Beam-Beam Interaction Study in ERL Based eRHIC

Yue Hao

Submitted to the faculty of the University Graduate School
in partial fulfillment of the requirements
for the degree
Doctor of Philosophy
in the Department of Physics,
Indiana University
September, 2008

Accepted by the Graduate Faculty, Indiana University, in partial fulfillment of the requirements for the degree of Doctor of Philosophy.

Doctoral Committee

_____

(Shyh-Yuan Lee, PhD)

_____

(David V. Baxter, PhD)

_____

(Mark H. Hess, PhD)

_____

(Brian D. Serot, PhD)

Date of Oral Examination: August 22, 2008

Copyright ©2008 by
Yue Hao
ALL RIGHTS RESERVED

To My Parents and Wife

Acknowledgement

With my deep expression of gratitude, I wish to express my sincere appreciation to my thesis advisor, Dr. Shyh-Yuan Lee, for his immense help and supports in selecting the subject and implementing this works in time. With his profound knowledge and assiduous attitude in research, Dr. Lee led me beyond the entrance of accelerator physics, on the track of a scientific researcher. Also, I wish to acknowledge the committee members, Dr. Mark Hess, Dr. David Baxter and Dr. Brian Serot, for their precious advice and correction for my thesis.

The research work in this thesis is accomplished in Brookhaven National Laboratory. I would like to express my gratitude to scientists in BNL who gave their kindness help in finish my thesis. My special appreciations are due to Dr. Vadim Ptitsyn for his guidance and thoughtful discussion throughout the past two years. I am also thankful to Dr. Vladimir Litvinenko, Dr. Eduard Pozdeyev, Dr. Christoph Montag, Dr. Ilan Ben-Zvi and many more for their kindly help.

I want to thank all my friends, both those who in the same field and those who have no idea about accelerator, for their friendship and encouragement.

The acknowledgement will never complete without addressing my family. I am grateful to my parents and wife for their inspiration and moral support all the time. Without their loving supports and understanding I would never have completed my present work.

ABSTRACT

Yue Hao

Beam-Beam Interaction Study in ERL Based eRHIC

There is growing interest in physics community in building high energy, high luminosity polarized electron-ion collider in order to study the fundamental structure of nucleons and nuclei and details of QCD theory governing the interaction in nuclear matter. eRHIC will take advantage of existing RHIC ion collider at BNL with addition of an electron accelerator to provide orders higher luminosity compared with RHIC.

There are several unique features of beam-beam effect, special for the linac-ring design. The features include: electron disruption effect by beam-beam interaction; proton beam instability of head-tail type ('kink instability'); pinch effect of electron beam and related proton beam dynamics and emittance growth; turn-by-turn noise of the electron beam and its impact on the proton beam.

Through analytical calculation and simulation, all special features above are studied carefully. The electron disruption effect and distribution distortion can be controlled by proper electron lattice and initial rms emittance. Large initial rms emittance (5nm-rad) and small waist beta function (0.2m) can reduce the mismatch between electron distribution after collision and design lattice and the electron distortion due to nonlinear force. This set of electron beam parameters also

decreases the emittance growth of proton beam.

Analytical approach and simulation also shows the kink instability induced by beam-beam force has threshold which is more than ten times smaller than design parameter. Proper tune spread is necessary to suppress fast proton emittance growth. Simulation shows a chromaticity value 7 to 8 is optimum for rms energy spread 5×10^{-4}. The tune spread can also be achieved by nonlinear lattices such as octopoles.

The effect on proton beam, due to turn by turn noise from fresh electron bunch is also estimated. Both dipole and quadrupole errors and their consequence are analyzed. The criteria are brought out for certain proton lifetime.

In one word, the ERL based eRHIC is a promising design for RHIC upgrade from beam-beam interaction study. It provides a versatile way that delivers 10^{33} $cm^{-2}s^{-1}$ luminosity for future nuclear physics research.

Table of Contents

List of Tables x

List of Figures xi

1. Introduction to eRHIC Project 1

1.1. From RHIC to eRHIC 1

1.2. The First Linac-Ring Collider 4

1.3. Energy Recovery Linac 8

2. Overview of Beam-Beam Effect 11

2.1. Charge Distribution and Field 11

2.2. Incoherent Beam-Beam Limit 16

2.3. Hourglass Effect 17

2.4. The Simulation Codes 20

3. Electron Disruption Effect 28

3.1. The Linear Mismatch 28

3.2. Nonlinear Disruption Effect 34

3.3. Luminosity Enhancement 42

3.4. Transverse Beer-Can Distribution Electron Beam 45

3.5. Electron Beam Optics Optimization 54

3.6. Beam Loss Estimation and Matching 60

4. Kink Instability 66

4.1. Cause and Threshold 66

4.2. Kink Instability from Simulation Results 73

4.3. Beam Stabilization and Slow Emittance Growth 80

5. Pinch Effect 87

5.1. Collision of Thin Proton Beam with Rigid Electron Beam 87

5.2. Electron Pinch Effect and Beam-Beam Field Calculation 93

5.3. Proton Emittance Growth under Pinch Effect 101

6. Noise 106

6.1. Noise of Electron Beam 106

6.2. Noise of Electron Beam Intensity and Displacement 107

7. Conclusion 114

Appendix A. Symplectic Integrator 117

List of Tables

Table 1.1: eRHIC parameter, Ring-Ring Scheme 5

Table 1.2: eRHIC parameter, Linac-Ring Scheme 7

Table 1.3: Comparison of different cooling method 8

Table 2.1: RF and related parameters 24

Table 3.1: Portion of particle be covered in certain emittance 41

Table 3.2: Luminosity of different initial electron beam parameters 44

Table 3.3: Test parameter table (design values is marked with #) 55

Table 5.1: Lifetime of Proton beam with different electron beam distribution 90

Table 5.2: Lifetime of Proton beam with different edge size in Beer-Can distribution

..... 93

Table 5.3: Lifetime of Proton beam with different initial electron beam parameter . 104

List of Figures

Figure 1.1: RHIC layout from sky 3

Figure 1.2: Layout of eRHIC Linac-Ring scheme.....6

Figure 1.3: Energy Recovery Linac layout in eRHIC and the electrons in main ERL with accelerating phase (red dots) and decelerating phase (blue dots).....9

Figure 2.1: Beam-Beam electric field amplitude of transverse symmetry Gaussian beam.....13

Figure 2.2: Beam rms size change, hourglass effect illustration 19

Figure 3.1: The numerical solution of equations in (3.8) is blue curve, while read curve corresponds to betatron amplitude function without beam-beam force. In (a) and (b), the initial beta function minimum is 1 meter; in (c) and (d) the initial beta function minimum is 0.2 meter. In all graphs, the initial beta waist position is at IP.....32

Figure 3.2: The numerical solution of equations in (3.8) is blue curve, while read curve corresponds to betatron amplitude function without beam-beam force. In (a) and (b), the initial beta function minimum is 0.225 meter,

with waist position at IP. 33

Figure 3.3: Evolution of Beam Size and Emittance of Electron Beam 35

Figure 3.4: Phase space distribution of electron beam after collision for β^*=1m, back traced to the IP. Mismatch between the geometric emittance and Courant-Snyder invariant ellipse of design lattice. 36

Figure 3.5: Comparison of rms geometric and effective emittance of electron beam in beam-beam interaction for β^*=1m 38

Figure 3.6: Evolution of beam size and rms emittance of electron beam for β^*=0.2m, both geometric and effective emittance. 39

Figure 3.7: Phase space distribution of electron beam after collision for β^*=0.2m, back traced to IP. Mismatch between the geometric emittance and Courant-Snyder invariant ellipse of the design lattice.....40

Figure 3.8: 100% electron geometric and effective emittance as function of cut off points for Gaussian distribution, for both large (initial rms emittance = 5nm-rad; β^*=0.2m) and small initial emittance (initial rms emittance = 1nm-rad; β^*=1m).....42

Figure 3.9: Electron and Proton rms beam size as function of longitudinal position..44

Figure 3.10: Transverse picture of Beer-Can distribution (left) and Gaussian distribution (right) for round beam with same rms beam size $\sigma=3.1\times10^{-5}$m. 48

Figure 3.11: Evolution of beam size and rms emittance of electron beam for β^*=1m

and initial Beer-Can transverse distribution, both geometric and effective emittance. 50

Figure 3.12: Evolution of beam size and rms emittance of electron beam for β^*=0.2m and initial Beer-Can transverse distribution, both geometric and effective emittance. 51

Figure 3.13: Phase space map after collision of initial Beer-Can distribution Electron beam, the figure corresponds to initial transverse rms emittance 1×10^{-9} m-rad and β^*=1m; the bottom one corresponds to initial rms emittance 5×10^{-9} m-rad and β^*=0.2m. 52

Figure 3.14: 100% electron geometric and effective emittance as function of cut off points for Beer-Can distribution, for both large (initial rms emittance = 5nm-rad; β^*=0.2m) and small initial emittance (initial rms emittance = 1nm-rad; β^*=1m) 53

Figure 3.15: Electron rms geometric emittance after collision as function of luminosity 55

Figure 3.16: Electron rms effective emittance after collision as function of luminosity, the legend shows different initial electron emittance with unit $\times10^{-9}$ m-rad 56

Figure 3.17: Electron 100% effective emittance after collision as function of luminosity, the legend shows different initial electron emittance with unit $\times10^{-9}$ m-rad 57

Figure 3.18: Luminosity and electron beam size dependence as function of waist position. 59

Figure 3.19: Power loss at given aperture and energy with initial Gaussian distribution and Beer-Can distribution, high energy setup. 62

Figure 3.20: Power loss at given aperture and energy with initial Gaussian distribution and Beer-Can distribution, low energy setup. 63

Figure 3.21: Comparison power loss at 0.5GeV, between different initial energy, 10GeV and 3GeV electron beam 63

Figure 3.22: Power loss at 0.5GeV with or without matching scheme, top is initial 10GeV case and bottom is 3GeV case. 65

Figure 4.1: Wake field that the proton beam exerts, with different initial offset position of proton beam. 69

Figure 4.2: The proton rms emittance growth with different proton beam intensity. .. 74

Figure 4.3: The proton rms emittance growth with different electron beam intensity. 75

Figure 4.4: The proton rms emittance growth with different proton rms bunch length. 76

Figure 4.5: The proton rms emittance growth with different proton beam intensity with linearized beam-beam force and without hourglass effect. 77

Figure 4.6: FFT of proton beam horizontal centroid with different proton intensities. 78

Figure 4.7: Proton beam centroid FFT peak as function of proton intensity. The tune

peaks have been normalize by $(\nu-\nu_\beta)/\nu_s$. 79

Figure 4.8: Snapshot of proton centroid position.....80

Figure 4.9: Proton rms emittance growth under different chromaticity.....81

Figure 4.10: Proton emittance growth with different chromaticity 82

Figure 4.11: Proton rms emittance growth under different chromaticity with low proton intensity (1×10^{11} per bunch).....83

Figure 4.12 : Slow proton emittance growth at when chromaticity equals 7. 84

Figure 4.13: Proton rms emittance growth slope as function of macro-particle number 85

Figure 5.1: The beam-beam field of Gaussian and Beer-Can distribution with same beam intensity. 89

Figure 5.2: Comparison of proton rms emittance with rigid Gaussian and Beer-Can electron transverse distribution.....90

Figure 5.3: Soft edge Beer-Can distribution with different edge.....91

Figure 5.4: Beam-Beam Field calculated from Beer-Can transverse distribution with different edge size. The right graph is the zoom-in graph of left one at edge. 92

Figure 5.5: Proton emittance evolution under different size of edge in 'soft' Beer-Can distribution model. 92

Figure 5.6: Electron pinch effect with different initial electron parameter 94

Figure 5.7: Average electron rms beam size as function of luminosity. 96

Figure 5.8: Electron position histogram after Beam-Beam collision. Initial electron rms emittance is 1nm-rad and β^* is 1m at IP. Green curve corresponds to the Gaussian function fit based on electron beam rms size and histogram data. 98

Figure 5.9: Electron position histogram after Beam-Beam collision. Initial electron rms emittance is 5nm-rad and β^* is 0.2m at IP. Green curve corresponds to the Gaussian function fit based on electron beam rms size and histogram data. 99

Figure 5.10: Beam-Beam field calculated by Gauss Law and from rms beam size .. 100

Figure 5.11: Proton rms emittance comparison between different electron beam initial emittance. 102

Figure 5.12: Proton rms emittance growth at small waist beta functions at different waist positions. 103

Figure 6.1: Transverse rms size rising time as function of electron intensity relative rms error 110

Figure 6.2: Proton rms beam size evolution under the presence of electron intensity noise and comparison with prediction of equation (6.9), each beam size data is the average of 1000 turns nearby. 111

Figure 6.3: Details of proton beam rms beam size and angular divergence without averaging under the presence of electron intensity noise 112

1. INTRODUCTION TO ERHIC PROJECT

1.1. From RHIC to eRHIC

Relativistic Heavy Ion Collider (RHIC)[1] is a heavy ion collider at Brookhaven National Laboratory (BNL) operated since 2000, followed by 16 years of development and construction. It accelerates heavy ion (such as gold) to top energy of 100 GeV/u or polarized proton to 250 GeV and brings out head-on collision.

The objectives of RHIC are to study the state of matter formed in the first microseconds of early universe and to study spin origin and structure of proton. With very high energy in center of mass (200 GeV/u for gold nuclei, 500GeV for proton), we can create very high matter density and temperature condition and expect nuclear matter to undergo a phase transition and form the plasma of quarks and gluons. This transition and property of quark gluon plasma can be predicted by the theory called Quantum Chromo Dynamics (QCD) which describes the strong interaction.

Initially, the proton and ion beams are generated from Tandem Van de Graaff and then accelerated by Linac accelerator to 200MeV. Then the particles will be transported to AGS booster and then AGS (Alternating Gradient Synchrotron) ring and be accelerated to 99.7% of speed of light before exiting (velocity depends on type of nuclei). The AGS serves as injector of RHIC ring.

For main part of RHIC, two concentric superconducting magnet rings (noted as yellow and blue respectively) were built in a ring tunnel. Beams are counter-rotating in two rings, accelerated from injection energy and then stored at top energy. There are six intersection points along the circumference located at twelve (IP 12, similar for other collision points), two, four, six, eight and ten o'clock position, where two counter-rotating beams collide with each other. Currently, the two experiments, named by STAR and PHENIX, locate at IP6 and IP8 respectively. The design luminosity at top energy is 1×10^{31} $cm^{-2}s^{-1}$ for proton-proton collision and 2×10^{26} $cm^{-2}s^{-1}$ for gold-gold collision. Here luminosity is the most important parameter of collider performance and represent the collision rate per unit area per unit time, usually expressed in $cm^{-2}s^{-1}$. Explicitly, it is defined as below if both beams are Gaussian distribution in both transverse directions.

$$L = \frac{N_1 N_2 f h}{2\pi\sqrt{\sigma_{x1}^2 + \sigma_{x2}^2}\sqrt{\sigma_{y1}^2 + \sigma_{y2}^2}} \tag{1.1}$$

Here, subscription 1 and 2 denote 2 beams respectively. N is the bunch intensities. f is the revolution frequency; h is bunch number in the ring. Horizontal and vertical rms beam sizes at collision point are σ_x and σ_y. Also, we assume that both beams bunch lengths are short (infinitesimal bunch length).

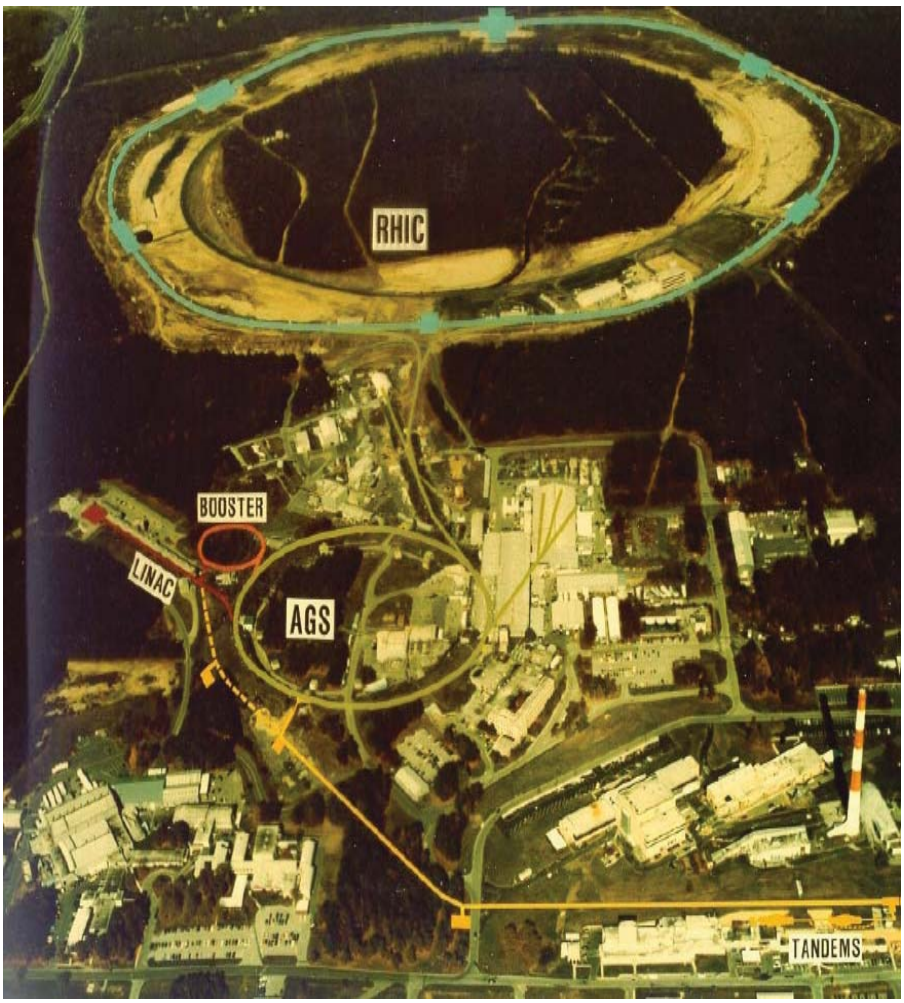

Figure 1.1: RHIC layout from sky

As an important upgrade of RHIC, eRHIC[2, 3] is brought out as an advance experiment tool to answer more questions of fundamental structure of matters, such as the structure (both momentum distribution and spin properties) of hadrons, the role of quarks and gluons with dynamics of confinement, etc. Also, eRHIC can provide more precise instrument to explore and test the theory of QCD itself in the extent of many-body and other aspects.

In order to make eRHIC be an attractive tool, the following aspects must be achieved:

- Collision between electron beam with various nuclei (from proton to

heavy nuclei)

- The energy of electron beam and nuclei is adjustable over a large range
- Higher Luminosity (order of 10^{33} $cm^{-2}s^{-1}$)
- High polarization for both electron beam and proton beam

To fulfill the requirements above and control the cost, eRHIC will take advantage of existing RHIC ion collider with addition of an electron accelerator, which will generate high intensity high quality electron beam. An upgrade will be made in the RHIC ring including transverse and longitudinal cooling to reach the required beam quality. The designed parameter for eRHIC will reach,

- 5-10 GeV electron beam energy
- 50-250 GeV proton beam energy, 100GeV/u Au ions
- 70% polarization for both electron beam and proton beam

In the eRHIC design, there is capability of operating both ion-ion and electron-ion collision at same time, which is called 'parallel mode', instead of electron-ion collision only, referred as 'dedicated mode'. In this thesis, we only discuss dedicated mode, in which ion beam only with electron beam once per turn.

1.2. The First Linac-Ring Collider

Presently, there are two possible designs for the proposed electron accelerator. One design is called ring-ring design. In this scheme, the electron beam is generated

from a polarize electron source and accelerated in recirculating linac injector to energy of 5 – 10 GeV. After the electron beam reaches top energy, it will be injected to newly-built electron storage ring. The storage ring intersects with RHIC blue ring at one existing interaction point (currently at IP12). And new detector, special designed for electron–ion collision, will be built at that interaction point.

Currently the parameters for ring-ring option are listed in Table 1.1. We can find that the luminosity in this scheme is about half of the design order 10^{33} $cm^{-2}\cdot s^{-1}$.

Table 1.1: eRHIC parameter, Ring-Ring Scheme

	High energy setup		Low energy setup	
	p	e	p	e
Energy (GeV)	250	10	50	5
Number of bunches	165	55	165	55
Bunch spacing (ns)	71	71	71	71
Bunch intensity ($\times 10^{11}$)	1.0	2.34	1.49	0.77
Beam current (mA)	208	483	315	353
95% normalized emittance (π·mm·mrad)	15		5	
Rms emittance (nm),x/y	9.5/9.5	53.0/9.5	15.6/15.6	130/32.5
β^* (cm), x/y	108/27	19/27	1.86/0.46	0.22/0.22
Beam-beam parameters, x/y	0.015/0.0075	0.029/0.08	0.015/0.0075	0.035/0.07
Rms bunch length (cm)	20	1.2	20	1.6
Polarization, %	70	80	70	80
Peak Luminosity, $cm^{-2}s^{-1}$	**0.47×10^{33}**		0.082×10^{33}	

Aside from ring-ring option, there is another scheme named 'Linac-Ring' scheme. The idea is easily derived for its name. The electron beam will be accelerated by a Linac accelerator and directly transport to interaction region. When

collision process at IP finishes, the electron beam will be dumped after its energy being recovered. This will be the world first Linac-Ring collider. Parameters of Linac-Ring scheme are listed in Table 1.2. There are many advantages in Linac-Ring scheme compared with Ring-Ring scheme. All attractive merits come from the idea that we have fresh electronic bunch in each collision. From the comparison of two tables, we can easily discover the most important one, **the luminosity enhancement from 0.47×10^{33} to 2.6×10^{33}** $cm^{-2}s^{-1}$. In Linac-Ring option, we can apply larger beam-beam force on electron bunches hence achieve higher luminosity. Beside the luminosity enhancement, other significant advantages include full spin transparency for all energies; longer drift space for detector in interaction region, easily upgradeable option for higher electron energy (20GeV) and wider electron energy range.

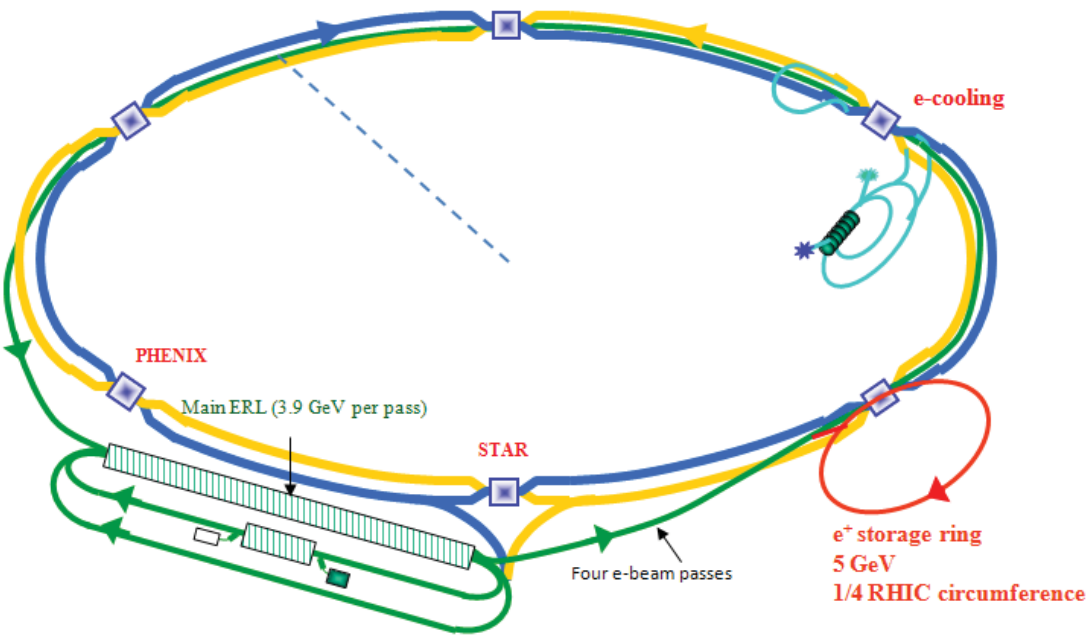

Figure 1.2: Layout of eRHIC Linac-Ring scheme

Table 1.2: eRHIC parameter, Linac-Ring Scheme

	High energy setup		Low energy setup	
	p	e	p	e
Energy (GeV)	250	10	50	3
Number of bunches	166		166	
Bunch spacing (ns)	71	71	71	71
Bunch intensity ($\times 10^{11}$)	2	1.2	2.0	1.2
Beam current (mA)	420	260	420	260
95% normalized emittance (π·mm·mrad)	6	115	6	115
Rms emittance (nm),	3.8	1.0	19	3.3
β^* (cm), x/y	26	100	26	150
Beam-beam parameters, x/y	0.015	2.3	0.015	2.3
Rms bunch length (cm)	20	0.7	20	1.5
Polarization, %	70	80	70	80
Peak Luminosity, $cm^{-2}s^{-1}$	**2.6×10^{33}**		0.53×10^{33}	

The Linac-Ring scheme is preferred with all advantages listed above. Since this is the first proposed linac-ring scheme collider, there will be many unique features distinguished from traditional ring-ring or linac-linac colliders. In this thesis, we will focus on new features of beam-beam effect and discuss the countermeasures of prospected side-effects of this layout. From Table 1.2, the transverse beam sizes for both beams are the same ($\sigma_{px}= \sigma_{py}$, $\sigma_{ex}= \sigma_{ey}$). In many formulas in the following chapters, we will take advantage and not distinguish rms beam sizes of two transverse directions. Without further notice, we will only discuss dynamics property in x direction (horizontal) from now on. The same result is expected from vertical direction due to symmetry.

To achieve high luminosity collision in eRHIC, proper cooling is necessary for preventing degradation of the proton beam quality. Currently, four cooling methods are brought out, including stochastic cooling[4], electron cooling[5], optical stochastic cooling (OSC)[6] and coherent electron cooling (CEC)[7]. Coherent electron cooling is the most efficient way according to theoretical estimation and simulation.

Table 1.3: Comparison of different cooling method

Particle species	Energy (GeV / u)	Approximate Cooling Time (Hour)		
		Stochastic Cooling	Electron Cooling	CEC
Proton in eRHIC	325	1	1	0.05
Gold in eRHIC	130	100	30	0.3

1.3. Energy Recovery Linac

The electron accelerator in eRHIC is designed to be an energy recovery linac (ERL) to provide both high energy efficiency and high electron beam current.

ERL[8] has a long history, tracing back to more than three decades. It combines the advantages of both linac and ring accelerators and has the potential to provide high current, short pulse and excellent beam quality at same time. An obvious application for ERL is to provide high peak current electron beam for synchrotron radiation light source or free electron laser.

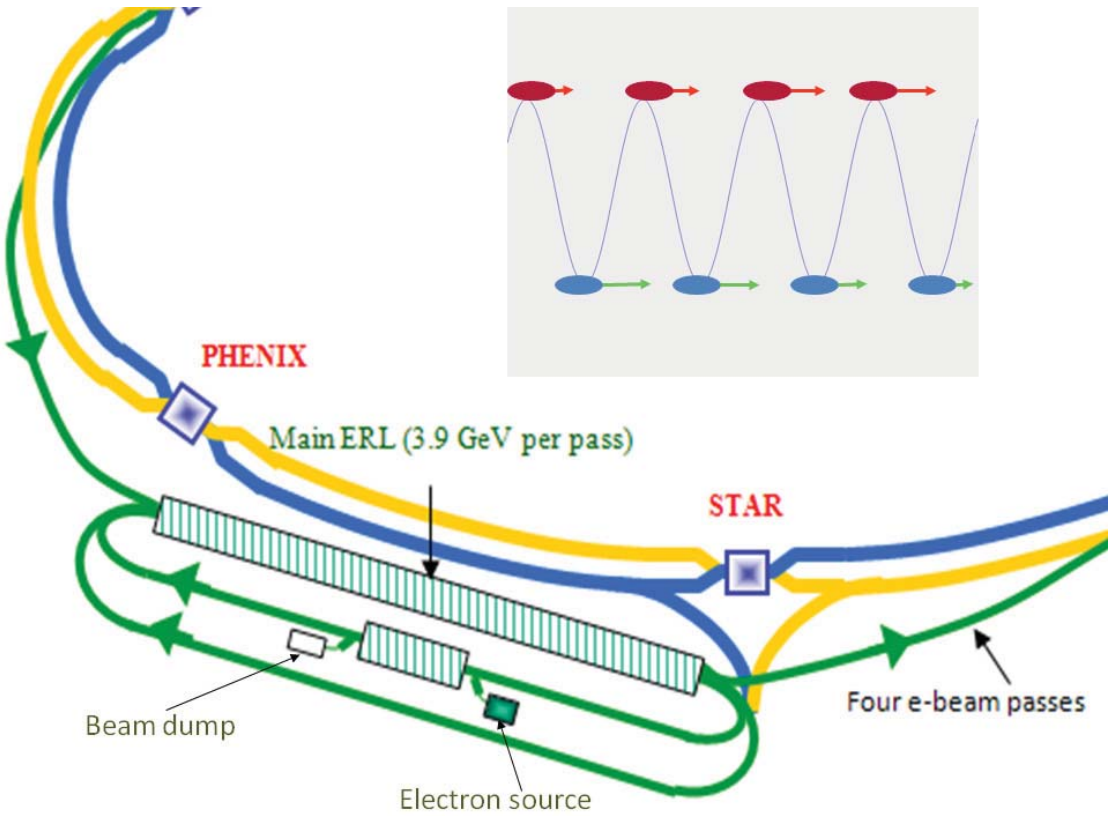

Figure 1.3: Energy Recovery Linac layout in eRHIC and the electrons in main ERL with accelerating phase (red dots) and decelerating phase (blue dots).

In the ERL base eRHIC scheme, the electron beam is accelerated from the source though a superconducting RF cavity (main ERL in Figure 1.3) and transported through electron beam pass along arrow direction. If the electron energy does not reach the desired energy, the electron will be transferred one turn back to main ERL with correct phase (acceleration phase) and accelerate again until desired energy is reached. Then the full energy electron beam will collide with the proton beam at interaction region. After collision, the electron beam will be transfer back to main ERL with decelerating phase, which has π difference with the accelerating phase. The high energy electron beam with decelerating phase will pass its energy to RF field in the main ERL. This portion of energy will be used to accelerate low energy electron beam with accelerating phase. After energy loss process in main ERL, the electron beam will be terminated at beam dump with very low energy.

Compared with conventional Linac accelerators, the power needed by ERL is reduced dramatically. Therefore, much higher average current can be achieved compared to a linac without energy recover scheme.

Compared with storage ring accelerators, the ERL does not recirculate the electron beam itself; it only retrieves the electron energy. The electron beam does not have sufficient time to reach its equilibrium state due to synchrotron radiation and quantum excitation. Therefore, the electron beam quality mainly depends on the source which is much better than the equilibrium state in storage rings. However, currently the average beam current in ERL cannot reach the typical current in storage ring (order of Ampere). In ERL the achievable average current is in order of 100 mA.

2. OVERVIEW OF BEAM-BEAM EFFECT

Beam-Beam effect is the most important factor that limits colliders achieving higher luminosities. This chapter reviews key points of beam-beam interaction generally and special features in designing ERL based eRHIC project.

2.1. Charge Distribution and Field

In collider, beam-beam effect refers to the interaction between two colliding beams via electro-magnetic field. The section where two beams intercept with each other is called interaction region, which is usually positioned in a drift space. In modern colliders, beam-beam effect becomes one of the most important factors that limit the luminosity.

During collision, one moving bunch generates both electric field and magnetic field. The fields will exert on itself and the opposite beam simultaneously. The force on itself is called space charge force. At very high energy when the speed of the bunch approaches speed of light, the space charge force vanishes. The force applied on the opposite beam is called beam-beam force, which will be enhanced in the high energy case.

Before further discussion, we make assumptions that both beams are relativistic

where $\gamma \gg 1$ and $\beta < 1$, the electromagnetic field is only in transverse two-dimension space. Also we only discuss the head on collision which excludes collisions with crossing angle. The assumptions we made are very suitable for eRHIC without losing physics details.

The most general charge distribution model is Gaussian distribution in two transverse dimensions, written as:

$$\rho(x,y) = \frac{n(z)e}{2\pi\sigma_x\sigma_y}\exp(-\frac{x^2}{2\sigma_x^2}-\frac{y^2}{2\sigma_y^2}) \tag{2.1}$$

Where $n(z)$ is the line charge density, and transverse rms beam sizes are represented as σ_x and σ_y. From charge distribution (2.1), one can derive the electric field from its scalar potential U, and the electric field has the form:

$$E_x - iE_y = -\frac{ine}{2\varepsilon_0\sqrt{2\pi\left(\sigma_x^2-\sigma_y^2\right)}}\left[w\left(\frac{x+iy}{\sqrt{2\left(\sigma_x^2-\sigma_y^2\right)}}\right)-\exp\left(-\frac{x^2}{2\sigma_x^2}-\frac{y^2}{2\sigma_y^2}\right)w\left(\frac{\frac{x\sigma_y}{\sigma_x}+i\frac{y\sigma_x}{\sigma_y}}{\sqrt{2\left(\sigma_x^2-\sigma_y^2\right)}}\right)\right] \tag{2.2}$$

This was derived by Bassetti and Erskine. In (2.2), $w(z)$ is the complex error function defined as:

$$w(z) = \exp\left(-z^2\right)\mathrm{erfc}(-iz) = \exp\left(-z^2\right)\left(1-\mathrm{erf}(-iz)\right)$$

For eRHIC case, the vertical and horizontal rms beam sizes are identical. The expression (2.2) can be simplified as:

$$\vec{E}_r = \frac{n(z)e}{2\pi\varepsilon_0 r^2}\left[1-\exp\left(-\frac{r^2}{2\sigma^2}\right)\right]\vec{r} \tag{2.3}$$

It is notable that $\sigma_x = \sigma_y$ is not a singular point in (2.2). We can plot the field amplitude as Figure 2.1. The field maximum reaches at 1.85σ. Below 1 rms size, the field is almost linear.

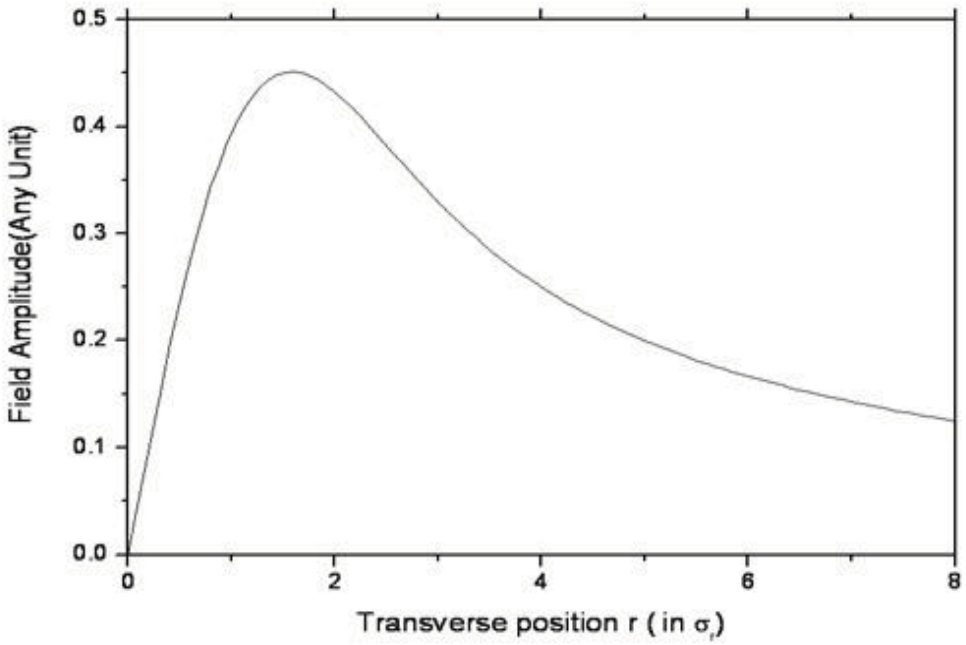

Figure 2.1: Beam-Beam electric field amplitude of transverse symmetry Gaussian beam

Then the magnetic field can be calculated as:

$$\vec{B} = \vec{\beta} \times \vec{E} / c \tag{2.4}$$

Above, βc is the velocity of moving bunch. This is obvious if we investigate the bunch from the moving bunch rest frame, where the magnetic field vanishes. Then Lorentz force exerted on particle of the bunch itself F_{11} (space charge force) and on particle of the opposite bunch F_{12} (beam-beam force) can be expressed respectively:

$$F_{11} = e\left(\vec{E} + \left(-\vec{v}\right)\times\vec{B}\right) = e(1-\beta^2)\vec{E} = e\vec{E}/\gamma^2$$
$$F_{12} = e\left(\vec{E} + \left(\vec{v}\right)\times\vec{B}\right) = e(1+\beta^2)\vec{E} \approx 2e\vec{E} \tag{2.5}$$

As what we stated before, the space charge force vanishes as the particle velocity approaches c, while beam-beam force is enhanced.

Consider near axis case of equation (2.2), the field is linear in both transverse directions. The electric field reduces to:

$$\begin{pmatrix} E_x \\ E_y \end{pmatrix} = \frac{n(z)e}{2\pi\varepsilon_0\left(\sigma_x + \sigma_y\right)}\begin{pmatrix} x/\sigma_x \\ y/\sigma_y \end{pmatrix} \tag{2.6}$$

We can see that beam-beam force is linear near axis, which is similar to the case of a thick quadrupole. But this 'beam-beam quadrupole' focuses or defocuses in both transverse directions. If the bunch is very short, equivalently $n(z) = N\delta(z)$, the beam-beam effect can be modeled as a thin quadrupole near axis. Focal lengths of the beam-beam effect are given as:

$$\frac{1}{f_x} = -\frac{2C_1C_2Nr_0}{\left(\sigma_x + \sigma_y\right)\sigma_x\gamma}$$
$$\frac{1}{f_y} = -\frac{2C_1C_2Nr_0}{\left(\sigma_x + \sigma_y\right)\sigma_y\gamma} \tag{2.7}$$

Here, N is the total particle number in the bunch, $r_0 = e^2/(4\pi\varepsilon_0 mc^2)$ is the classical radius of particle in opposite bunch who exerts the field, C_1C_2 is the charge number of particle from two colliding bunch. We already assume that both bunches are highly relativistic, i.e. $\beta = 1$, which will hold throughout the thesis. Without further notice, β will represent the beta function below. For RHIC proton-proton collision, the beam-beam force is defocusing, $C_1C_2 = 1$; for eRHIC electron-proton collision, $C_1C_2 = -1$.

Now we can introduce the beam-beam parameter, one most important parameters in beam-beam dynamics. The beam-beam parameter ξ is defined as:

$$\xi_{x,y} = \frac{\beta^*_{x,y}}{4\pi}\frac{1}{f_{x,y}} \tag{2.8}$$

Here, β^* is the waist beta function at $z = 0$. For eRHIC the beam-beam parameter for proton and electron are:

$$\xi_p = \frac{N_e r_{0p}\beta^*_p}{4\pi\sigma_e^2\gamma_p}; \qquad \xi_e = \frac{N_p r_{0e}\beta^*_e}{4\pi\sigma_p^2\gamma_e} \tag{2.9}$$

It is obvious that the physical meaning of beam-beam parameter is the tune shift created by linear beam-beam force approximation.

From equation (1.1) and (2.9), we can summarize some useful rules to maximize the luminosity without increasing the beam-beam parameter.

I. Set dispersion to be zero at interaction region.

II. Set the interaction point at waist of beta function, i.e. $\alpha = 0$ at IP

III. Decrease the minimum beta (at waist) as small as possible.

In actual designs, there are restrictions from choosing a too small beta function at interaction region. A tiny beta function at IP may lead to unacceptable beta function outside interaction region and large radiation because of beam bending.

2.2. Incoherent Beam-Beam Limit

From the beam-beam parameter ξ defined in last section, we treat the beam-beam force as a thin length quadrupole. Without beam-beam effect, a test particle has its trajectory around the ring, which can be expressed as a one turn map $M(s_0)$. By choosing s_0 to be the longitudinal position at interaction point, we can have the turn-by-turn coordinate of the testing particle at interaction point without beam-beam effect. Then we can multiply a thin length quadrupole matrix K to the one turn map M:

$$K \cdot M = \begin{pmatrix} 1 & 0 \\ -1/f & 0 \end{pmatrix} \cdot \begin{pmatrix} \cos(2\pi\nu) & \beta^* \sin(2\pi\nu) \\ -\sin(2\pi\nu)/\beta^* & \cos(2\pi\nu) \end{pmatrix} \tag{2.10}$$

Here, f is the beam-beam focal length defined in (2.7), β^* is the beta waist function at interaction point, ν is transverse tune. The resulting one turn matrix including beam-beam effect gives,

$$M_t = \begin{pmatrix} \cos(2\pi\nu) & \beta^* \sin(2\pi\nu) \\ -\dfrac{\sin(2\pi\nu)}{\beta^*} - \dfrac{\cos(2\pi\nu)}{f} & \cos(2\pi\nu) - \dfrac{\beta^* \sin(2\pi\nu)}{f} \end{pmatrix} \tag{2.11}$$

There is a tune change due to beam-beam kick. We have:

$$\begin{aligned} 2\cos(2\pi\nu + 2\pi\Delta\nu) &= Tr(M_t) \\ &= 2\cos(2\pi\nu) - \frac{\beta^* \sin(2\pi\nu)}{f} \end{aligned} \tag{2.12}$$

If the beam-beam focus effect is very small, i.e. $f \gg \beta^*$, we proved that the tune change $\Delta\nu = \beta^*/4\pi f$, which is just the definition of beam-beam parameter ξ in (2.9).

The new one turn matrix M_t represents a stable motion only if the condition $|Tr(M_t)| \leq 2$ is valid. This gives:

$$-2 \leq 2\cos(2\pi\nu) - \frac{\beta^* \sin(2\pi\nu)}{f} \leq 2$$

And the linear stability criterion is given as:

$$\xi = \frac{1}{4\pi}\frac{\beta^*}{f} < \begin{cases} \cot(\pi\nu)/2\pi & n < \nu < n+0.5 \quad n \in Z \\ -\tan(\pi\nu)/2\pi & n+0.5 < \nu < n+1 \quad n \in Z \end{cases} \tag{2.13}$$

Based on modern collider design, the beam-beam limits are about the order of 0.01 to 0.1, far below the criterion in (2.13). For example, in eRHIC design table, the fraction tune for proton ring is 0.685. According to (2.13), the upper limit gives 0.24, which is much larger than the design beam-beam parameter for proton. As we will reveal later, this limit is the weakest constraint. It is worthwhile to point out again that the beam-beam parameter for electron is not limited by the criterion discussed above. This is the main benefit we can get from the linac-ring scheme.

2.3. Hourglass Effect

The hourglass effect comes from the beam size difference among various longitudinal positions. The previous sections in this chapter are focused in transverse beam dynamics with the assumption that both beams are infinitely short and collide exactly at interaction point. In real cases, each colliding beam has a finite beam length. Particles with different longitudinal positions collide with the

opposing beam with different field and different tune shift.

In interaction region, without beam-beam effect, the beam emittance remains unchanged and the beam size at *s* away from the IP gives:

$$\sigma_x = \sqrt{\varepsilon_x \beta_x(s)} = \sqrt{\varepsilon_x \left[\beta_x(0) + s^2 / \beta_x(0)\right]} \tag{2.14}$$

Figure 2.2 illustrates the hourglass effect for the eRHIC linac-ring scheme. The electron beam (Green) is much shorter than proton beam (red). Because the proton ring's beta waist at IP is only about 0.26m, comparable with proton rms bunch length 0.2m, different longitudinal proton slices transverse rms size varies about 50% during collision with electron beam.

Obviously the hourglass effect results in changing of beam-beam parameters. For proton beam, particle at longitudinal position *s* has beam-beam parameter as:

$$\xi_p = \frac{N_e r_{0p} \beta_p^*(s)}{4\pi\sigma_e^2(s)\gamma_p} \tag{2.15}$$

The proton beam-beam parameter will have longitudinal position dependence. Combined with synchrotron oscillation, there will another reason for tune spread in additional to beam-beam force nonlinearity.

The electron bunch is very short, so we can assume it has delta function longitudinal distribution. The beam-beam parameter for electron has to be expressed by an integral:

$$\xi_e = \int \frac{N_p \lambda(s) r_{0e} \beta_e^*(s)}{4\pi\sigma_p^2(s)\gamma_e} ds \tag{2.16}$$

Here, $\lambda(s)$ is the normalized proton density distribution that electron meets at position s, which satisfies $\int\lambda(s)ds = 1$. And the luminosity formula will change to:

$$L = \int \frac{N_p N_e \lambda(s) fh}{2\pi\left[\sigma_{xp}^2(s) + \sigma_{xe}^2(s)\right]} ds \tag{2.17}$$

It has been simplified by the fact that both beams are round.

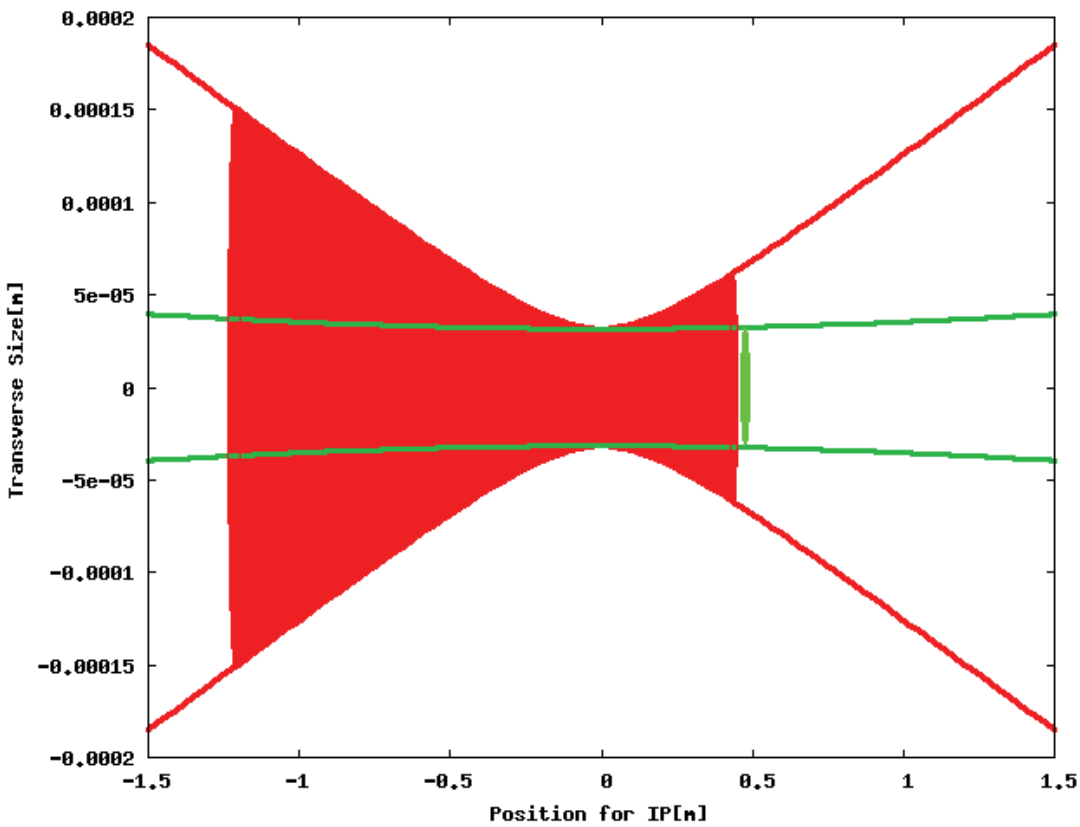

Figure 2.2: Beam rms size change, hourglass effect illustration

It is easy to observe, due to hourglass effect, only the center part of beam collide with center of opposite beam at the designed transverse rms beam size at IP. Both the head part and tail part will collide with larger rms beam size of itself and of opposite beam. Then the luminosity defined in (1.1) will be degraded by hourglass effect because the equation (1.1) assumes the collision only occurs at IP with designed transverse rms beam size. Typically the hourglass effect can be eliminated by

choosing same waist beta function β^*.

In eRHIC linac-ring scheme, hourglass effect cannot be cured and does not show significant effects because the electron beam is highly disrupted by proton beam. The deterioration will overwhelm hourglass effect. But the equation (2.15)--(2.17) will hold for any effects that induce transverse size change and any proton longitudinal distributions.

2.4. The Simulation Codes

Since the beam-beam effect is nonlinear force, it is very difficult to analyze the beam-beam effect in theory thoroughly. In order to study nonlinear dynamics and beam-beam effects of long time scale, we need numerical calculation methods.

Now, two kinds of simulation exist to simulate the beam-beam effects. One is called weak-strong model. In this model, one beam is assumed as rigid beam and is not affected by beam-beam effect. The beam-beam field of the rigid beam is calculated using equation (2.2), when transverse Gaussian distribution is expected, or directly calculated by solving Poisson equation with proper bounder condition for other specific transverse distribution. Then the opposite beam undergoes the beam-beam field of rigid beam. This weak-strong model is very suitable for retrieving the key nonlinear dynamics and easy to implement coding. Usually the calculation time is short. The drawback is also obvious.

Strong-strong models have been possible to implement as the computation power improves [9, 10]. In this model, both colliding beams exert field generated by opposite beams. Because the field calculation must be updated every collision, generally it is more time consuming compared with weak-strong codes. As we

mentioned above, the field can be calculated from the real-time beam distribution. By setting grids in both transverse directions, one can put all particles in grids according to their positions and derive the field from convolution of density (the number of particles in each grid) and green function of certain Poisson equation with certain boundary condition. This is usually referred as PIC (Particle In Cell) method. The PIC method gives self-consistent numerical solution for the beam-beam effect. But it is hard to implement coding and usually very time-consuming. Most strong-strong codes using PIC employ parallel computing libraries and run on clusters. Much calculation time can be saved by always assuming the beam distribution as Gaussian distribution and determine the field using (2.2). The median, amplitude and width of Gaussian distribution are variable and are calculated from real-time distribution. Because the Gaussian distribution parameters are not rigid, we call it 'Strong-Strong model with Soft Gaussian distribution'. In most cases it is adequately accurate and much faster than PIC method because we substitute the field solver with statistic characteristics of macro-particles.

In order to investigate the special feature of eRHIC, I programmed a code for linac-ring asymmetry scheme particularly. It simulates the ion beam in the ring undergoes turn-by-turn dynamics and collides with fresh electron beam from ERL at interaction point once per turn, as well as the status of electron beam after each collision. In the code, the beam-beam field is mostly calculated by the soft Gaussian distribution method.

The algorithm used in the code is straightforward. First we generate macro-particles for proton beam of total number N_p at interaction point. Each macro-particle has 6D coordinates (x, p_x, y, p_y, z, δ), representing coordinate and momentum of transverse direction x and y, longitudinal position relative to the reference particle and momentum deviation $\Delta p/p_0$ respectively. The whole N_p macro-particles have the designed rms values in all 6 coordinates with independent

Gaussian distribution. Then, similar to proton beam, we generate macro-particles 6D coordinates for electron beam of total number N_e with proper distribution and rms values.

After preparing all macro-particles, we cut the proton beam into longitudinal slices. The total slice number is indicated as n_s. Considering that proton beam is much longer than electron beam, we take electron beam as one slice, ignore its longitudinal size and choose n_s to be around 25 so that slices from both beams have similar slice sizes. Then we will calculate the beam-beam effect between electron slice and proton slices. Each proton will collide once with electron beam at half of its longitudinal position z apart from IP. We need to 'unfold' the proton beam as:

$$\begin{aligned} x(z/2) &= x(0) + p_x(0)z/2 \\ y(z/2) &= y(0) + p_y(0)z/2 \end{aligned} \tag{2.18}$$

Because the transverse momentum p_x and p_y remain constant in interaction region if beam-beam force is absent. The electron beam needs to be transported back to the position of first proton slice (head slice), and interact with proton beam slices in sequence while propagating forward. The beam-beam interaction is expressed as:

$$\begin{aligned} \tilde{p}_x &= p_x + \Delta p_x(x,y) \\ \tilde{p}_y &= p_y + \Delta p_y(x,y) \end{aligned} \tag{2.19}$$

The momentum with tilde represents the new momentum after beam-beam collision. The momentum change Δp is calculated from the field of opposite slice at transverse position (x,y). The proton macro-particles which undergo beam-beam kick are 'folded' to IP:

$$\begin{aligned} \tilde{x}(0) &= x(z/2) - \tilde{p}_x(z/2)z/2 \\ \tilde{y}(0) &= y(z/2) - \tilde{p}_y(z/2)z/2 \end{aligned} \tag{2.20}$$

Note that the positions with tilde are updated using new momentum; we can easily find the Jocobians of both transverse directions are 1. So the maps described above are symplectic.

$$\begin{vmatrix} \frac{\partial \tilde{x}}{\partial x} & \frac{\partial \tilde{x}}{\partial p_x} \\ \frac{\partial \tilde{p}_x}{\partial x} & \frac{\partial \tilde{p}_x}{\partial p_x} \end{vmatrix} = \begin{vmatrix} \frac{\partial \tilde{y}}{\partial y} & \frac{\partial \tilde{y}}{\partial p_y} \\ \frac{\partial \tilde{p}_y}{\partial y} & \frac{\partial \tilde{p}_y}{\partial p_y} \end{vmatrix} = 1 \tag{2.21}$$

This symplectic map refers to symplectic integrator of first order. In the code, 4th order symplectic integrator is another option, which runs slower but more accuracy compared with 1st order integrator for same time step.

Then we simplify all other linear lattices in proton ring as one-turn matrix at IP, written as:

$$\begin{pmatrix} \cos\left(2\pi\nu_{x/y}\right) + \alpha_{x/y}\sin\left(2\pi\nu_{x/y}\right) & \beta_{x/y}\sin\left(2\pi\nu_{x/y}\right) \\ -\left(1+\alpha_{x/y}^2\right)\sin\left(2\pi\nu_{x/y}\right)/\beta_{x/y} & \cos\left(2\pi\nu_{x/y}\right) - \alpha_{x/y}\sin\left(2\pi\nu_{x/y}\right) \end{pmatrix} \tag{2.22}$$

We did not use gamma function ($\gamma = (1+\alpha^2)/\beta$) above because of preventing confusion with the Lorentz factor gamma ($\gamma = E/m$). Since in eRHIC both beams are round beams, we will not distinguish transverse beta function and alpha function from now. To maximize the luminosity, one always set alpha function be zero at IP to get minimum beta function, hence minimum beam size. Then map (2.22) reduces to second matrix in (2.10) on the right hand side. At IP, the dispersion function is always set to zero, so the position is not directly related with momentum deviation δ.

Longitudinal map is similar to transverse maps when the synchrotron oscillation amplitude is small. In this case the oscillation is simply harmonic oscillation and the corresponding matrix reads:

$$\begin{pmatrix} z \\ \delta \end{pmatrix}_{n+1} = \begin{pmatrix} \cos(2\pi\nu_s) & -\mathrm{sgn}(\eta)k\sin(2\pi\nu_s) \\ \mathrm{sgn}(\eta)k\sin(2\pi\nu_s) & \cos(2\pi\nu_s) \end{pmatrix} \begin{pmatrix} z \\ \delta \end{pmatrix}_n$$
$$\eta = \frac{1}{\gamma_T^2} - \frac{1}{\gamma^2} \tag{2.23}$$

Where $k=\sigma_z/\sigma_\delta$, η is called phase-slip factor. In high energy storage ring as eRHIC proton ring, the phase-slip factor usually is positive, which is $(1/\gamma_T)^2$. Sometimes, the nonlinearity of synchrotron oscillation has important effect, then we can use the following map instead:

$$\delta_{n+1} = \delta_n - \frac{eV}{E}\left(\sin\left(\frac{2\pi hz}{C}\right) + \sin\phi_s\right)$$
$$z_{n+1} = z_n - C\eta(\delta_{n+1})\delta_{n+1} \tag{2.24}$$

Where E is the energy of beam, h is harmonic number, C is circumference of the ring, V is the RF voltage, and φ_s is the phase for synchronous particle. The current parameters in RHIC and proposed RF parameters are listed in Table 2.1.

Table 2.1: RF and related parameters

RF Voltage	6 (MeV)
Harmonic number	2520
Circumference of RHIC ring	3833 (m)
Transition energy γ_T of 08' run	23.57

By applying the maps to proton beam after beam-beam kink, we achieve the new coordinates of macro-particles for next beam-beam interaction with fresh electron beam with same initial distribution for each collision. The old electron beam information will be dump for data analysis.

After general description, we need to address the details of calculation the beam-beam effect each turn. In order to investigate the effects related to different

longitudinal position in proton bunch, such as head-tail effect (discussed in chapter 4) and pinch effect (discussed in chapter 5) during beam-beam effect, we divide the proton beam into longitudinal slices. If we simply allow the proton slices collide with electron beam individually, there will be artificial effects when synchrotron oscillation is included. Due to synchrotron oscillation, one single particle may travel from one slice to another after one after one turn map. Then, it will exert step function of beam-beam force between consequent turns when its longitudinal position is at the edge of one slice. This fake effect may cause artificial emittance growth on proton beam.

To eliminate this artificial effect with moderate calculation time, a 'two pass' procedure is performed. In the first pass, the proton beam is assumed as a rigid beam; while electron beam property is calculate at center of each proton slices. In second pass, the electron beam properties are interpolated at exactly the longitudinal position of each proton macro-particles. Then beam-beam field is calculated for each proton macro-particles to get smooth interaction along longitudinal direction.

Two interpolation methods are used in simulation. First is the linear interpolation, which means that straight lines are used to connect n_s discrete points. The interpolation is written as:

$$y(x) = y_1 + \frac{y_2 - y_1}{x_2 - x_1}(x - x_1) \tag{2.25}$$

Where $x_1 < x < x_2$ is assumed. The expression is simple and less CPU intensive. The possible drawback is the first order derivative of linear interpolation is not continuous, while the interpolation is continuous itself.

The higher order derivative's continuity can be assured by 3rd (cubic) order spline interpolation. The interpolation function $f_i(x)$ where x is between two adjacent

discrete points, x_i and x_{i+1}, gives:

$$f_i(x) = a_{i3}x^3 + a_{i2}x^2 + a_{i1}x + a_{i0} \tag{2.26}$$

Here subscript i is from 1 to n_s-1. The total spline 4(n_s-1) parameters above can be solved by following conditions:

$$\begin{aligned} &f_i(x_i) = y_i && f_i(x_{i+1}) = y_{i+1} \\ &f_i'(x_i) = f_{i-1}'(x_i) && f_i'(x_{i+1}) = f_{i+1}'(x_{i+1}) \end{aligned} \tag{2.27}$$

At boundary i=1 and i=n_s-1, two conditions in (2.27) are invalid. Therefore, there are 4(n_s-1)-2 conditions. We can freely choose two additional conditions to solve the spline parameters. A boundary condition called natural condition is used in my code:

$$f_1''(x_1) = 0 \qquad f_{ns-1}''(x_{ns}) = 0 \tag{2.28}$$

The geometric meaning is that beyond the region of given points, interpolation function will be a straight line. This is a fair solution for most cases. The solution of interaction function is usually written as:

$$\begin{aligned} a_{i1} &= (u_{i+1} - u_i)/6h_i \\ a_{i2} &= (x_{i+1}u_i - x_i u_{i+1})/2h_i \\ a_{i3} &= \frac{(y_{i+1} - y_i)}{h_i} - \frac{(u_{i+1} - u_i)h_i}{6} - \frac{(x_{i+1}^2 u_i - x_i^2 u_{i+1})}{2h_i} \\ a_{i4} &= \frac{x_{i+1}^3 u_i - x_i^3 u_{i+1}}{6h_i} + \frac{x_{i+1}y_i - x_i y_{i+1}}{h_i} - \frac{(x_{i+1}u_i - x_i u_{i+1})h_i}{6} \end{aligned} \tag{2.29}$$

Sets of coefficients h and u are introduced for convenience, which are roots of the following linear equations:

$$
\begin{aligned}
&u_0 = 0 \\
&h_{i-1}u_{i-1} + 2\left(h_{i-1} + h_i\right)u_i + h_i u_{i+1} = 6\left(\frac{y_{i+1} - y_i}{h_i} - \frac{y_i - y_{i-1}}{h_{i-1}}\right) \\
&u_{ns} = 0
\end{aligned}
\tag{2.30}
$$

The cubic spline interpolation is an excellent candidate to eliminate the artificial discontinuity effect up to first order. However, it is more computation resource intensive than first order spline.

3. ELECTRON DISRUPTION EFFECT

In eRHIC the effect of beam-beam interaction on the electron beam is much larger than the effect on the proton beam, as one can see comparing the beam-beam parameters in Table 1.2. The electron beam is disrupted considerably by the beam-beam force just after one collision with protons, while proton beam distribution changes very slowly. In order to investigate the evolution of electron beam in one collision process, we can assume proton beam to be rigid. One can distinguish two different components of the electron beam disruption. First, the nonlinear character of the beam-beam force distorts the beam distribution at high transverse amplitudes and increases the RMS emittance of the electron beam. Second, the linear part of the beam-beam interaction (strong focusing) causes the electron distribution mismatch in the phase space with the aperture shape defined by the design lattice without collisions. Both effects need to be considered carefully to evaluate possible beam-loss after beam-beam interaction.

3.1. The Linear Mismatch

At the interaction region, no external electromagnetic fields exist in drift space, the only force exerted on electron beam is the beam-beam force from proton beam. Near axis, this force is linear. The single electron motion can be calculated from

Hill's Equation.

$$x'' + k^2(s)x = 0 \tag{3.1}$$

Here, $k(s)$ represents the beam-beam kick from proton beam. We set IP as s=0, and positive s corresponds to the head of proton bunch. Then electron beam travels from positive s to negative. In order to avoid confusion, we will express all electron quantities in the proton coordinate frame in this chapter. We know that the for electron-proton collision, the beam-beam effect is an attractive force in the transverse direction, i.e. $k^2(s) > 0$. The electrons will oscillate inside proton beam. If we denote $\lambda_s(s)$ as the proton longitudinal distribution function where two beams meets and have $\int\lambda_s(s)ds = 1$, $k(s)$ has the form:

$$k^2(s) = \frac{N_p r_e}{\sigma_{px}^2 \gamma_e}\lambda(s) = \frac{1}{f_e}\lambda(s) \tag{3.2}$$

Above, σ_{px} is transverse rms size of proton beam; r_e is classical radius of the electron. The collision position is at $s = z/2$, so we can get $\lambda_s(s)$ from the real proton longitudinal distribution $\lambda_z(z)$. The relation between two different functions gives:

$$\begin{aligned} &\int_{-\infty}^{\infty}\lambda_s(s)ds = \int_{-\infty}^{\infty}\lambda_z(z)dz \xrightarrow{z=2s} 2\int_{-\infty}^{\infty}\lambda_z(2s)ds \\ &\lambda_s(s = z/2) = 2\lambda_z(2s) \end{aligned} \tag{3.3}$$

After establishing the relation, we will use $\lambda(s) = \lambda_z(s)$ for simplicity. Usually a Gaussian distribution is good model for longitudinal position, which is

$$\lambda(z) = \frac{1}{\sqrt{2\pi}\sigma_{pz}}\exp\left(-\frac{z^2}{2\sigma_{pz}^2}\right) \tag{3.4}$$

Here σ_{pz} is the rms bunch length of proton beam.

Before proceeding further, we need to define the disruption parameter *d* as:

$$d_e = \sigma_{pz} / f_e = \frac{N r_e \sigma_{pz}}{\sigma_{px}^2 \gamma_e} \tag{3.5}$$

The disruption parameter for the electron beam is about 5.78, comparing with proton disruption parameter 0.005. Now (3.2) and Hill's equation can be expressed using disruption parameter as:

$$\begin{aligned} k^2(s) &= \frac{N_p r_e}{\sigma_{px}^2 \gamma_e} \lambda_s(s) = \frac{2d_e}{\sigma_{pz}} \lambda(2s) \\ x'' &+ \frac{2d_e}{\sigma_{pz}} \lambda(2s) x = 0 \end{aligned} \tag{3.6}$$

The easiest thing that can be calculated from (3.6) is the electron oscillation wave-number under beam-beam force:

$$\begin{aligned} n &= \frac{1}{2\pi} \int_{-\infty}^{\infty} k(s)\, ds \\ &= \frac{1}{2\pi} \sqrt{\frac{2d_e}{\sigma_{pz}}} \int_{-\infty}^{\infty} \sqrt{\lambda(2s)}\, ds = \frac{\sqrt{d_e}}{(2\pi)^{3/4}} \approx \frac{\sqrt{d_e}}{4} \end{aligned} \tag{3.7}$$

So, for single electron near axis, it will finish $0.25\times5.78^{1/2}=0.6$ oscillation periods. The envelope of electron beam will oscillate $2\times0.6=1.2$ oscillation periods[11].

Without beam-beam effect, the electron particle distribution always matches the design lattice. When linear beam-beam effect is considered, there is extra phase advance in interaction region; therefore the phase distribution of electron beam after beam-beam interaction cannot match the design lattice.

To make the discussion more quantitative, we can compare the beta and alpha functions between the value with beam-beam effect and design values. The

difference between betatron amplitude functions determines whether the beam can match the design lattice. The beta and alpha functions with beam-beam effect can be obtained from either statistics of the distribution, which can be calculated from code, or the envelope equation as shown below:

$$\begin{aligned} &w'' + k^2(s)w - 1/w^3 = 0 \\ &\beta(s) = w^2(s) \\ &\alpha(s) = -w(s)w'(s) \end{aligned} \tag{3.8}$$

where $k(s)$ is defined in (3.2). The boundary condition is at the negative infinity away from IP before collision theoretically. Due to quick attenuation of proton longitudinal distribution beyond 3 rms beam length, we can set the boundary condition at the entrance of interaction region where s = 3m. The value of beta and alpha function can be calculated from their design values at IP as:

$$\begin{aligned} &\beta(s) = \frac{1}{\gamma(0)} + \gamma(0)\left(s - \frac{\alpha(0)}{\gamma(0)}\right)^2 \\ &\alpha(s) = \alpha(0) - \gamma(0)s \end{aligned} \tag{3.9}$$

This evolution relation in drift space is just the solution of (3.8) when $k(s)$=0. By solving the differential equation with non zero $k(s)$, we can get the beta and alpha function evolution in whole interaction region with beam-beam interaction, as well as the values at the exit of interaction at s = -3m after interaction with proton beam. Then the two cases, with or without beam-beam effect, can be easily compared.

In (3.8), if $k(s)$ is proportional to a Gaussian distribution, the solution cannot be expressed in terms of fundamental functions. An over-simplified approximation is to assume the proton bunch is very short, i.e. $k(s)$ is proportional to $\delta(0)$. Then the beam-beam interaction is reduced to thin-length focusing quadrupole effect in both transverse directions. As we know, the betatron functions evolve through a thin

length quadrupole as:

$$\begin{aligned} \beta_2 &= \beta_1 \\ \alpha_2 &= \alpha_1 + \beta_1 / f \end{aligned} \tag{3.10}$$

This gives conclusion that we have to set beta at IP be zero to minimize mismatching effect, which is obviously impossible to achieve. But it educates us to seek for smaller beta for small mismatching effect.

A numerical solver can give the exact solution easily. According to Table 1.2, the designed beta waist is 1 meter and the waist position is at IP (s=0). The solution of beta and alpha function in interaction region are shown in (a) and (b) of Figure 3.1.

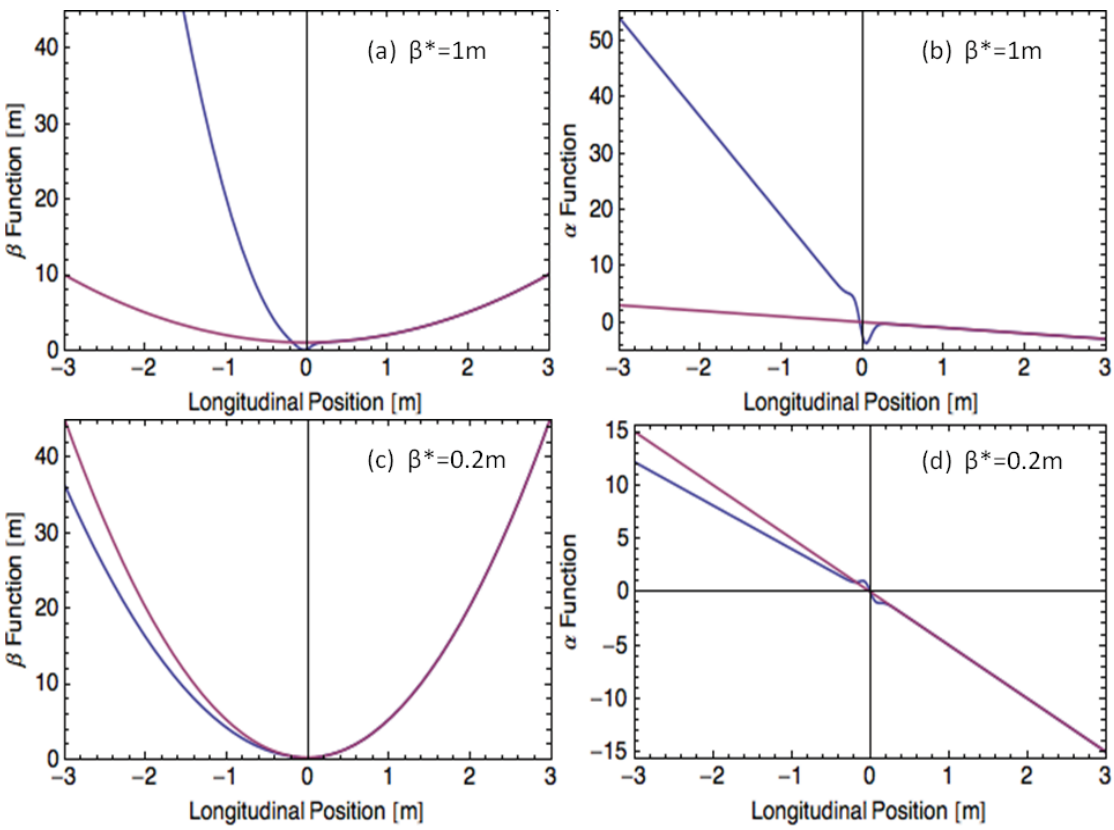

Figure 3.1: The numerical solution of equations in (3.8) is blue curve, while read curve corresponds to betatron amplitude function without beam-beam force. In (a) and (b), the initial beta function minimum is 1 meter; in (c) and (d) the initial beta function minimum is 0.2 meter. In all graphs, the initial beta waist position is at IP.

In Figure 3.1, the boundary condition is set at s=3m. For large positive longitudinal position, two curves overlap with each other because the beam-beam force is too weak. We observed that the mismatch is huge after collision if the waist β^* is one meter. From what we learned before, a smaller waist can contribute to reducing the mismatch. The numerical result of β^* =0.2m is shown in (c) and (d) of Figure 3.1. The mismatch is much smaller than the case β^* =1m. Compare these two cases, it is notable that for β^* =1m, the beta function after beam-beam collision is larger than the case without beam-beam effect; while for β^*=0.2m, the result is opposite. It is expected to have proper β^* for perfect matching. Then we are interested at the solution of:

$$\beta\left(\beta^*, s=-3m\right)=\beta^*+\frac{s^2}{\beta^*} \tag{3.11}$$

Numerical solution gives β^*=0.225m. In Figure 3.2, we show the case with perfect match. The betatron amplitude functions with beam-beam effect match functions without beam-beam force except longitudinal position near IP.

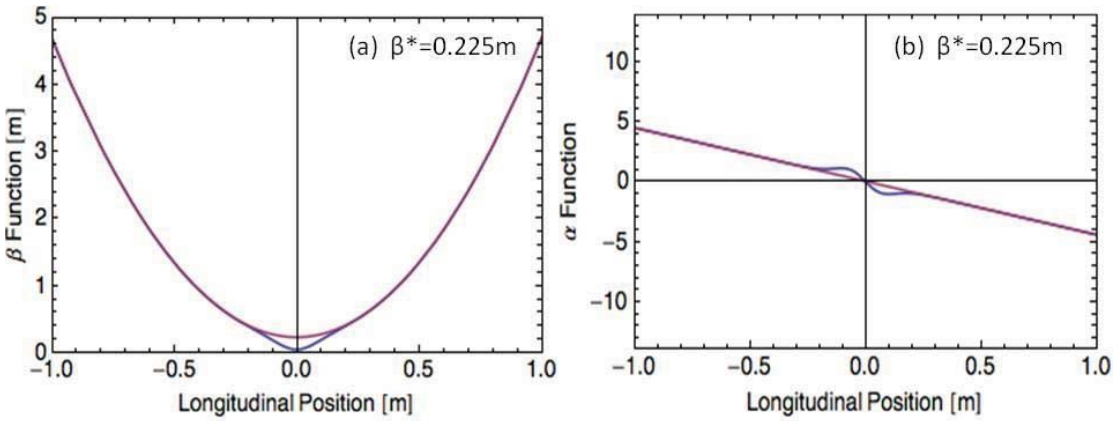

Figure 3.2: The numerical solution of equations in (3.8) is blue curve, while read curve corresponds to betatron amplitude function without beam-beam force. In (a) and (b), the initial beta function minimum is 0.225 meter, with waist position at IP.

Although we found that waist beta function of 0.225m at IP eliminates the

mismatch after beam-beam interaction, this is only valid for linear beam-beam force approximation. The result can be different when nonlinearity of beam-beam force is considered.

3.2. Nonlinear Disruption Effect

In the previous section, we discussed the electron distribution mismatch under linear beam-beam force. Simple results can be achieved by solving a linear differential equation. However, for electrons that are far from the axis, the beam-beam force is highly nonlinear. The nonlinearity of interaction can distort electron distribution from its original Gaussian form. Consequently, the betatron amplitude functions deviate from linear result of (3.8). Electron beam geometric emittance also changes under such a nonlinear force. We need to use simulations to determine the resulting deterioration.

First, we can calculate how the emittance changes and the evolution of rms beam size. The geometric emittance is expected to grow under nonlinear force. Simulation parameters are based on values in Table 1.2. The design electron β^* is 1 meter with beta waist position at IP. Both beams are assumed as 6-D Gaussian beam with 4 sigma cut off. So the proton coordinate range is from -0.8 meters to 0.8 meters relative to the reference particle. According to relation (3.3), the actual collision occurs from -0.4 meter to 0.4 meter relative to IP. The evolution of rms beam size and emittance is shown in Figure 3.3.

In Figure 3.3, the electron beam travels from positive longitudinal position to negative position. We can see the electron beam emittance increases by factor of 2 in the entire collision process. Mainly the emittance change happens in range of

[-0.2m, 0.2m], which corresponds to collisions with proton beam of longitudinal position $\pm 2\sigma_{pz}$. The beam size of the electron beam forms a 'pinch', which corresponds to the strong focusing by proton beam. Details of pinch effect on proton beam will be discussed in chapter 5.

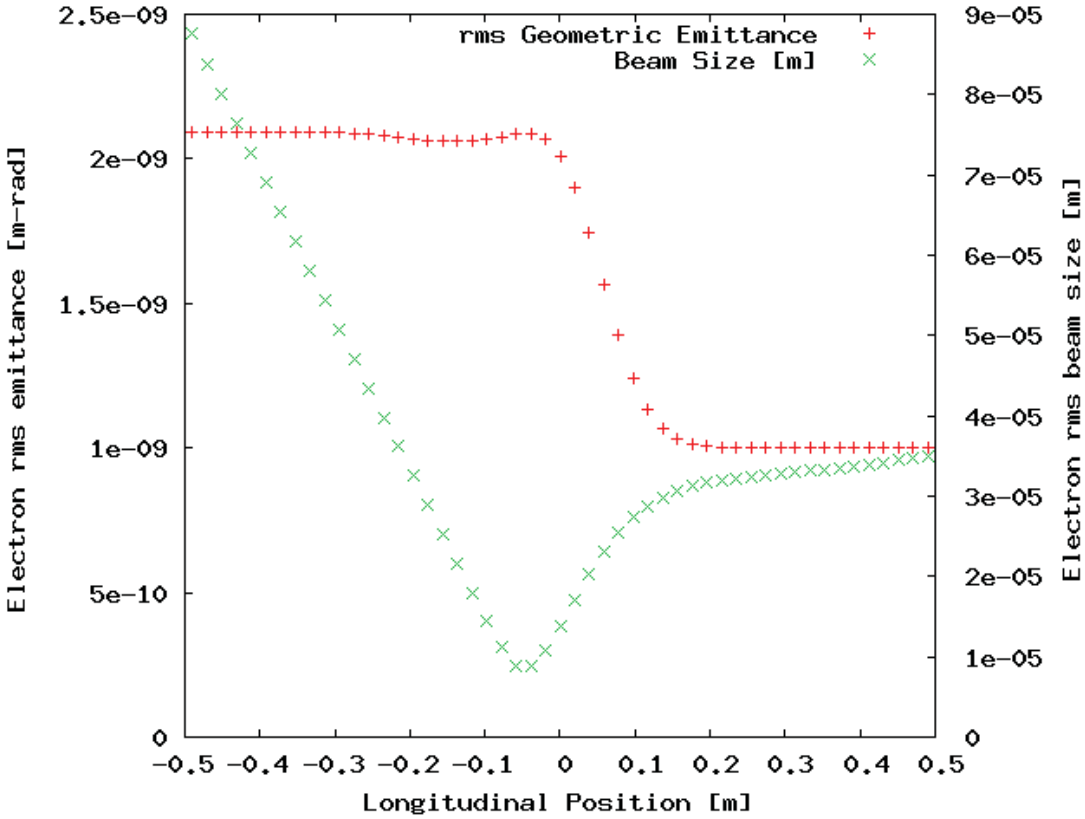

Figure 3.3: Evolution of Beam Size and Emittance of Electron Beam

Under nonlinear force, the proton beam distribution will be distorted from its original phase space shape, as seen in Figure 3.4. In order to easily compare with design optics without beam-beam effect, we transferred all macro-particles coordinates after beam-beam interaction back to IP position. Mathematically, the process is processed as:

$$\begin{aligned} \tilde{x}_e(s=0) &= x_e(s) - x_e'(s)s \\ \tilde{y}_e(s=0) &= y_e(s) - y_e'(s)s \end{aligned} \tag{3.12}$$

with s=-0.4meter. The coordinates with tildes represent the coordinate near IP. After getting the virtual distribution at IP, we can calculate the effective betatron amplitude function as:

$$\begin{pmatrix} \beta_x & -\alpha_x \\ -\alpha_x & \gamma_x \end{pmatrix} = \frac{1}{\varepsilon_x} \begin{pmatrix} \left\langle (x-\bar{x})^2 \right\rangle & \left\langle (x-\bar{x})(x'-\bar{x}') \right\rangle \\ \left\langle (x-\bar{x})(x'-\bar{x}') \right\rangle & \left\langle (x'-\bar{x}')^2 \right\rangle \end{pmatrix} \tag{3.13}$$

Here, ε_x represents the rms geometric emittance obtained from beam distribution, written as:

$$\varepsilon_x = \sqrt{\left\langle (x-\bar{x})^2 \right\rangle \left\langle (x'-\bar{x}')^2 \right\rangle - \left\langle (x-\bar{x})(x'-\bar{x}') \right\rangle^2} \tag{3.14}$$

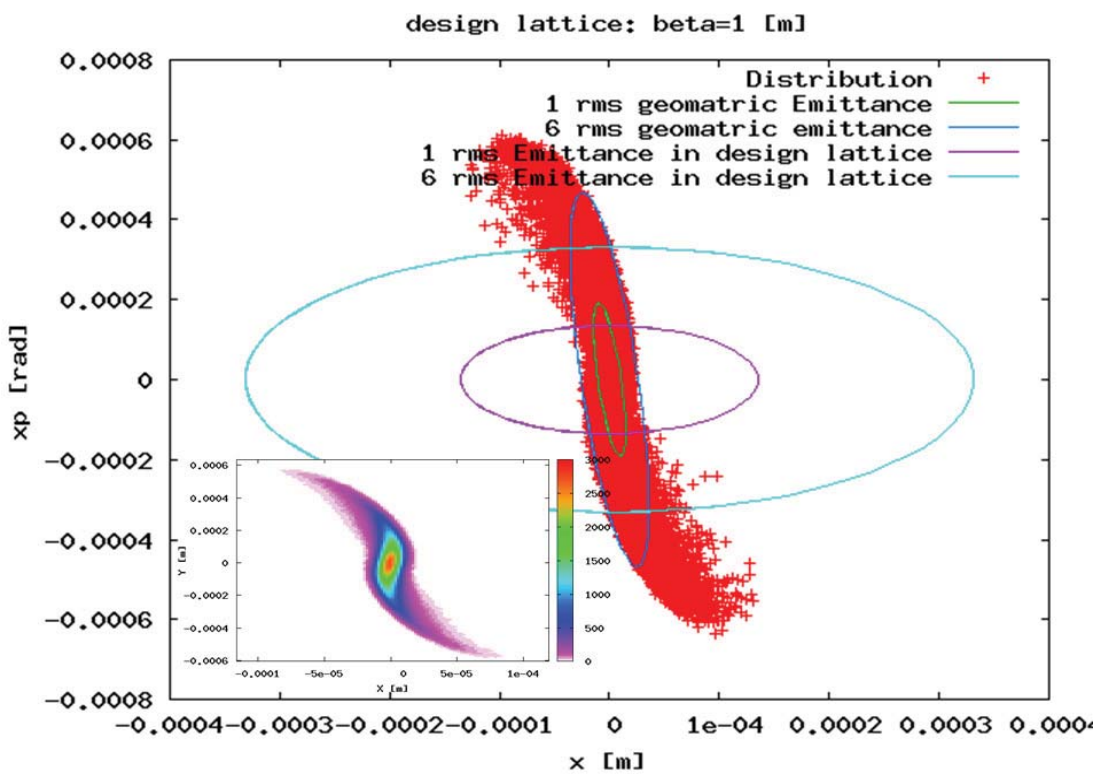

Figure 3.4: Phase space distribution of electron beam after collision for β^*=1m, back traced to the IP. Mismatch between the geometric emittance and Courant-Snyder invariant ellipse of design lattice.

Figure 3.4 shows the large mismatch between phase space distribution and the

design lattice. For design lattice at IP, the alpha function vanishes and Courant-Snyder invariant ellipse is upright with the ratio of semi-axis is $1/\beta$. From (3.13), we can calculate the effective beta and alpha function at IP gives:

$$\begin{aligned} \tilde{\beta}(s=0) &= 0.078\text{m} \\ \tilde{\alpha}(s=0) &= 0.59 \end{aligned} \tag{3.15}$$

After the collision, the electron beam is decelerated in the process of energy recovery and travels through several recirculation passes. The final electron emittance after the collision is very important, since magnets of recirculation passes as well as components of the superconducting linac must have sufficiently large aperture to accommodate the disrupted electron beam and avoid beam losses. For the purpose of evaluation of the acceptable magnet apertures it is reasonable to consider the final electron beam emittance defined not as the geometric emittance, but according to the emittance shape from the design lattice without collisions, diluting the real beam distribution in betatron phase to fill the emittance shape defined by the design lattice. Mathematically, the geometric emittance is defined in (3.14) and the effective emittance is defined as the half rms value of Courant-Snyder invariant of all macro-particles based on design lattice. The betatron amplitude function invariant C is:

$$C(\tilde{x},\tilde{x}') = \gamma\tilde{x}^2 + 2\alpha\tilde{x}\tilde{x}' + \beta\tilde{x}'^2 \tag{3.16}$$

In the above equation, the betatron amplitude function should be calculated at different longitudinal positions according to design optics. For the example of β^*=1m at IP, we can get the comparison of evolution of rms geometric emittance and effective emittance in Figure 3.5. In the figure we can see that the rms emittance growth in effective emittance due to mismatch is much larger than growth in geometric emittance which is only related to the nonlinear beam-beam force. Before

collision, the geometric emittance has exact same value as effective emittance because the beam distribution perfectly matches the optics. After the collision, in this case, the final rms effective emittance is about 9 times larger than geometric rms emittance, 18 times larger than original rms value. However, the geometric rms emittance growth is an intrinsic growth due to the nonlinearity, while beam mismatch largely depends on the design optics.

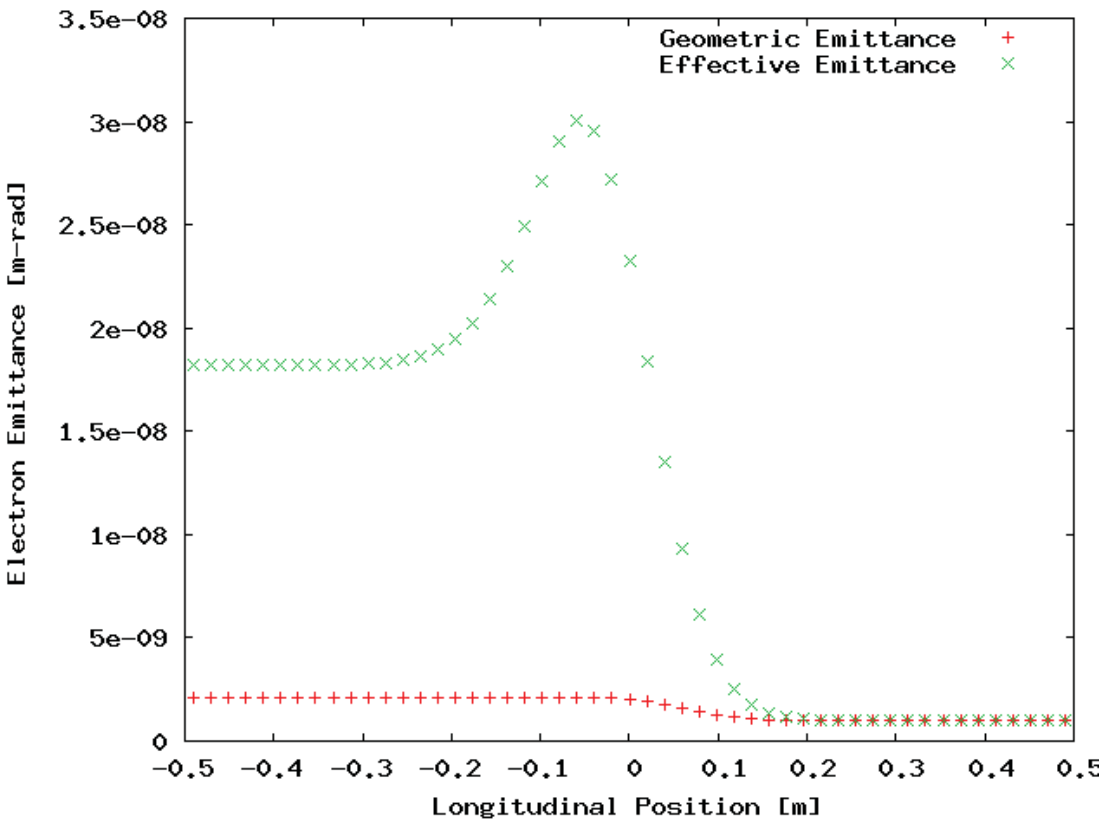

Figure 3.5: Comparison of rms geometric and effective emittance of electron beam in beam-beam interaction for β^*=1m

From the section 3.1, we know that the lattice mismatch is mainly a linear effect. It is expected that the mismatch can be reduced by properly choosing the betatron amplitude functions of the electron beam just as calculated in section 3.1. Since small designed β^* reduces mismatching from experience of linear force discussion, we can plot the rms emittance growth and rms beam size evolution in interaction region, for β^*=0.2 meter.

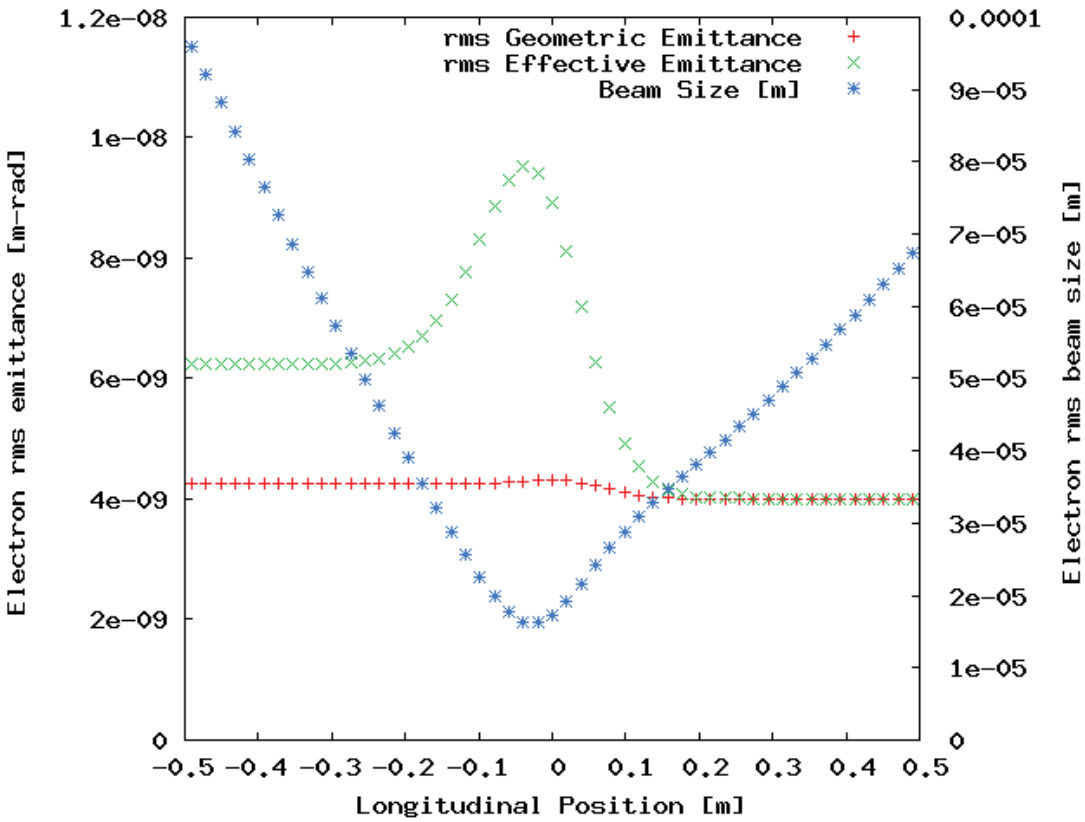

Figure 3.6: Evolution of beam size and rms emittance of electron beam for β^*=0.2m, both geometric and effective emittance.

From Figure 3.6, we can observe two advantages over large design β^*=1m. First the rms geometric emittance growth rate between initial emittance and its final value is low for low β^*. The emittance increase only about 4% compare with 100% in the case of β^*=1m. Second, the rms effective emittance after interaction has about 25% increment, far less than the huge rms effective emittance of β^*=1m. This is clearly a benefit from small mismatch, which is proved in Figure 3.7. And we can calculate the effective beta and alpha function from phase space distribution as:

$$\begin{aligned} \tilde{\beta}(s=0) &= 0.12\text{m} \\ \tilde{\alpha}(s=0) &= 0.249 \end{aligned} \tag{3.17}$$

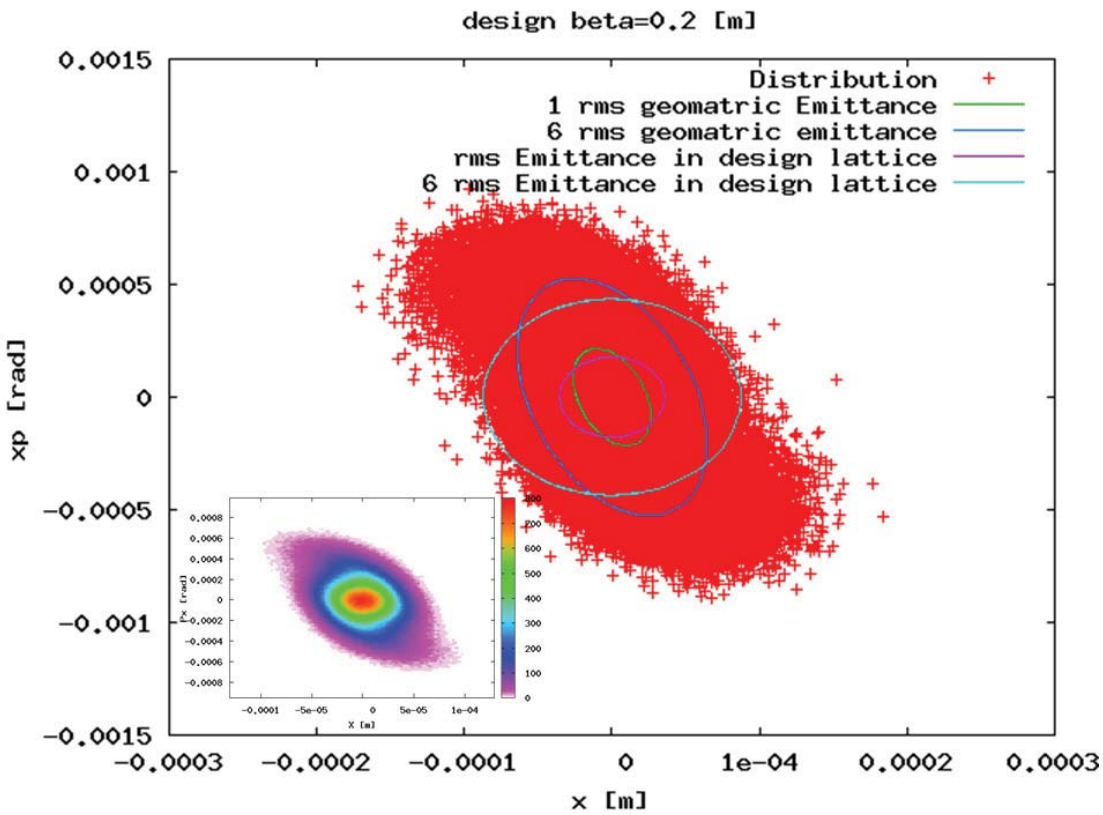

Figure 3.7: Phase space distribution of electron beam after collision for β^*=0.2m, back traced to IP. Mismatch between the geometric emittance and Courant-Snyder invariant ellipse of the design lattice

Usually nonlinear forces not only cause rms emittance growth, but also form a longer tail and a dense core at center of the electron beam distribution. The long tail beam distribution requires larger acceptance to prevent beam losses. Before the beam-beam collision, the electron beam distribution is Gaussian with 4 sigma cut off. We can expect that all macro-particles are covered by phase space ellipse of 16 rms emittance. However, after nonlinear beam-beam interaction, the long-tail will extend to at least 25 times the final rms emittance according to simulation results as shown in Table 3.1.

Table 3.1: Portion of particle be covered in certain emittance

# of rms emittance	Gaussian Distribution	Distribution after Beam-Beam effect (β^*=1m)	Distribution after Beam-Beam effect (β^*=0.2m)
2	63.2%	69.5%	64.0%
4	86.5%	90.9%	86.8%
6	95.0%	95.5%	94.9%
8	98.2%	96.9%	97.8%
10	99.3%	97.6%	99%
15	99.9%	98.6%	99.8%
20	100%	99.1%	99.9%
25	100%	99.4%	100%
30	100%	99.6%	100%

We can see that after beam-beam collision, the electron beam distribution deviates from initial Gaussian distribution. The deformed distribution tends to have dense core in center and long tail compare with Gaussian distribution.

Since we cannot allow much particle loss in the energy recovery path and Linac, it is important to consider 100% geometric and effective transverse electron emittance in addition to their rms values. For Gaussian distribution electron beam, it is apparent that 100% emittance values have direct dependence on the tail cut-off convention. Therefore, it is reasonable to study the 100% emittance as function of tail cut-off points.

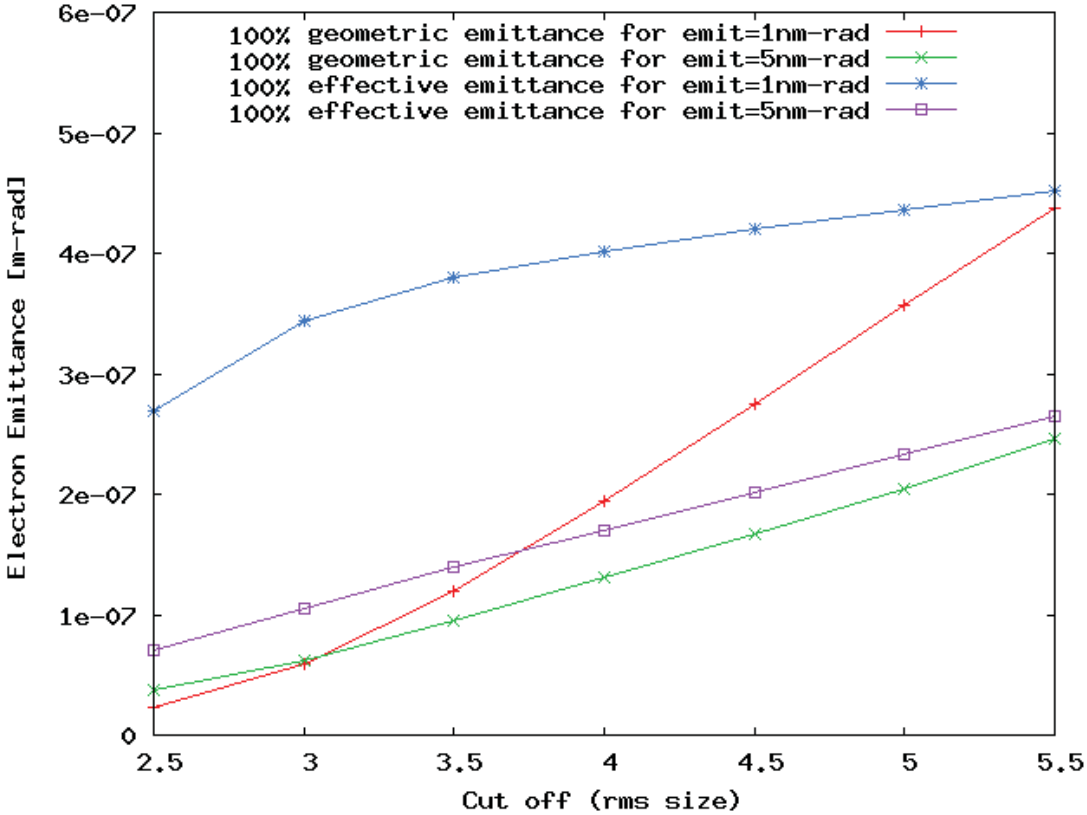

Figure 3.8: 100% electron geometric and effective emittance as function of cut off points for Gaussian distribution, for both large (initial rms emittance = 5nm-rad; β^*=0.2m) and small initial emittance (initial rms emittance = 1nm-rad; β^*=1m)

Figure 3.8 shows that there is still large discrepancy between 100% geometric emittance and effective emittance for small initial emittance case (1nm-rad). The discrepancy is getting smaller if initial electron emittance is set to a larger value (5nm-rad). The advantage of a large initial electron emittance is still obvious; it yields higher beam quality after beam-beam collision.

3.3. Luminosity Enhancement

Under strong focusing beam-beam force, the electron beam size shrinks from the designed beam size around interaction point. At specific points, the electron beam forms narrow 'pinch' as we already seen in Figure 3.3 and Figure 3.6 for different

initial conditions. This is usually referred as the pinch effect. Obviously, this effect will enhance the design luminosity from definition (1.1) by introducing smaller electron beam size in denominator of the integral.

By linear approximation, where the electron beam rms emittance is constant, the transverse rms beam size of electron beam is proportional to square root of beta function $\beta(s)^{1/2}$, which is $w(s)$ in equation (3.8). The enhanced luminosity can be expressed as:

$$
\begin{aligned}
&L = \int \frac{2N_p N_e \lambda(2s)\, fh}{2\pi\left[\sigma_{xp}^2(s) + w^2(s)\varepsilon_e\right]} ds \\
&w'' + k^2(s)w - 1/w^3 = 0 \\
&k^2(s) = \frac{2d_e}{\sigma_{pz}}\lambda(2s)
\end{aligned}
\tag{3.18}
$$

Here, proton and electron parameters are distinguished by subscript p and e. σ_{pz} is the proton rms bunch length and d_e is the electron disruption parameter defined in (3.5). In the first two equations of (3.18), both pinch effect and hourglass effect are included for calculating luminosity. If we set $k^2(s)$ to zero, the luminosity will be reduced due to hourglass effect of electron beam. When proper $k^2(s)$ is included, we can obtain enhanced luminosity due to pinch effect by solving (3.18).

Since the nonlinear portion of the beam-beam field is very strong for electron beam, linear theory won't give useful information on the electron rms beam size. More accurate results must be achieved from simulation, which considers strong nonlinearity of the beam-beam interaction. In the simulation code, we perform a numerical integral just as the first equation in (3.18) and get the luminosity enhancement.

Table 3.2: Luminosity of different initial electron beam parameters

Initial electron beam parameters			Luminosity [$cm^{-2}s^{-1}$]
Emittance [nm-rad]	β^* [m]	Waist position [m]	
1	1	0	3.7×10^{33}
1	1	1	2.8×10^{33}
4	0.25	0	3.3×10^{33}
5	0.2	0	3.0×10^{33}
10	0.1	0	2.3×10^{33}

From Table 3.2, we can see different luminosity for various initial electron beam parameter. As the initial beta function at the waist position decreases, the luminosity decreases too because of the hourglass effect. Also we can control the luminosity by adjusting the waist position.

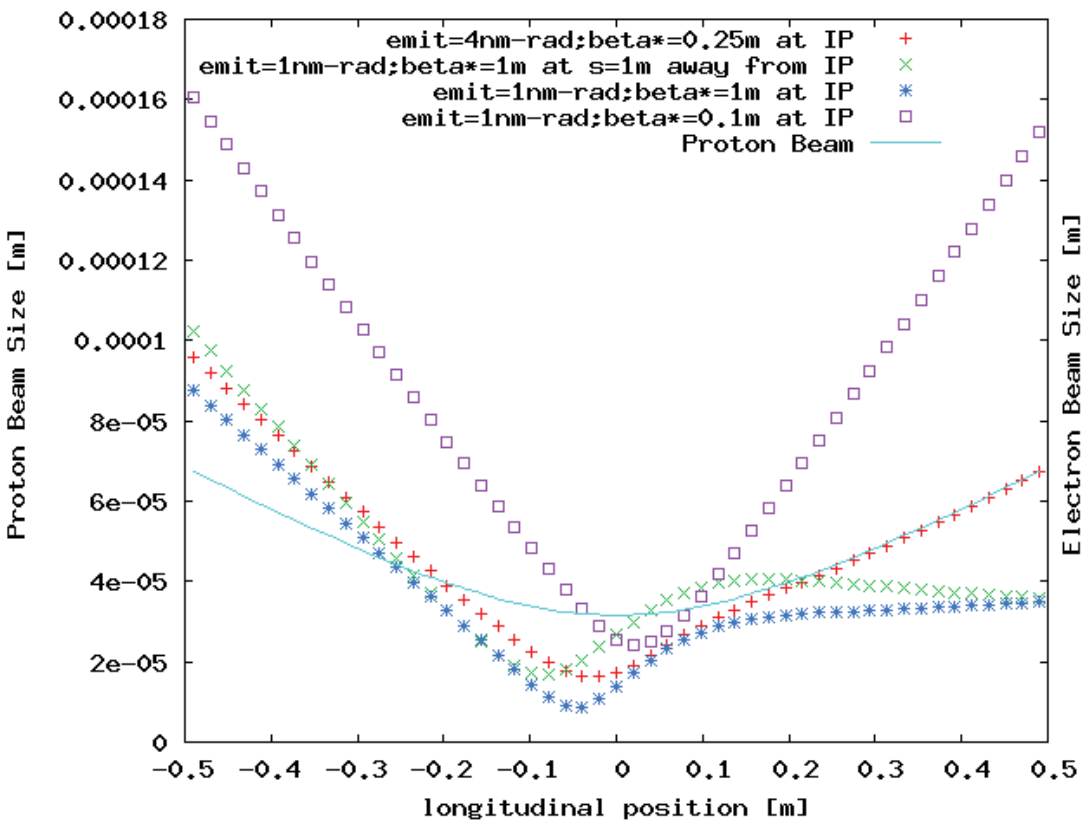

Figure 3.9: Electron and Proton rms beam size as function of longitudinal position

In Figure 3.9, we show the rms beam size change for each item in Table 3.2. This is the main reason that the luminosity deviate from its design value. In this case, we assume that, although the electron beam is disrupted by beam-beam force, the transverse distribution is almost Gaussian distribution. Because (3.18) and (1.1) are only valid for a transverse Gaussian distribution. As we will reveal in chapter 5, for large emittance and small β*, even though there is disruption effect on electron beam, the Gaussian distribution is still a good approximation and the luminosity we get in this section has good accuracy.

3.4. Transverse Beer-Can Distribution Electron Beam

Discussions of all sections in this chapter are under assumption that the electron beam has transverse Gaussian distribution (with 4 sigma cut-off) before colliding with proton beam. But this assumption is valid only when electron beam travels much longer than the order of corresponding damping time of specific transverse direction.

As we know, when the electron beam is bent during acceleration, electron radiates energy by synchrotron radiation. On one hand, the radiation causes transverse phase space damping and the damping process will not stop until the transverse phase space area is zero. On the other hand, the synchrotron radiation is a quantum process. The lost energy from electron beam is discrete and has random Poisson distribution, which cause excitation on electron beam. Besides synchrotron radiation, the magnet alignment errors also contribute the electron beam excitation. As a result, the transverse phase space distribution will reach balance between the damping effect and quantum excitation. The dynamics system can be express as a simple 1-D system with (x,p) as conjugate coordinates

$$x' = p, \qquad p' = -\frac{dU(x)}{dx}, \tag{3.19}$$

where the prime represents the derivative with respective to time t. The Hamiltonian is very simple: $H=p^2/2+U(x)$. Now we can add damping and quantum excitation to the system as:

$$x' = p, \qquad p' = -\frac{dU(x)}{dx} - Ap + Dw(t) \tag{3.20}$$

Here A corresponds to the damping effect and $Dw(t)$ represents quantum excitation. D serves as the excitation amplitude and the random function $w(t)$ is normalized white noise function which satisfies:

$$\langle w(t) \rangle = 0, \qquad \langle w(t)\, w(t') \rangle = \delta(t - t') \tag{3.21}$$

Let $\Psi(x,p)$ represent the distribution function, after simple steps we can get the time evolution of distribution function combined with(3.20):

$$\frac{\partial \Psi}{\partial t} = \left(-p\frac{\partial}{\partial x} + A\frac{\partial}{\partial p}p + \frac{dU}{dx}\frac{\partial}{\partial p} + \frac{D^2}{2}\frac{\partial^2}{\partial p^2} \right)\Psi \tag{3.22}$$

This formula is referred as Fokker-Plank Equation. The equilibrium solution gives:

$$\begin{aligned} \Psi(x,p) &\propto \exp(-H/E_0) \\ &\propto \exp\left(-\left(p^2/2 + x^2\right)/E_0\right) \end{aligned} \tag{3.23}$$

The equilibrium distribution we get is Gaussian distribution in both conjugate coordinates. The constant E_0 equals $D^2/2A$, which is the thermal energy. The time that one system takes to reach equilibrium can be estimated by the order of its

damping time. The damping time for electron machine is usually on the order of milliseconds.

For the current ERL design, the electron beam travels 5 turns and reaches its maximum energy, 10GeV, before colliding with proton beam. Each turn, the circumference is very close to the RHIC circumference 3833 meters. Therefore, before collision, it takes 64 microseconds for electron to travel from the entrance of ERL to interaction region. This interval is two orders of magnitude smaller than typical time that electron beam needs to reach equilibrium.

The above discussion reveals that the transverse distribution of the electron beam may not be a Gaussian-like distribution before colliding with proton beam. The real distribution should be half way between the initial electron distribution when electron beam just escapes from electron cathode and Gaussian distribution. Usually, the Beer-Can distribution is used to model electron beams in electron source studies. We also need to study the electron beam property after collision if the electron transverse distribution before collision is the Beer-Can type.

Suppose an electron beam with Beer-Can distribution with rms value of σ, there is a hard edge (Figure 3.10) for the beam distribution boundary, which is 2σ. This shows main difference between Gaussian distribution and Beer-Can distribution. For Gaussian beam, it has much longer tail (even with 4σ cut-off) than the Beer-Can beam. If the proton beam size equals electron beam size, the tail of the electron beam will experience nonlinear force according to Figure 2.1. So we are expecting benefit from the result of Beer-Can beam simulation because high portion of electron undergo linear beam-beam force from the electron beam.

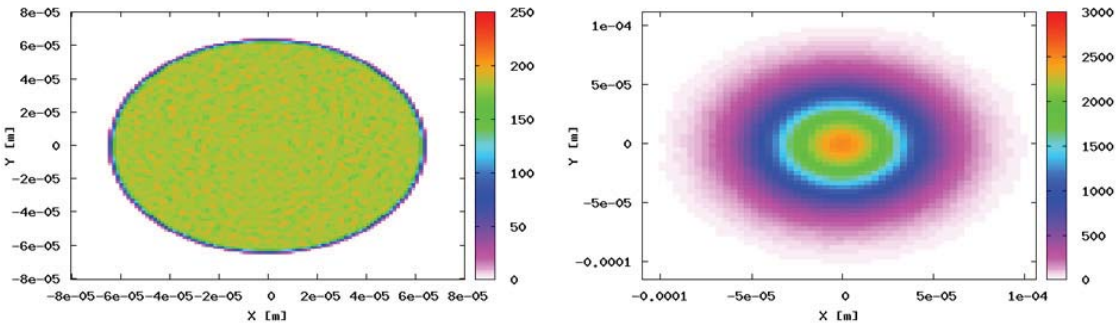

Figure 3.10: Transverse picture of Beer-Can distribution (left) and Gaussian distribution (right) for round beam with same rms beam size $\sigma=3.1\times10^{-5}$m.

It is worthwhile to note that if we collide a proton beam with a transverse Gaussian distribution with Beer-Can distribution electron beam, the resulting luminosity will be different from (1.1) which is for transverse Gaussian-Gaussian distribution beam collisions.

For transverse Beer-Can distribution electron beam colliding with proton beam, the luminosity needs to be calculated by integration as:

$$L = \iint dxdy\rho_p(x,y)\rho_e(x,y)fh \tag{3.24}$$

Here, ρ represents the beam transverse density function, and infinite short bunches are assumed. Other variables have same meaning as (1.1). If both densities are in Gaussian form, we simply rebuild (1.1). Now we use the following expressions for Gaussian and Beer-Can distribution respectively.

$$\begin{aligned}\rho_p &= \frac{N_p}{2\pi\sigma_{px}^2}\exp\left(-\frac{x^2}{2\sigma_{px}^2}-\frac{y^2}{2\sigma_{px}^2}\right)=\frac{N_p}{2\pi\sigma_{px}^2}\exp\left(-\frac{r^2}{2\sigma_{px}^2}\right)\\ \rho_e &= \frac{N_e}{4\pi\sigma_{ex}^2}H\left(2\sigma_{ex}-r\right)\end{aligned} \tag{3.25}$$

We already take the fact into account that both beams are round. The explicit luminosity expression gives:

$$L = \frac{N_p N_e f h}{4\pi\sigma_{ex}^2}\left[1 - \exp\left(-\frac{2\sigma_{ex}^2}{\sigma_{px}^2}\right)\right] \tag{3.26}$$

If proton and electron beams are matched, i.e. both transverse rms beam size are the same, we can compare the luminosity of 'Gaussian-BeerCan' collision and 'Gaussian-Gaussian' collision with same electron intensity.

$$L_{GB} / L_{GG} = 1 - e^{-2} = 0.865 \tag{3.27}$$

Here subscript GB and GG represents 'Gaussian-Beer-Can' collision and 'Gaussian-Gaussian' collision respectively. This indicates that a Beer-Can distribution electron beam requires 15.6% more intensity to achieve the same luminosity as the value of electron beam with a Gaussian transverse distribution.

First we perform same simulation as we did in section 3.2 for Gaussian electron beam. With the original parameter values, β^*=1m at IP and initial electron emittance 1nm-rad, we get the beam size and emittance evolution graph (Figure 3.11) as before.

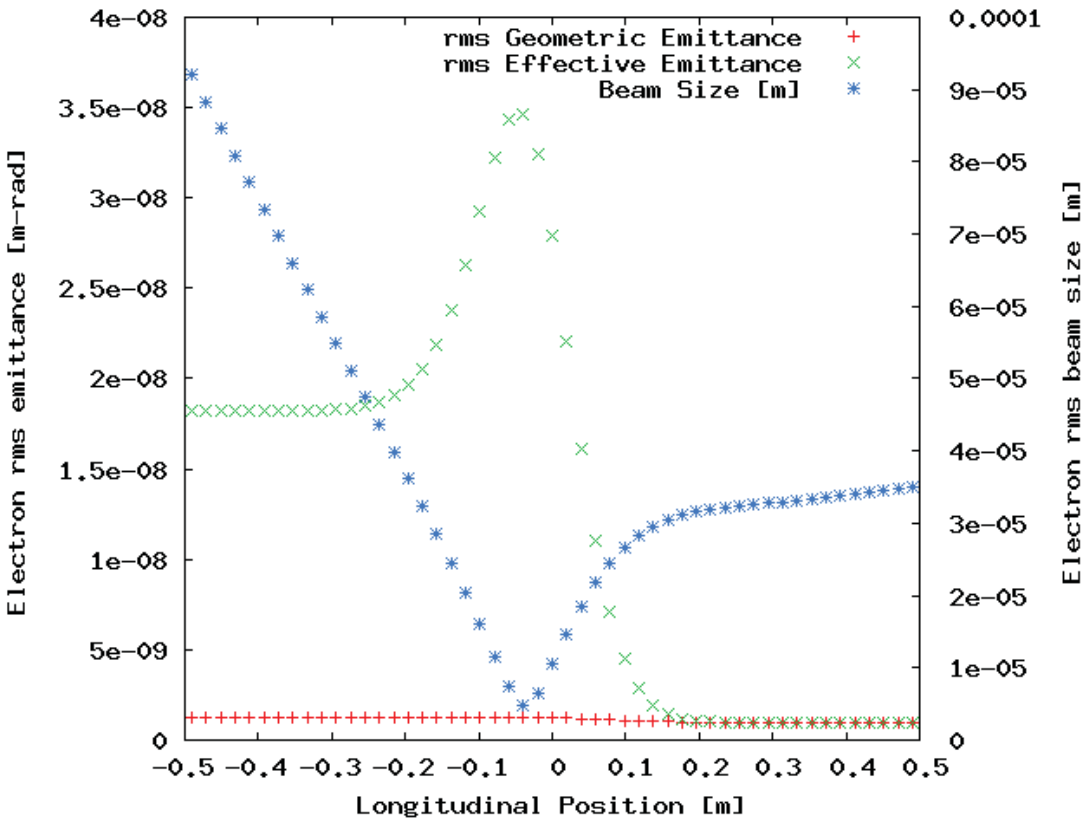

Figure 3.11: Evolution of beam size and rms emittance of electron beam for β^*=1m and initial Beer-Can transverse distribution, both geometric and effective emittance.

By comparing Figure 3.11 with Figure 3.3 and Figure 3.5, we can see that the rms geometric emittance growth is negligible for Bear-Can transverse distribution case compared with Gaussian distribution. But if the mismatch effect is considered, the final effective rms emittance for Beer-Can distribution is very close to the value of Gaussian distribution according to Figure 3.5.

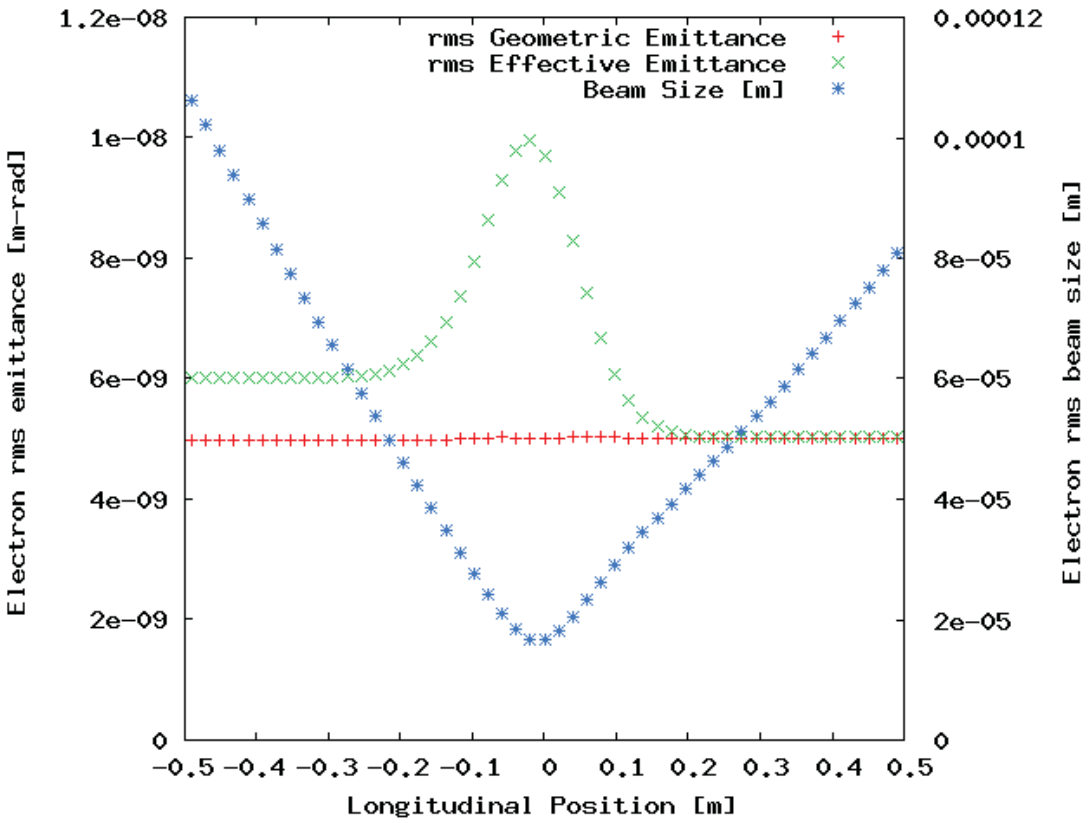

Figure 3.12: Evolution of beam size and rms emittance of electron beam for β^*=0.2m and initial Beer-Can transverse distribution, both geometric and effective emittance.

If we reduce β^* and increase the initial electron beam rms emittance to (β^*=0.2m, initial emittance = 5 nm-rad), the mismatch is expected to be suppressed as shown in Gaussian distribution case. For Beer-Can distribution, it is also valid as indicated in Figure 3.12. The final rms effective emittance is similar to Gaussian distribution case in Figure 3.6. Although the geometric emittance does not has obvious growth, the final rms geometric emittance for small is still larger than β^*=1m case.

After simple comparison, the rms geometric emittance improvement is observed in transverse Beer-Can distribution results, as we expected. But rms effective emittance (considering mismatch) does not show much difference because mismatch is a linear effect.

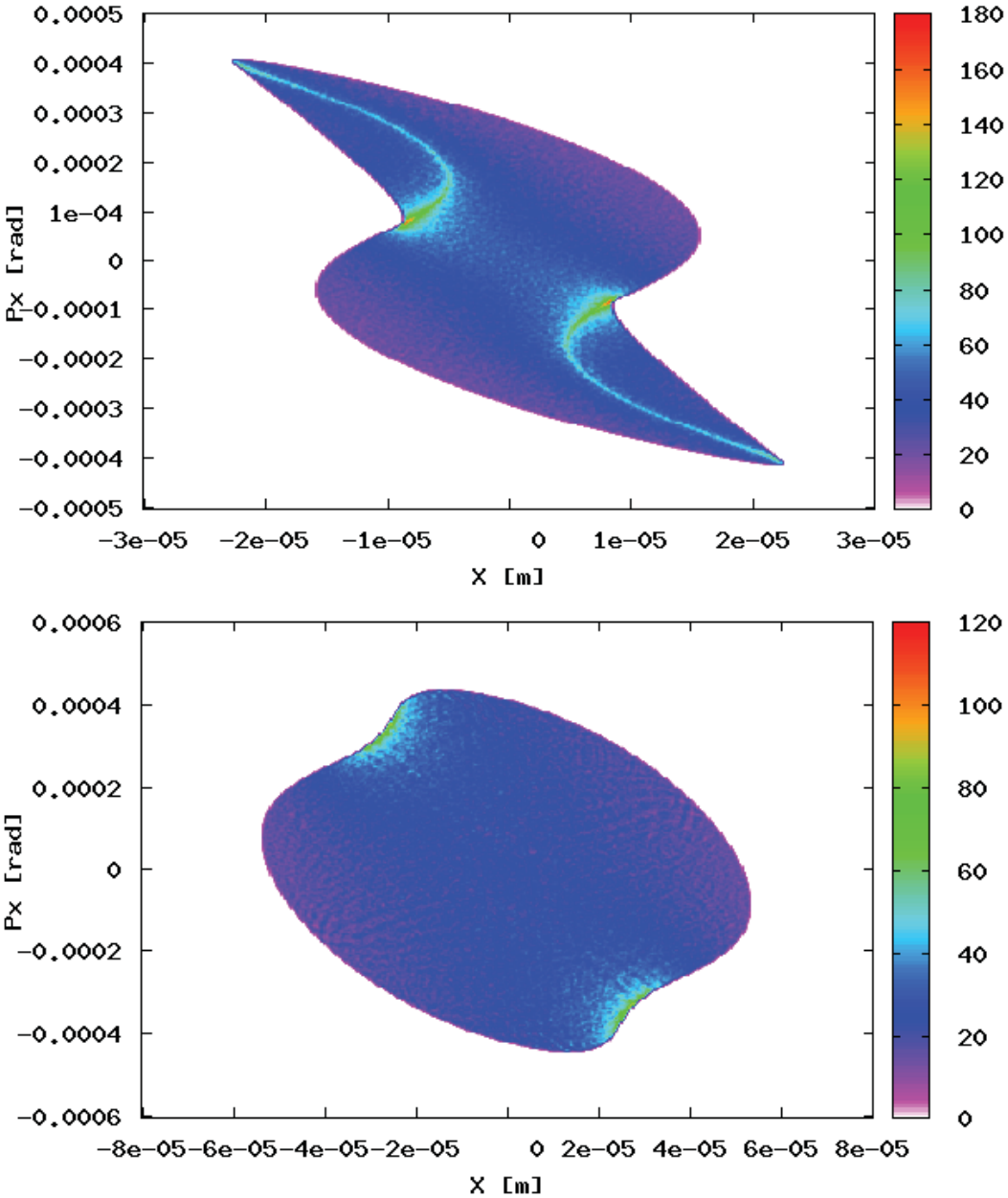

Figure 3.13: Phase space map after collision of initial Beer-Can distribution Electron beam, the figure corresponds to initial transverse rms emittance 1×10^{-9} m-rad and β^*=1m; the bottom one corresponds to initial rms emittance 5×10^{-9} m-rad and β^*=0.2m.

The phase space map of Figure 3.13 indicates that the distribution still has much sharper edge than Gaussian distribution after beam-beam collision. And again, we can see smaller beam disruption and mismatch for large initial rms emittance. Therefore, for initial Beer-Can distribution, the initial condition with large rms emittance and small waist beta function is preferred, which is same result as we saw for initial

Gaussian distribution case.

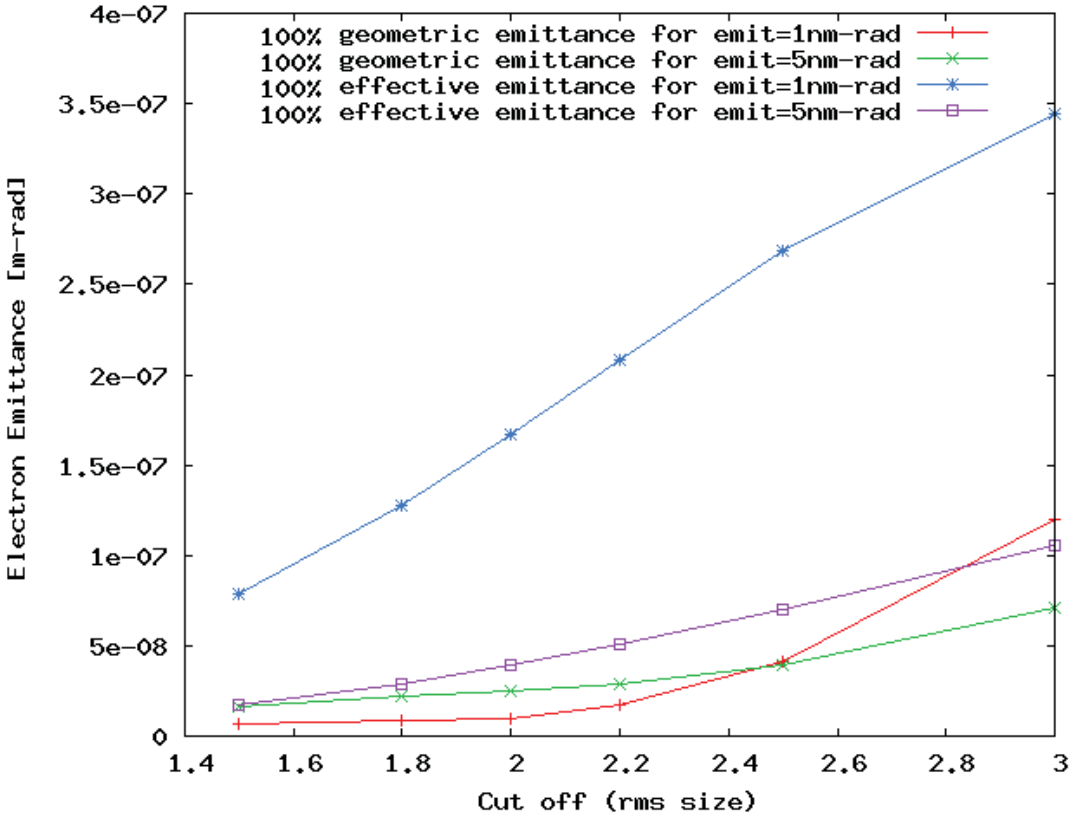

Figure 3.14: 100% electron geometric and effective emittance as function of cut off points for Beer-Can distribution, for both large (initial rms emittance = 5nm-rad; β^*=0.2m) and small initial emittance (initial rms emittance = 1nm-rad; β^*=1m)

Although Beer-Can distribution ideally has hard edge at boundary at twice transverse rms sizes, it is safe to study 100% emittance at different cut-off values to investigate tolerance near twice rms sizes. Similar to the Gaussian distribution, a large initial electron rms emittance (5nm-rad) reduces mismatch effect and yields smaller final emittance. For geometric emittance, the result for Beer-Can distribution is different from Gaussian distribution case. The small initial rms emittance (1nm-rad) yields smaller final geometric emittance, because the nonlinear effect is not strong at the edge of Beer-Can distribution.

3.5. Electron Beam Optics Optimization

From discussion in the section above, both final geometric emittance and effective emittance improve when electron design optics changes from β^*=1 m to β^*=0.2 m. Unlike linear theory, it is impossible to predict a specific optics function to minimize the mismatch after beam-beam interaction and electron beam loss. In simulation, the process of prediction is replaced by searching from variety of electron beam initial emittance and reasonable lattices.

During the simulations the following parameters were varied: initial electron beam emittance just before entering interaction region, design electron beta-function waist (beta function minimum) and electron beta-function waist position. The initial emittance and waist beta function determine the rms electron beam size before collision. The position of the waist of the electron beta-function presents an important parameter as well. Intuitively, having diverging electron beam (with alpha function negative) before entering collision region, should be helpful for the reduction of the pinch effect. If we persist the beam size matching condition, which means two beam transverse rms size equal with each other, only two parameters of emittance, beta and alpha function are independent variables.

Let us first ignore the beam size match condition. Then all three parameters are free in simulation. As the output of simulation, we can get the final luminosity, the rms emittance (both geometric and effective emittance) and the 100% emittance that cover all macro-particles. The luminosity deviates from nominal value in the design table, because we gave up matching condition in addition to the electron beam

distortion which is due to pinch effect and hourglass effect. It is worthwhile to note that a 100% emittance for a Gaussian beam is infinite. But in the simulation, since our macro-particles distribution has 4-sigma cut-off initially, we can get a finite 100% emittance using large amount of macro-particles.

Table 3.3: Test parameter table (design values is marked with $^{\#}$)

Initial Electron Emittance ($\times 10^{-9}$ m-rad)	$1^{\#}$, 2, 3, 4, 5, 6, 7, 8
Electron Beta Function at Waist (m)	0.1, 0.2, 0.4, 0.6, 0.8, $1^{\#}$, 1.5, 2
Electron Beta Function Waist Position from IP (m)	-0.5, -0.4, -0.3, -0.2, -0.1, -0.05, $0^{\#}$, 0.1, 0.2

For a reasonable comparison, we group all the output as function of final luminosity, because the luminosity is most important parameter in collider design.

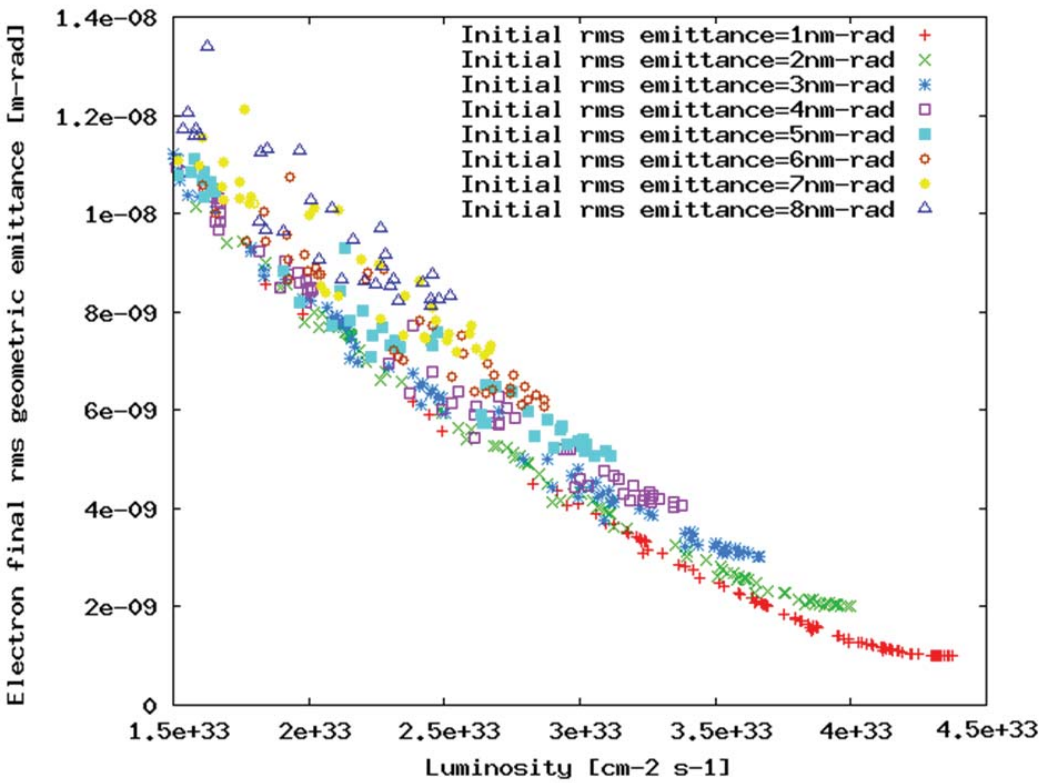

Figure 3.15: Electron rms geometric emittance after collision as function of luminosity

Figure 3.15 through Figure 3.17 illustrate simulation results for dependencies of various electron beam parameters related to beam loss (rms geometric emittance, rms effective emittance and the 100% effective emittance after collision based on the design lattice) on the luminosity. Different symbols correspond to different initial electron beam emittance. Each set of points for an individual initial emittance includes the points corresponding to various beta functions and beta function waist positions from Table 3.3.

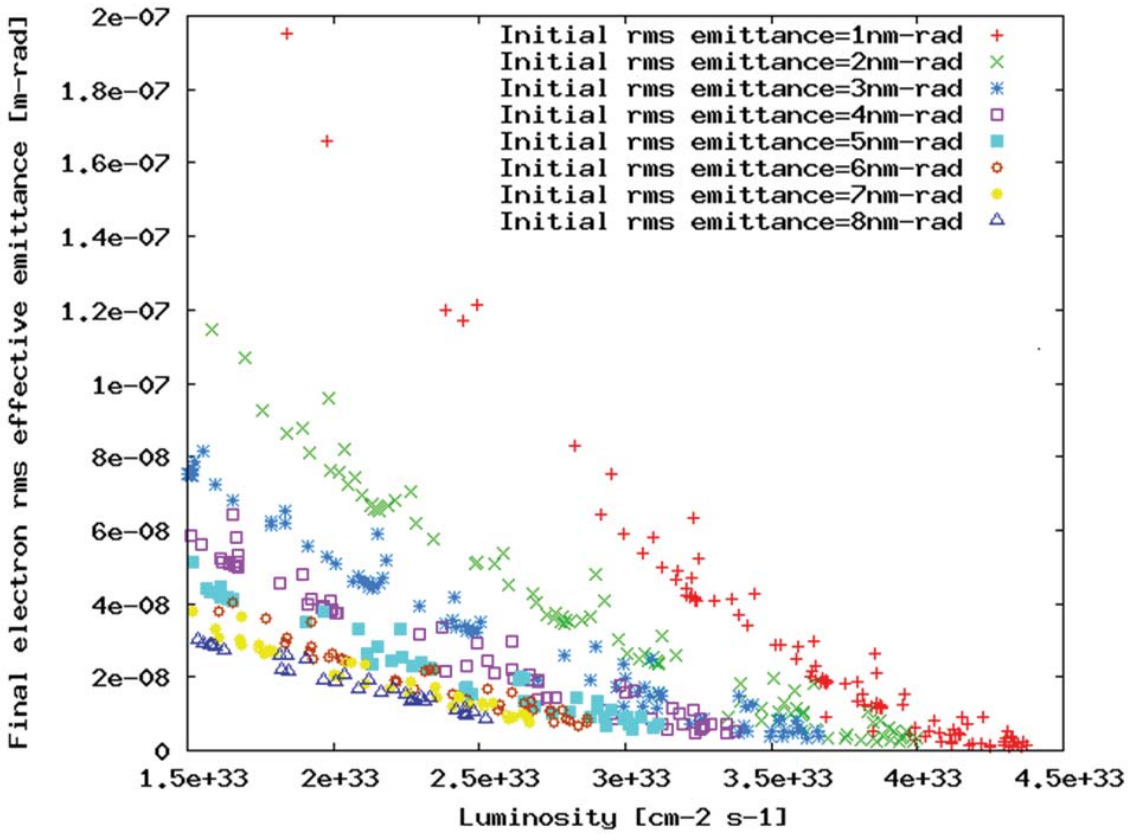

Figure 3.16: Electron rms effective emittance after collision as function of luminosity, the legend shows different initial electron emittance with unit $\times 10^{-9}$ m-rad

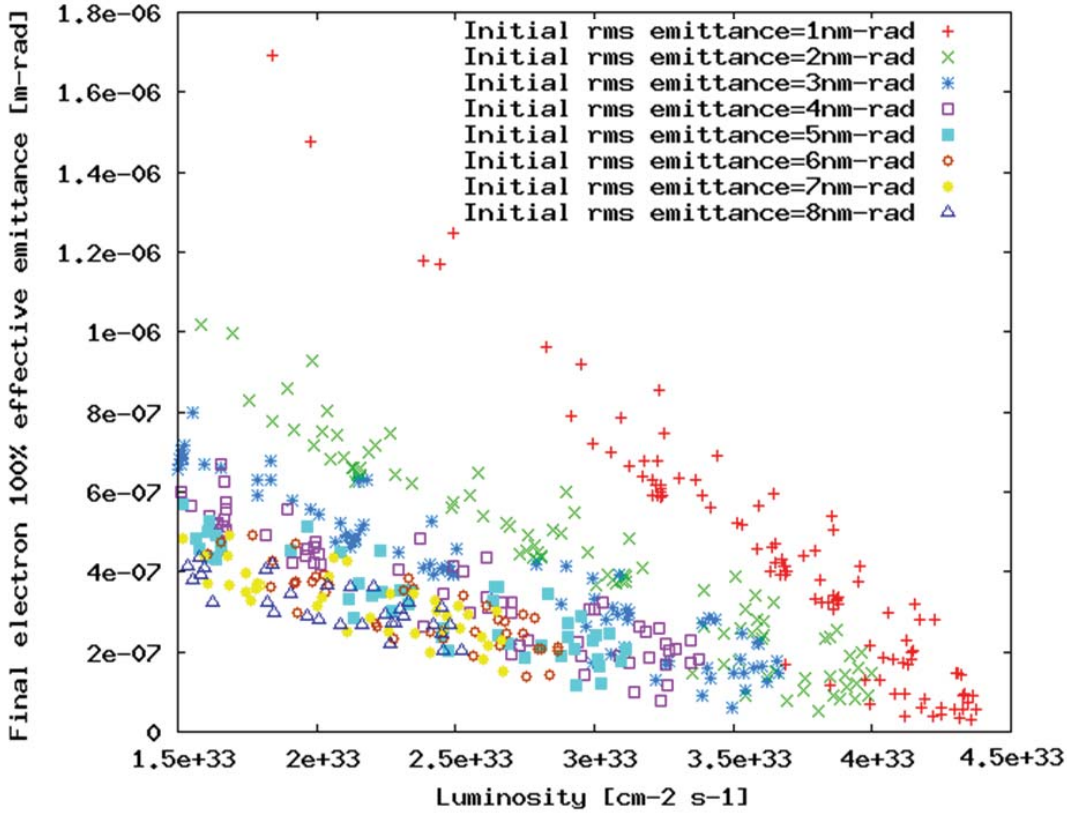

Figure 3.17: Electron 100% effective emittance after collision as function of luminosity, the legend shows different initial electron emittance with unit $\times 10^{-9}$ m-rad

Figure 3.15 shows rms geometric emittance after collision versus luminosity. A remarkable feature is that the final rms emittance only weakly depends on the initial electron emittance for the same final luminosity value at a specific luminosity. If those weak dependence is observed carefully, the final rms geometric emittance moves in the same direction as the initial rms electron emittance changes its value. Since the dependence is weak, the ratio of emittance grow is much larger for low initial rms emittance than large ones. At about 40% accuracy, the rms geometric emittance after collision is a linear function of resulting luminosity. A conclusion can be made that if we can achieve higher luminosity, a lower final rms geometric emittance will be automatically obtained. This statement is valid from Figure 3.15 to Figure 3.17.

The rms effective emittance of the electron beam after collision based on the

design lattice, on the contrary, depends on the initial emittance (as seen in Figure 3.16). For different initial electron emittance, it is also a linear function of resulting luminosity with different slope and intercept. For one target luminosity, in order to achieve smaller final rms effective emittance, one need higher initial emittance. This is the opposite relation compared with the result of rms geometric emittance.

To prevent beam loss, we need to pay more attention to the 100% effective electron emittance after collision. From Figure 3.17, the relation is very similar to the case of rms effective emittance. For any given luminosity, large initial emittance is preferred for a small final 100% emittance and less beam loss after collision. When the initial emittance is larger than 4nm-rad, the improvement of reducing 100% effective emittance becomes negligible.

Because a large emittance electron beam is hard to achieve from a linac, we can conclude from Figure 3.15 to Figure 3.17 that, for minimizing the final electron emittance and beam loss after the collision, an initial rms emittance of electron beam should be increase to 4 nm-rad or 5 nm-rad from the design value 1 nm-rad.

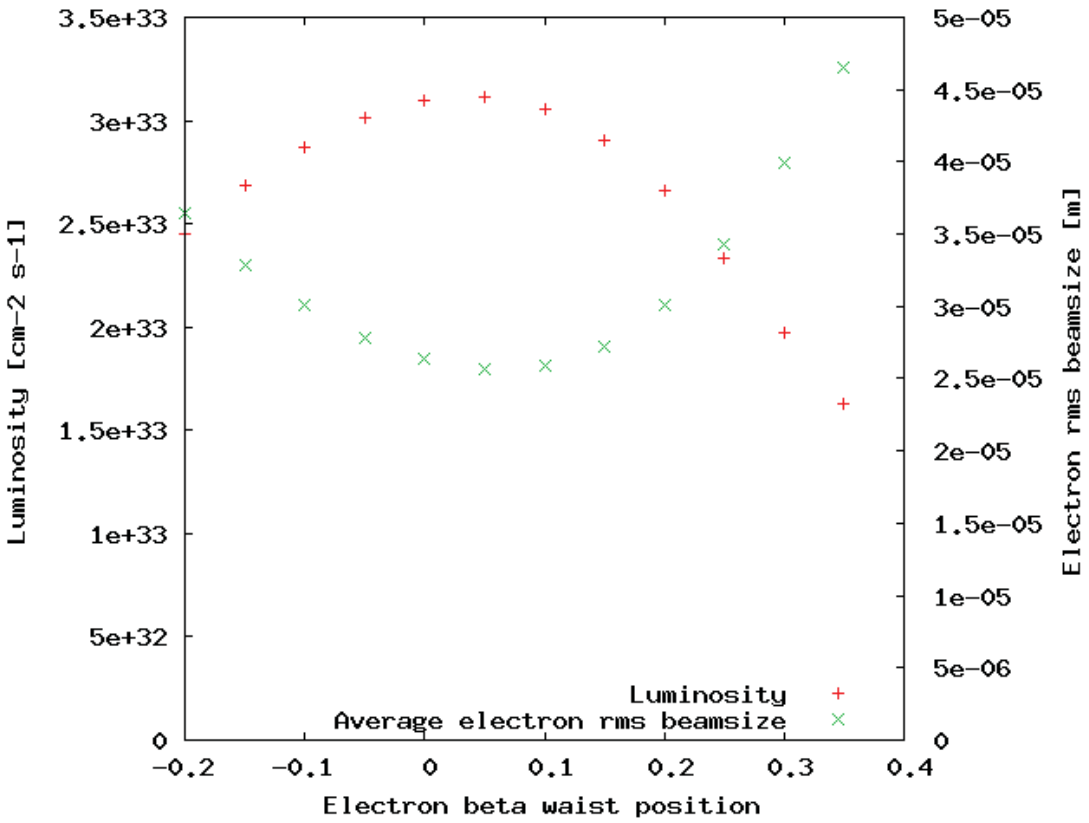

Figure 3.18: Luminosity and electron beam size dependence as function of waist position.

For electron beam loss study, we can apply matching condition to simplify the discussion. If we change the initial rms emittance of electron beam to 4 nm-rad or 5 nm-rad, the β^* at waist position should be 0.25m or 0.20m correspondingly. And now the free parameter is the waist position. Figure 3.18 shows the dependence of luminosity and electron beam size as function of waist position when the initial electron rms emittance is 5 nm-rad and β^* is 0.2m. We can get maximum luminosity when the waist position sits on IP. At the same time, we yield minimum rms electron beam size. Usually it is dangerous for proton beam as we will see in chapter 0. By adjusting the waist position, we can sacrifice luminosity to gain larger electron rms beam size.

3.6. Beam Loss Estimation and Matching

Based on discussion of electron beam disruption and mismatch with designed optics, we can calculate the electron beam loss downstream after beam-beam interaction for a given aperture of the energy recovery path [12]. The evaluation needs the following assumptions:

- After collision, only linear optics is present. Normalized beam emittance is conserved.
- The average beta function at energy recovery pass is 50 meters
- According to the optimization result, initial electron rms emittance is set to 0.2 nm-rad and β^* is 0.2 meters.

The electron beam will be decelerated after beam-beam interaction in the linac, which is exact reverse process as it being accelerated. The lowest energy in energy recovery path is around 1.75GeV for the low energy setup and 2.4GeV for high energy setup. Then the beam will be decelerated in main linac for the last time and the beam energy drops to 0.5GeV. The beam geometric emittance increases as the beam energy decreases. Because the normalized rms emittance for electron beam $\gamma\beta\varepsilon$ remains constant during decelerating. The beam loss happens when some electrons with large amplitude exceeds the aperture of energy recovery pass or linac.

Unquestionablely, for fixed top energy, the number of lost electron will increase as the energy decreases. But the power loss needs to be calculated carefully. The power loss gives:

$$
\begin{aligned}
P &= 2mc^2\gamma f\int_a^\infty \rho(r)\,r\,dr \\
&\xrightarrow{r^2=2\beta J/\gamma} 2mc^2\beta f\int_{a^2\gamma/2\beta}^\infty \rho(J)\,dJ
\end{aligned}
\tag{3.28}
$$

The energy dependence of power loss gives:

$$
\frac{dP}{d\gamma} = -mc^2 f a^2 \rho\left(\frac{\alpha^2\gamma}{2\beta}\right) < 0 \tag{3.29}
$$

which implies the power loss will also increase as electron beam is decelerated.

Figure 3.19 shows the power loss after collision for initial electron beam energy 10GeV case. It confirms that initial Beer-Can distribution electron beam needs smaller aperture than Gaussian distribution beam. As we revealed before, the real electron beam distribution should be in transition between Beer-Can to Gaussian distribution. We anticipate that the aperture value achieved from Beer-Can distribution is underestimated and the one from Gaussian is overestimated, the real aperture will reside between above two values. Besides, when one electron beam with certain top energy (10GeV) is decelerated to lower energy, it needs larger aperture to avoid beam loss.

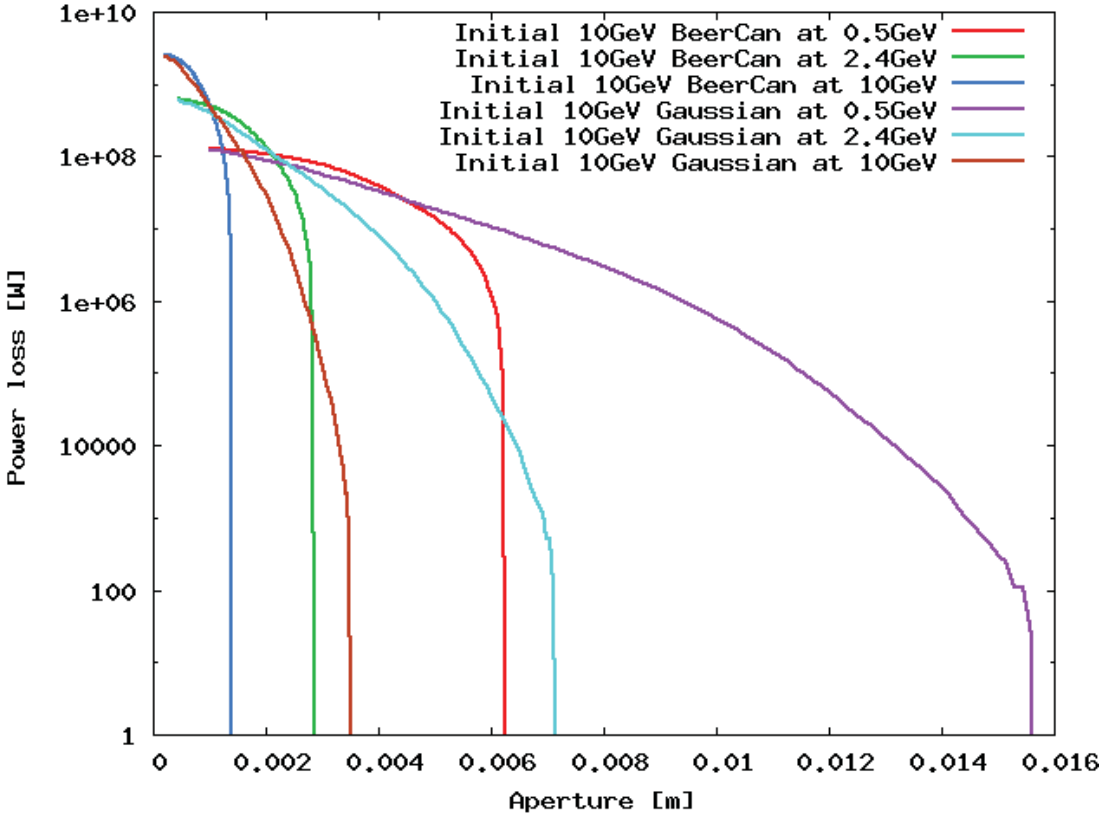

Figure 3.19: Power loss at given aperture and energy with initial Gaussian distribution and Beer-Can distribution, high energy setup.

Till now, all discussion is for the 10GeV case, which is high energy setup for the eRHIC project. The analysis for low energy (3GeV electron beam) follows same steps as high energy case. According to Table 1.2, the beam-beam parameters for both high energy and low energy are close. In order to avoid repetition, the procedure will be omitted, and power loss graph is given directly. Figure 3.20 indicates that the power loss for the low energy setup share similar features with the high energy case.

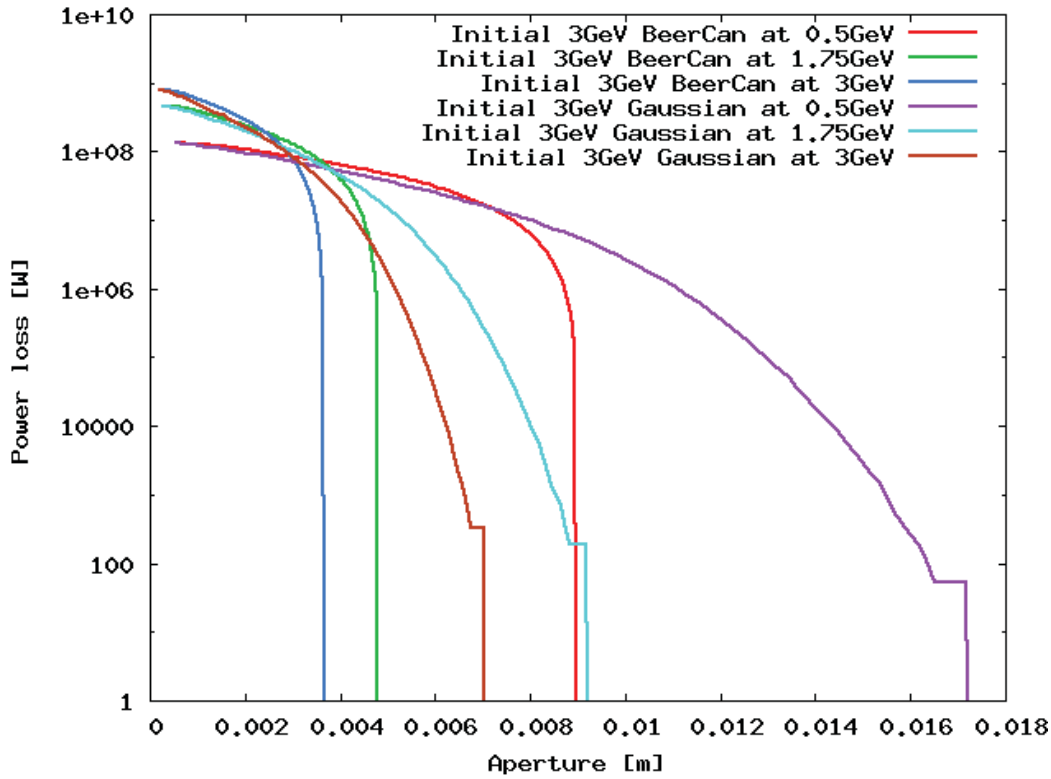

Figure 3.20: Power loss at given aperture and energy with initial Gaussian distribution and Beer-Can distribution, low energy setup.

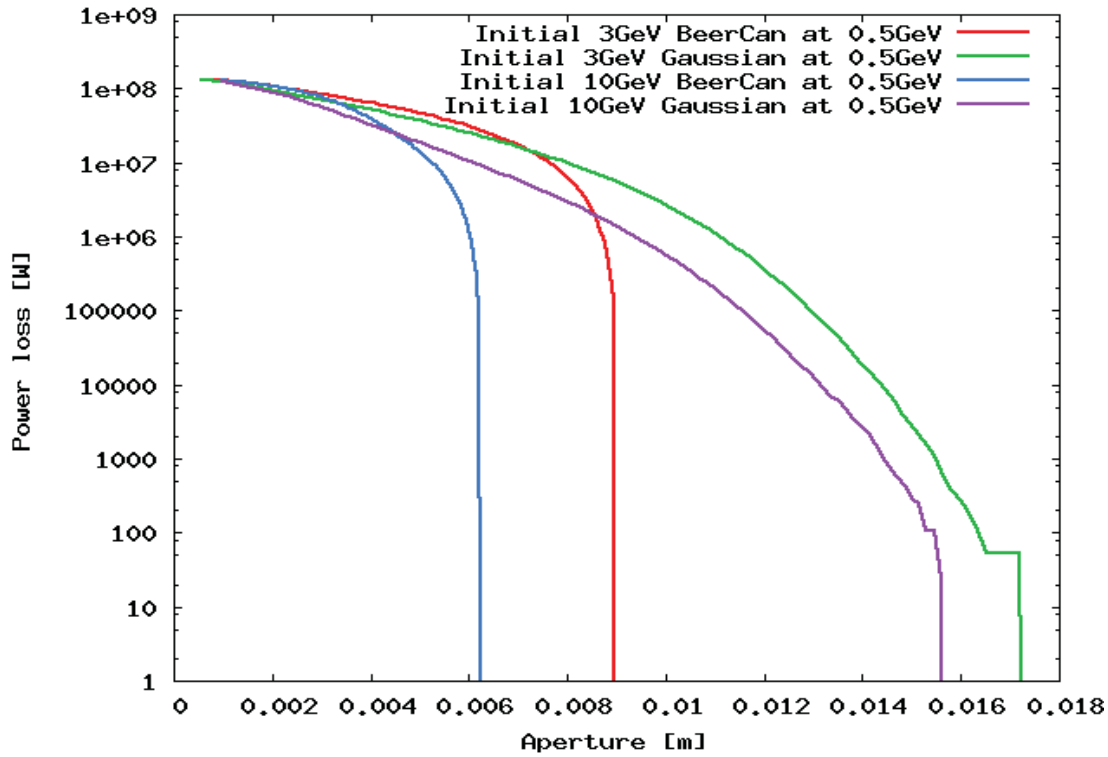

Figure 3.21: Comparison power loss at 0.5GeV, between different initial energy, 10GeV and 3GeV electron beam

From the comparison in Figure 3.21, the low energy case needs a larger aperture for same power loss level because the low energy beam is less rigid and the nonlinear force is more important. The difference in aperture between low and high energy is small. For both energy cases, the estimated apertures are around 15mm when the beam energy drops to 0.5GeV.

From the fact that final electron beam emittance after the collision is contributed from both nonlinear disruption and linear mismatch effect; one can manually compensate the mismatch to reduce the final emittance by changing the linear electron lattice. The difficulty for matching scheme lays at the capability of fast response system and the power needed for adjusting the magnet strength.

Nevertheless, we need to first investigate the advantage of the matching scheme. We assume the latter lattice for electron beam already matches with beta gamma function of electron beam distribution after collision according to (3.13). Then we can compare the aperture at 0.5GeV for certain power loss level for both the high energy and the low energy setup of eRHIC.

This is a dilemma to judge the advantage of matching scheme. Figure 3.22 illustrates that for both the high energy setup and the low energy setup, the matching scheme will decrease power loss only for the Beer-Can distribution. For a Gaussian beam, the matching scheme, on the contrary, will increase the power loss level, because of the tail of the electron distribution. The definite conclusion can be drawn is: if the electron distribution before collision does not have long tails as in Gaussian distribution, the matching scheme will reduce the required aperture by about 20%, for given power loss level. If this 20% aperture reduction is essential for magnet design of energy recovery pass, the matching scheme would be worth building.

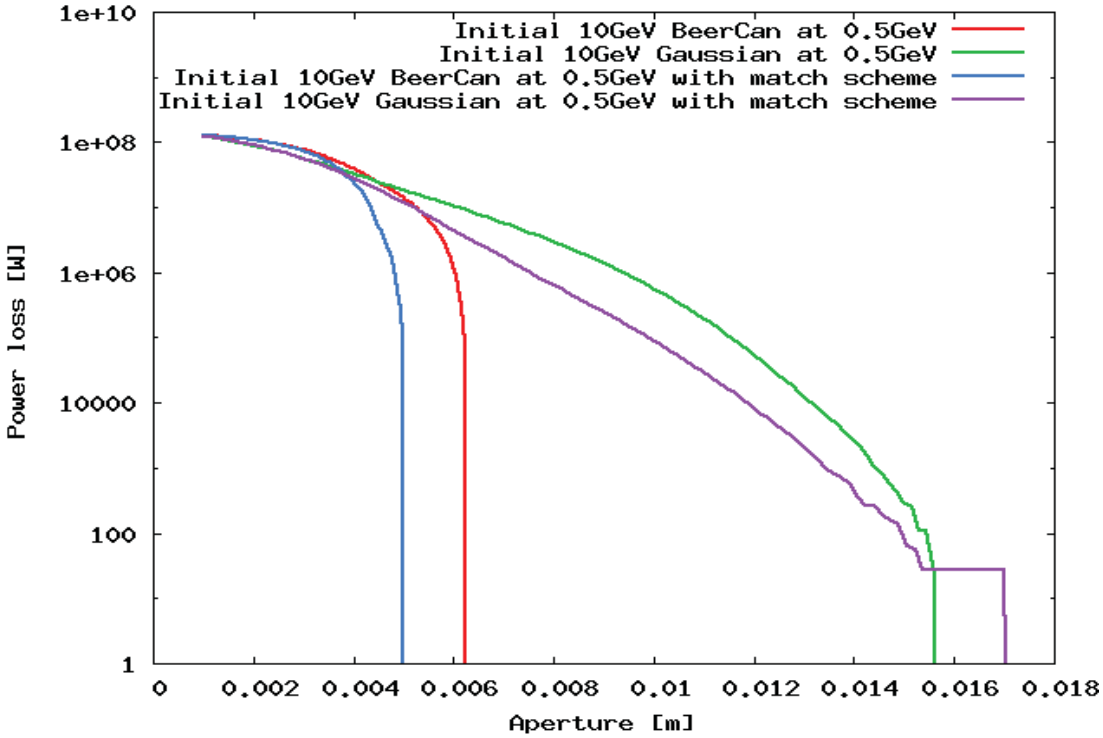

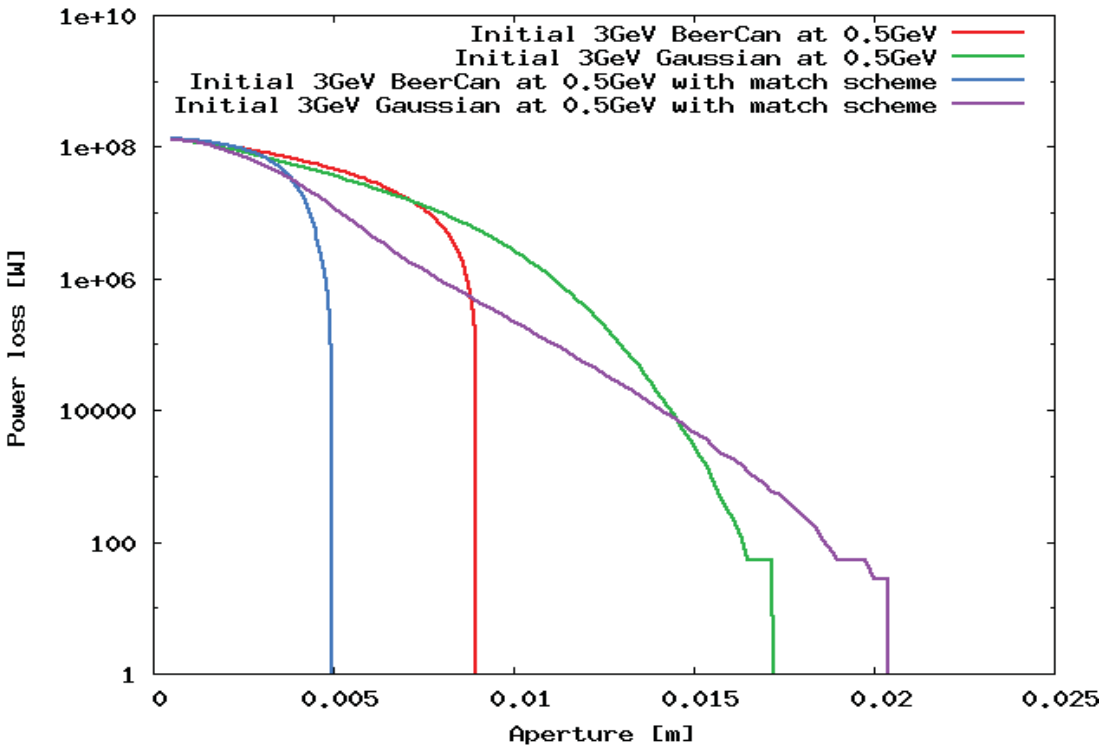

Figure 3.22: Power loss at 0.5GeV with or without matching scheme, top is initial 10GeV case and bottom is 3GeV case.

4. KINK INSTABILITY

Throughout the beam-beam collision, the proton beam experiences the field generated by the disrupted electron beam. The information of head in the proton bunch will be passed to its tail via this interaction. This scheme can lead to head-tail type instability, referred as 'kink instability'. Thus, beam stability conditions should be established to avoid proton beam loss.

4.1. Cause and Threshold

The periodic beam-beam interaction between proton and electron beams may excite strong head-tail type instability, referred as the kink instability, on the proton beam. Previous works [13, 14] analytically considered the instability using the linear approximation for the beam-beam force.

The physical scheme of the kink instability is that through the beam-beam effect, the imperfection of head part of proton beam will deform the electron beam, and the deformed electron beam will pass the imperfection of head part to the latter portion of proton beam. In the whole process, the electron beam generates a transverse wake field for proton beam through beam-beam interaction. The proton synchro-betatron motion under electron wake field may lead to instability if the wake field intensity

exceeds certain threshold.

Usually the imperfection of dipole moments has the lowest threshold and needs to be paid most attention. We can perform analytical treatment to search exact form of wake field induced by the electron beam. In this section, we use subscript p for the proton beam and subscript e for the electron beam. For the electron beam, only the beam center is of concern, so we only the include dipole motion of one longitudinal slice. And we use z to represent the longitudinal position inside proton, and s as the longitudinal coordinate. The derivatives are with respect to s. The proton macro-particle and center of the electron beam motion are given as:

$$\begin{aligned} x_p''(s,z) + K^2 x_p(s,z) &= -\delta(s - z/2)\frac{x_p(z,s) - \bar{x}_e(s)}{f_p} \\ \bar{x}_e''(s) &= -k^2(s)\left(\bar{x}_e(s) - \bar{x}_p(s,z)\right) \end{aligned} \tag{4.1}$$

Here, K represents the one turn betatron motion, $k(s)$ has the same form as in (3.2).

In order to make further analytical progress, we have to assume the function $k^2(s)$ is constant in range [-L/2, L/2], and zero outside the range, i.e. we have approximation as:

$$k^2(s) = \frac{1}{Lf_e} \tag{4.2}$$

Also we need to set the boundary condition that, before collision, the electron beam center has zero displacement and zero angular deviation, i.e.

$$\bar{x}_e(L/2) = \bar{x}_e'(L/2) = 0 \tag{4.3}$$

Then we take Laplace transformation to the second equation of (4.1) and can solve the

motion of electron beam centroid.

$$\bar{x}_e(s,z) = k\int_s^{L/2} \bar{x}_p(s',z)\sin k(s-s')\,ds' \tag{4.4}$$

Then the proton slice centroid at z satisfies the equation

$$\bar{x}_p''(s,z) + K^2\bar{x}_p(s,z) = -\frac{\delta\left(s-\frac{z}{2}\right)}{f_p}\left[\bar{x}_p(z,s) - k\int_s^{\frac{L}{2}} \bar{x}_p(s',z)\sin k(s-s')\,ds'\right] \tag{4.5}$$

Then we can learn that the wake field behaves as a sinusoidal function in range [-L/2, L/2] and the wake field only depends on the distance between leading and trailing particles, if we assume the proton distribution is uniform in longitudinal direction.

$$W(s,s') = W(s-s') = \sin k(s-s')H(s'-s) \tag{4.6}$$

If we don't make the approximation in (4.2), but instead use the Gaussian longitudinal model described by (3.2), there will be no analytical solution for electron beam centroid. However, it is easy to discover that the wake field does not only depend on the distance between two longitudinal coordinates but also on both coordinates explicitly. We can calculate the wake field by simulation from the definition of wake field:

$$W(s,s') = \frac{\gamma_p}{N_b r_{0p}}\frac{\Delta x'_{p,s}}{\Delta x_{p,s'}} \tag{4.7}$$

Here N_b is number of proton in the slice with initial offset Δx_p at s'. The kick for the proton beam at s ($s<s'$) could be achieved from simulation and so could the wake field.

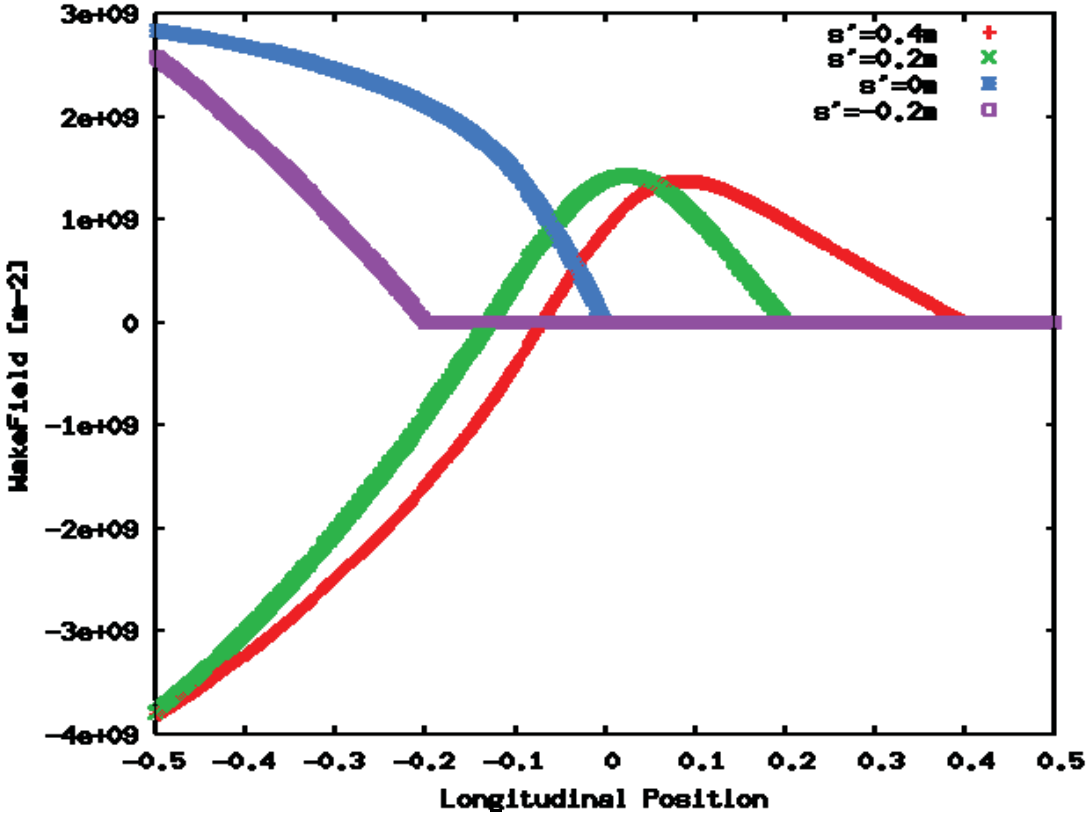

Figure 4.1: Wake field that the proton beam exerts, with different initial offset position of proton beam.

In Figure 4.1, we verify that the wake field shape depends on where the initial offset is and differs from sinusoidal function which comes out of the approximation in (4.2).

The exact threshold is impossible to calculate by an analytical approach under the wake field described by Figure 4.1. To get an estimation of threshold we need to carry out the following further simplification. First we assume the wake field is constant for a trailing particle and zero for a leading particle. Second a two-particle proton model is used so that we can use a matrix to describe the map. Subscripts 1 and 2 refer to two macro-particles respectively. Each particle carries $N_p/2$ charges. Particle 1 is leading particle in first half synchrotron period, and it becomes the trailing particle in the second half period. The one turn map for two particles is

simple to write:

$$M = \begin{pmatrix} \cos\phi + \alpha\sin\phi & \beta\sin\phi & 0 & 0 \\ -\gamma\sin\phi & \cos\phi - \alpha\sin\phi & 0 & 0 \\ 0 & 0 & \cos\phi + \alpha\sin(\phi) & \beta\sin\phi \\ 0 & 0 & -\gamma\sin\phi & \cos\phi - \alpha\sin\phi \end{pmatrix} \tag{4.8}$$

Here, the one tune phase advance φ includes the linear beam-beam tune shift, i.e. $\varphi = 2\pi(\nu + \xi)$. The betatron functions are at the position just after beam-beam interaction. Here the phase difference between two particles is neglected. The trailing particle feels wake field induced by electron beam, which can be express by the map:

$$K_1 = \begin{pmatrix} 1 & 0 & 0 & 0 \\ 0 & 1 & 0 & 0 \\ 0 & 0 & 1 & 0 \\ a & 0 & 0 & 1 \end{pmatrix} \tag{4.9}$$

We use a to represent the kink from wake field for trailing particle. Approximately a is given as:

$$a = \frac{\sigma_{pz}}{2 f_p f_z} = \frac{N_p N_e r_p r_e \sigma_{pz}}{2\sigma_{px}^2 \sigma_{ex}^2 \gamma_p \gamma_e} \tag{4.10}$$

In above equation, r is the classical radius of proton or electron, depending on the subscripts. After half synchrotron period, the previous leading particle 1 becomes the trailing particle. The K matrix becomes:

$$K_2 = \begin{pmatrix} 1 & 0 & 0 & 0 \\ 0 & 1 & a & 0 \\ 0 & 0 & 1 & 0 \\ 0 & 0 & 0 & 1 \end{pmatrix} \tag{4.11}$$

The one turn matrixes including beam-beam wake field in each half synchrotron period (T_1 and T_2) are:

$$T_1 = K_1 \cdot M; \qquad T_2 = K_2 \cdot M \tag{4.12}$$

If the synchrotron tune of the storage ring is ν_s, it takes N_s=1/ν_s turns to accomplish one synchrotron oscillation. The total matrix in one synchrotron period gives:

$$T = T_2^{N_s/2} \cdot T_1^{N_s/2} \tag{4.13}$$

Usually, the explicit matrix of T is hard to obtain. But if both T_1 and T_2 are not degenerate, which means that nth order matrix has n distinguished eigenvalues; we can get matrix power of T_1 and T_2 easily from its Jordan form. For any matrix T_1 and T_2, they can be treated by Jordan Decomposition and written as Jordan canonical form. Then equation (4.13) will be simplified as:

$$\begin{aligned} &T_1 = S_1 J_1 S_1^{-1} \qquad\qquad T_2 = S_2 J_2 S_2^{-1} \\ &T = S_2 J_2^{N_s/2} S_2^{-1} S_1 J_1^{N_s/2} S_1^{-1} \end{aligned} \tag{4.14}$$

If T_1 and T_2 are not degenerate, J_1 and J_2 will be diagonal matrixes and the power of matrices becomes the power of each diagonal elements. Then the total matrix T will be just multiplication of six matrixes.

With no surprise, we will get matrix T in a complicated form. As we know the synchrotron oscillation will be very slow, so N_s is much larger than 1. We can greatly simplified T, if the following conditions hold:

$$N_s \gg 1 \quad \text{and} \quad N_s \gg |\cot\phi| \tag{4.15}$$

The second condition holds because the tune of ring must avoid integer and half integer to avoid resonance from imperfection of dipole and quadrupole magnets. Then the term $\cot\varphi$ won't be a large number. If taking the eRHIC parameters for instance, $N_s = 1/\nu_s = 232$, we have the transverse tune must be away from integer or half integer by value at least 6.8×10^{-4}. Apparently this condition is always true. The simplified T reads as:

$$
\begin{aligned}
T &= \begin{pmatrix} 1-\left(\frac{aN_s\beta}{4}\right)^2 M\left(N_s\phi\right) & \frac{aN_s\beta}{4} X\left(N_s\phi\right) \\ \frac{aN_s\beta}{4} X\left(N_s\phi\right) & M\left(N_s\phi\right) \end{pmatrix} \\
M\left(\phi\right) &= \begin{pmatrix} \cos\phi + \alpha\sin\phi & \beta\sin\phi \\ -\gamma\sin\phi & \cos\phi - \alpha\sin\phi \end{pmatrix} \\
X\left(\phi\right) &= \begin{pmatrix} -\alpha\cos\phi + \sin\phi & -\beta\cos\phi \\ \gamma\cos\phi & \alpha\cos\phi + \sin\phi \end{pmatrix}
\end{aligned}
\tag{4.16}
$$

Then the criteria of stable motion described by T are that no absolute values of eigenvalue exceed one and no eigenvalues are one. After mathematical steps, we have:

$$
\frac{aN_s\beta}{4} < 2 \quad \Rightarrow \quad a < \frac{8\nu_s}{\beta} \tag{4.17}
$$

After plugging in parameters of eRHIC, where proton beta function is 0.26m, and the synchrotron tune is 0.0043, we have the parameter a must less than 0.13. From the definition of parameter a in (4.10), the parameter a has value 2.1. In other words, if other eRHIC parameters remain as in Table 1.2, the estimated threshold of proton intensity given by the approximation in this section is about 1.2×10^{10} per bunch, while design number is 2.0×10^{11} per bunch. The design parameter is about 16 times larger than the calculated threshold.

4.2. Kink Instability from Simulation Results

The analytical approach in 4.1 cannot give a full picture on the Kink Instability. We need to use simulation code to investigate the threshold and instability modes when the system becomes unstable[12]. Two main factors that are missed in analytical study will be covered by simulation.

First, the beam-beam force is nonlinear beyond one transverse rms size for both beams. The wake field at large transverse amplitude is smaller or even of a different sign if compared with adaxial case. Second, because longitudinal distribution of proton beam is a Gaussian beam, the actual transverse wake field in Figure 4.1 cannot be expressed in analytical formula. Different wake field shapes will certainly affect instability threshold.

In order to separate from the other effects, the electron rms size is assume to be not deteriorated by the proton beam, i.e. we only simulated dipole effects on both beams. In simulation we only use one macro-particle for the electron beam. The size of electron beam is properly calculated at different position according to hourglass effect. By these settings we ignore the electron pinch effect.

We use 10^5 proton macro-particles in simulation. The calculation time is set to 10000 turns, which is 0.13 seconds. Usually it is long enough when the transverse instability is investigated. In order to prevent additional tune spread, we set the chromaticity to zero in this section.

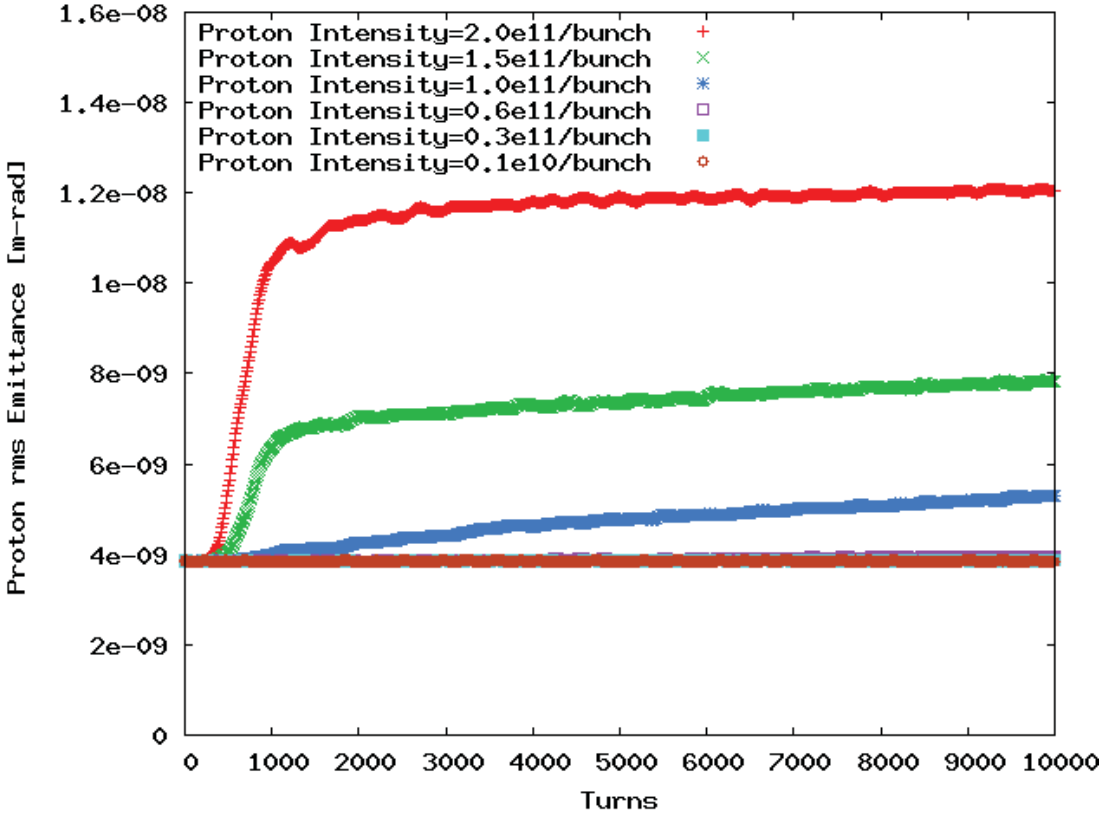

Figure 4.2: The proton rms emittance growth with different proton beam intensity.

Figure 4.2 shows the proton rms emittance growth under nonlinear beam-beam force with zero chromaticity under different proton beam intensity. Here the electron and proton parameters are according to Table 1.2 except proton beam intensity. The nominal proton beam intensity is 2.0×10^{11} per bunch, which gives largest and fastest rms emittance growth. The growth rate decreases as the proton intensity drops down. At very low intensity ($<3.0\times10^{10}$ protons per bunch), no emittance growth is observed with in calculation time. After rising quickly, the emittance growth in the unstable high intensity cases is suppressed by nonlinear force.

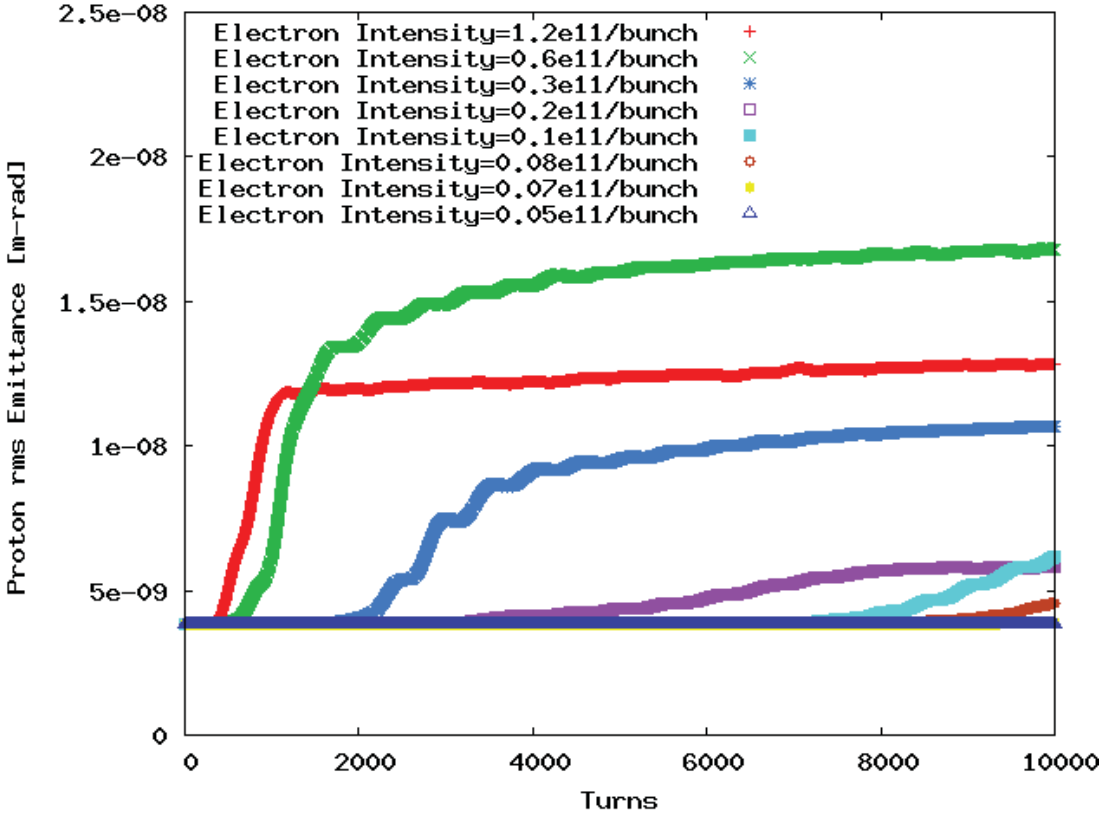

Figure 4.3: The proton rms emittance growth with different electron beam intensity.

Figure 4.3 shows the proton rms emittance growth under nonlinear beam-beam force with zero chromaticity for different electron intensities. Other parameters are set to the same value as parameter table of Table 1.2. For a very low electron beam intensity (0.7×10^{10} electrons per bunch), no emittance blowup happens within calculation time. From the graph, we can see the higher electron beam intensity we use, the faster rise time we get. However, large electron intensities generate larger nonlinear beam-beam field, which suppress the proton beam emittance to a lower level. This explains the difference between Figure 4.3 and Figure 4.2.

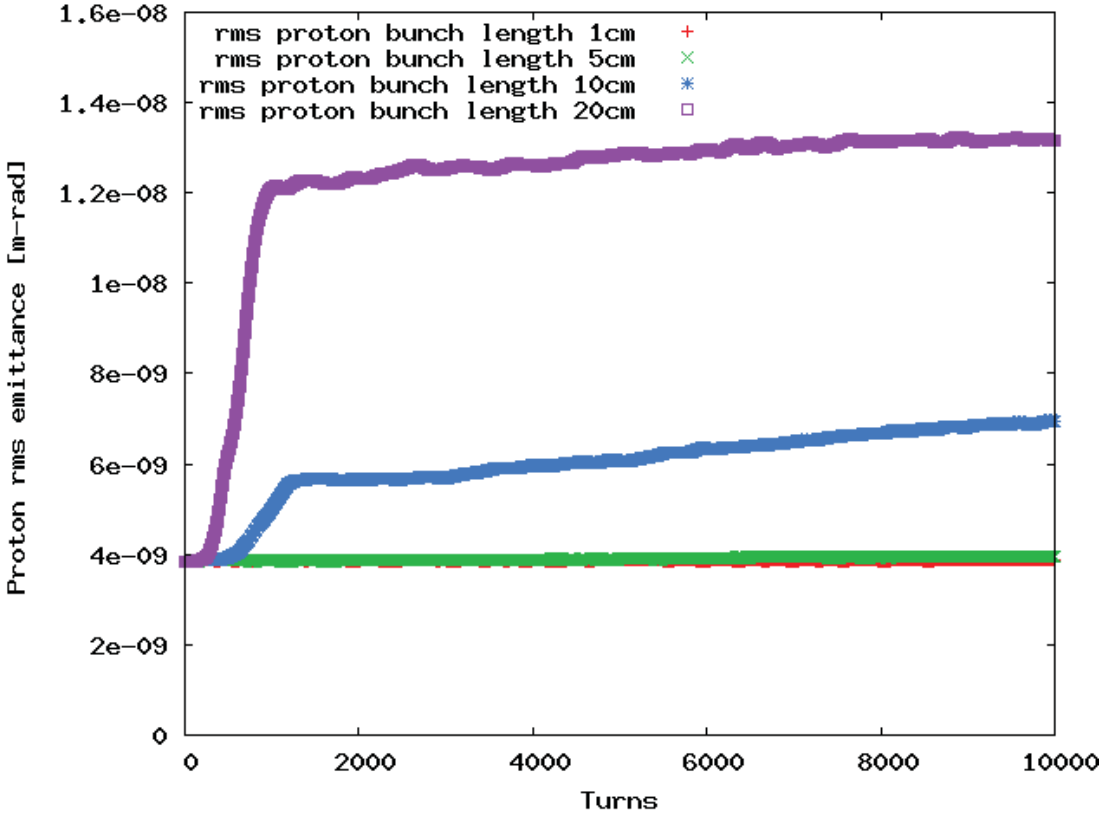

Figure 4.4: The proton rms emittance growth with different proton rms bunch length.

From the simple model of analytical approach in section 2.1, the threshold of transverse strong head-tail instability gives:

$$a = \frac{N_p N_e r_p r_e \sigma_{pz}}{2\sigma_{px}^2 \sigma_{ex}^2 \gamma_p \gamma_e} < \frac{8\nu_s}{\beta} \tag{4.18}$$

For nominal design number σ_{pz}=0.2m, there is clearly fast instability with design value of other parameters. We are anticipating that there will be a threshold for small rms bunch length σ_{pz}, as we already shown for electron and proton density. From Figure 4.4, the fast emittance growth disappears when the bunch length is shorter than 5cm.

In order to compare this fairly to the threshold from matrix approach in previous section, we turn off the nonlinear effect and hourglass effect in the simulation code.

In addition, the synchrotron motion is replaced by matrix (2.23). By this setting we only consider linearized beam-beam force and exclude the coupling between synchrotron and betatron motions due to hourglass effect.

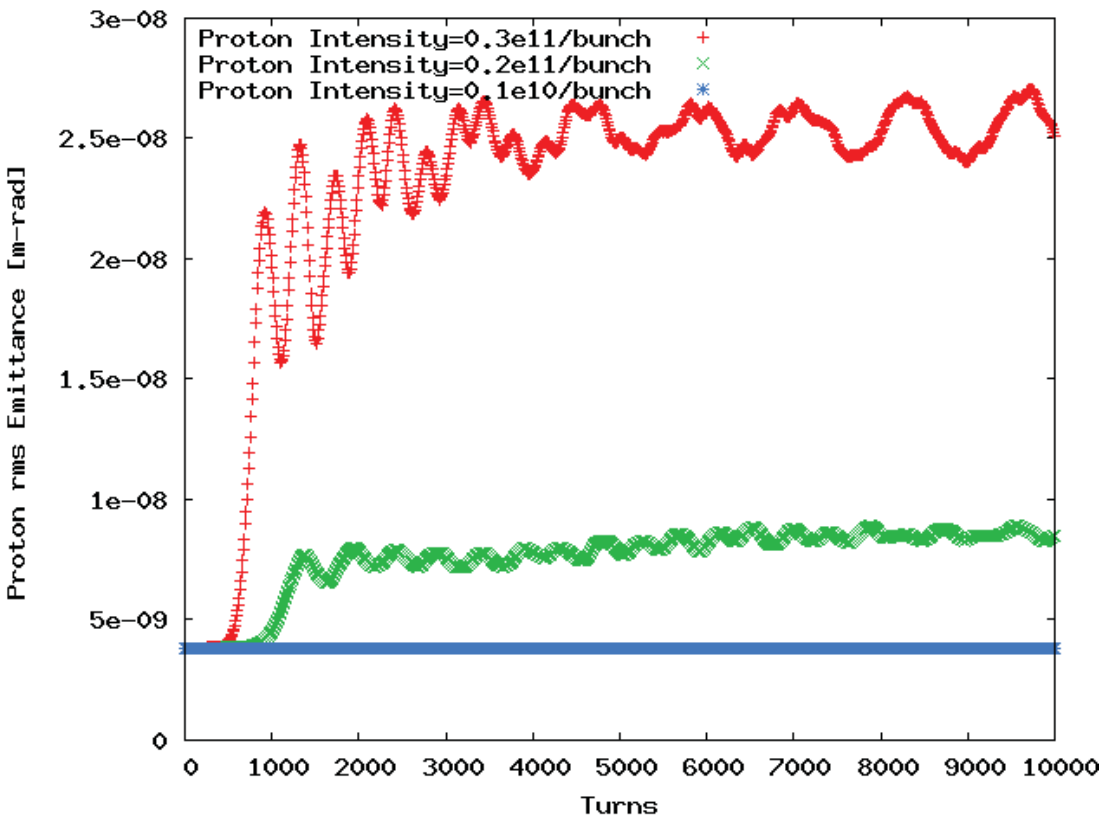

Figure 4.5: The proton rms emittance growth with different proton beam intensity with linearized beam-beam force and without hourglass effect.

If we compare Figure 4.2 with Figure 4.5, in some proton intensity case such as 0.3×10^{11} / bunch, the proton beam loses its stability in linearized beam-beam force and absence of hourglass effect case. The tune spread caused by nonlinearity and hourglass effect actually increases the threshold of system. In Figure 4.5, apparently, the threshold for proton intensity is between 0.1×10^{11} / bunch and 0.2×10^{11} / bunch.

To investigate the threshold more accurately, we can perform Fast Fourier Transform on turn-by-turn proton beam centroid position. For each proton intensity, the main peak and side peaks corresponds to the betatron tune and synchrotron side

bands because beam-beam force provides coupling between transverse and longitudinal motion. Here we take horizontal motion for instance.

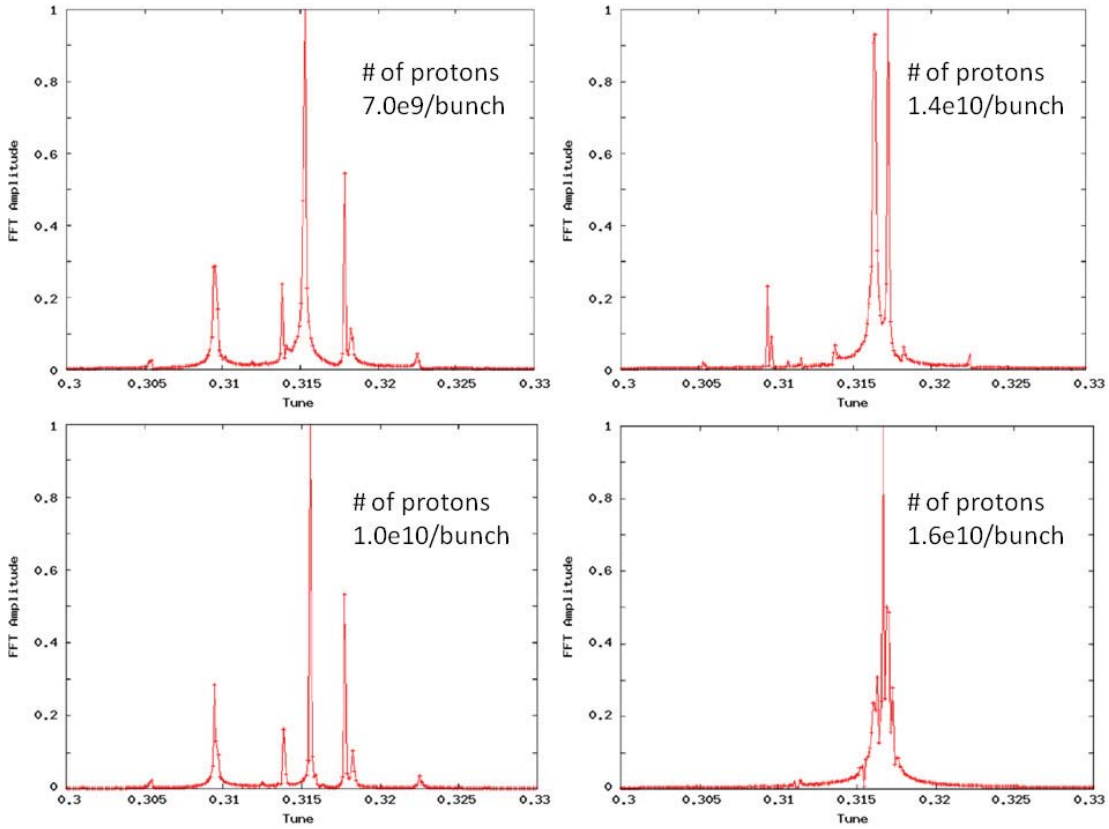

Figure 4.6: FFT of proton beam horizontal centroid with different proton intensities.

In this simulation the horizontal and longitudinal tune is chosen to be 0.685 and 0.0043 respectively. If proton intensity approaches zero, the main peak and side bands should be at:

$$\nu = \nu_\beta \pm n\nu_s \qquad n \in \mathbb{Z} \tag{4.19}$$

where n is the order of side bands, ν_β is the horizontal tune and ν_s is longitudinal tune. As proton intensity increases, some side bands move towards the main peak (zero order). When two peaks merge, the beam will become unstable.

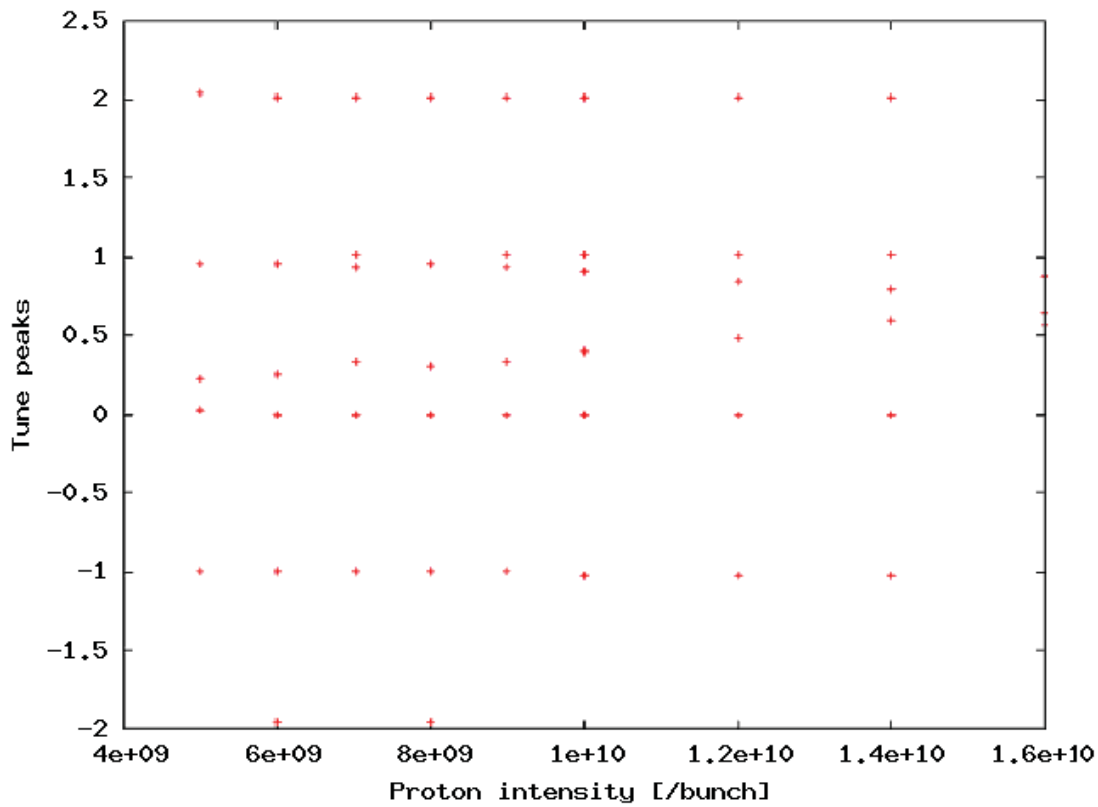

Figure 4.7: Proton beam centroid FFT peak as function of proton intensity. The tune peaks have been normalized by $(\nu-\nu_\beta)/\nu_s$.

From Figure 4.7, the first order side band merges with main peak at an intensity of 1.6×10^{10} proton per bunch. This means the threshold of proton intensity is 1.6×10^{10} /bunch, which is very near to the analytical anticipation 1.2×10^{10} /bunch.

When the beam in unstable, the mode can be investigated by taking a snapshot of the proton beam at IP. On the turns when fast emittance growth is seen, the 0 and 1 collective modes are well seen in the dipole moment pattern, as shown in Figure 4.8.

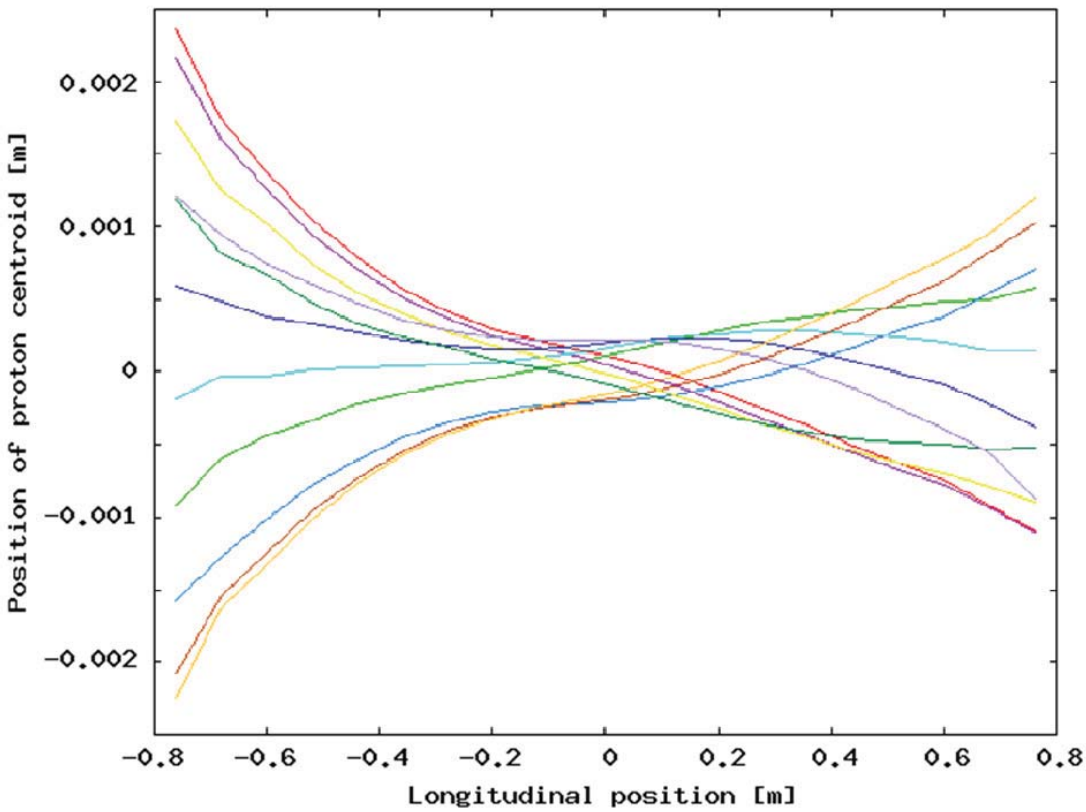

Figure 4.8: Snapshot of proton centroid position.

4.3. Beam Stabilization and Slow Emittance Growth

Since the eRHIC proposed proton intensity is above threshold, proper scheme is needed to cure the instability. As we know, instabilities can be suppressed by tune spread, which is usually referred as Landau damping. There are many sources to provide tune spread. Nonlinear beam-beam force, hourglass effect and synchro-betatron motion are contributing to tune spread automatically. Clearly, the tune spread helps in stabilizing the proton beam beyond threshold according to last section. But at nominal design parameter, the beam is still suffering from instability.

To increase tune spread, the easiest way is apply chromaticity in simulation, because the transverse tune for one particle is:

$$\nu_{x/y} = \nu_{\beta,x/y} + \xi_{x/y}\delta \tag{4.20}$$

So the rms tune spread of the beam is just the rms energy spread times chromaticity. Experimentally, the tune spread can also be enhanced by nonlinear magnets such as octopoles.

From the eRHIC RF cavity data in Table 2.1, the rms energy spread for proton beam is 5×10^{-4}. We can apply different chromaticity to achieve various rms tune spread values.

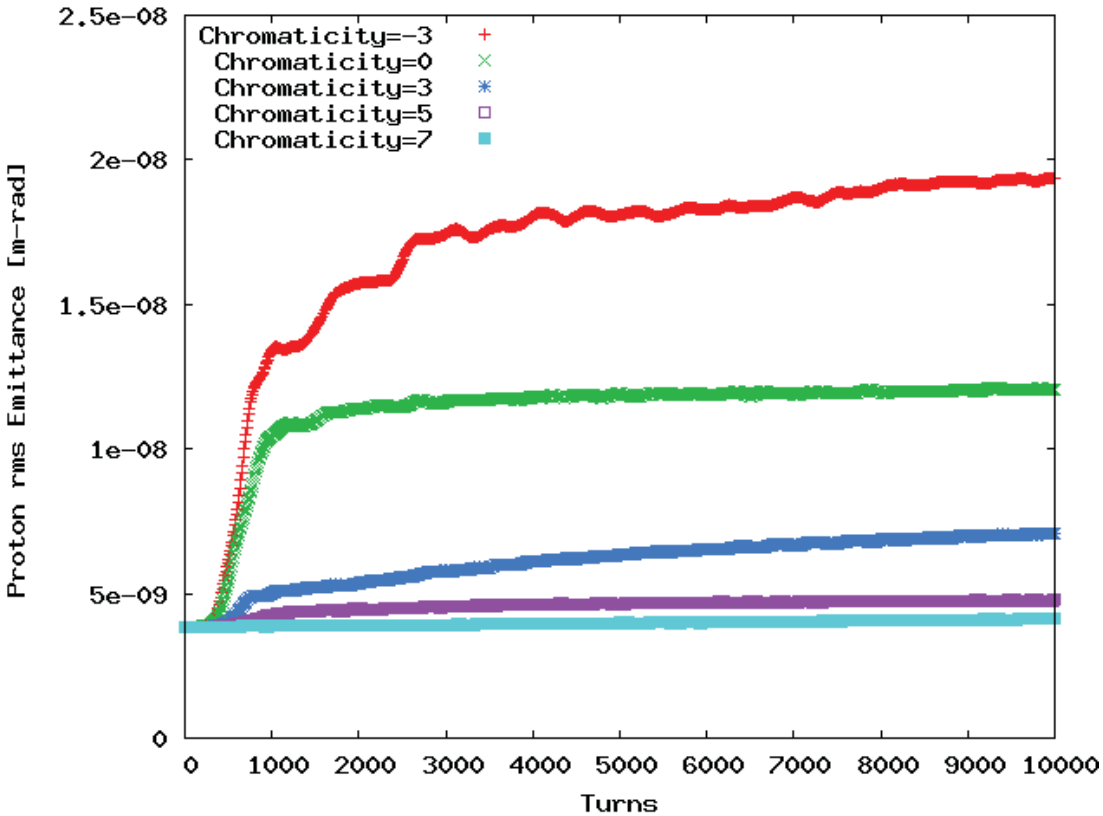

Figure 4.9: Proton rms emittance growth under different chromaticity.

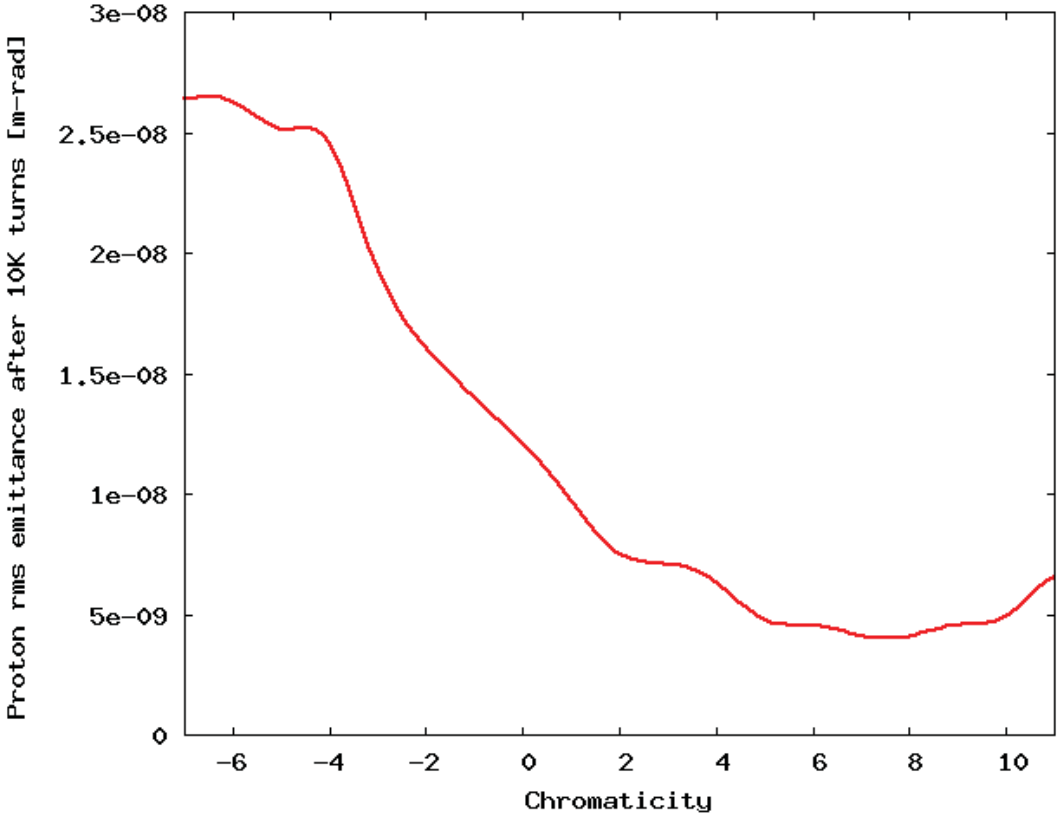

Figure 4.10: Proton emittance growth with different chromaticity

Figure 4.9 and Figure 4.10 indicates chromaticity value of 7-8, which provides rms tune spread 3.5-4.0×10^{-3}, can suppress the instability with other parameters in their design values. The chromaticity must be of the correct sign and have small amplitude; otherwise it will deteriorate the beam due to head-tail effect. Under transition energy, the chromaticity must be small negative number and above transition a small positive chromaticity is need. We can see a wrong sign chromaticity will deteriorate the beam worse, even though it can also provide same amount of tune spread.

With low proton intensity, half of the design value 1×10^{11} per bunch, slightly smaller chromaticity is needed, as shown in Figure 4.11. Here, a chromaticity value 6 is sufficient to suppress the emittance growth.

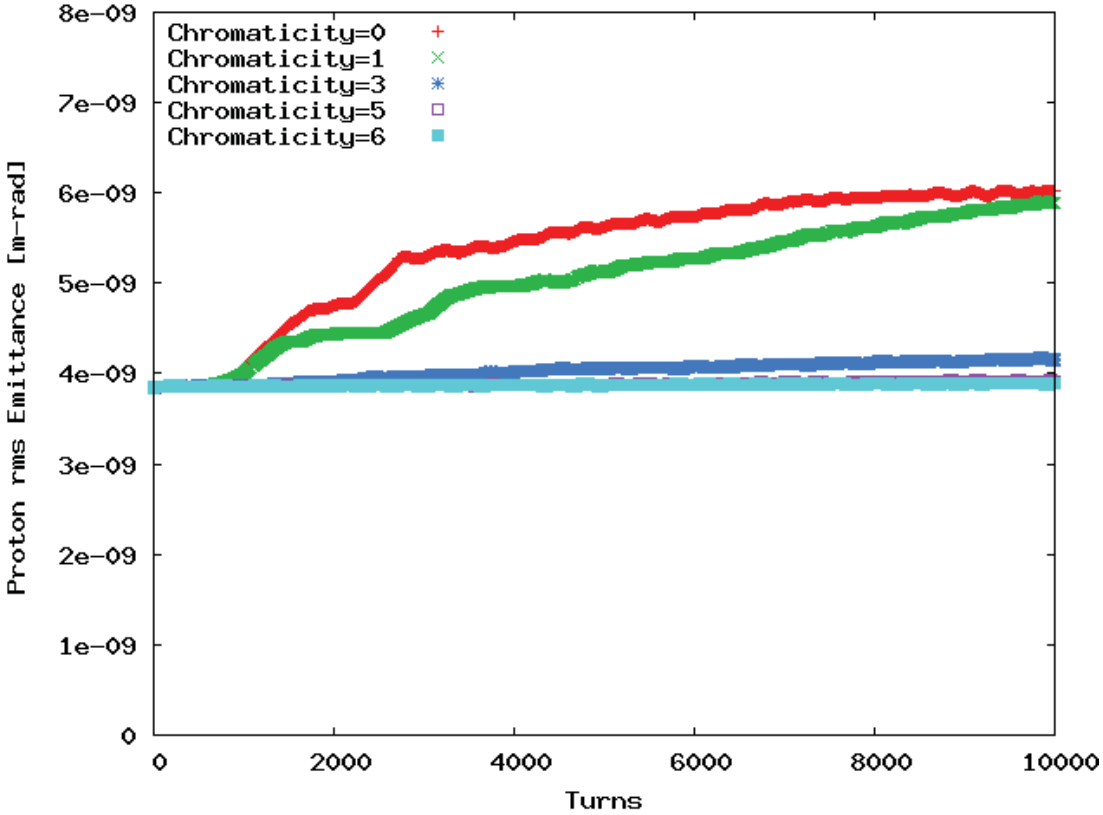

Figure 4.11: Proton rms emittance growth under different chromaticity with low proton intensity (1×10^{11} per bunch)

One may already notice that even the fast emittance oscillation is suppressed by proper chromaticity; there will be small proton emittance growth under this chromaticity. A zoom-in figure of Figure 4.9 can show it clearly (Figure 4.12).

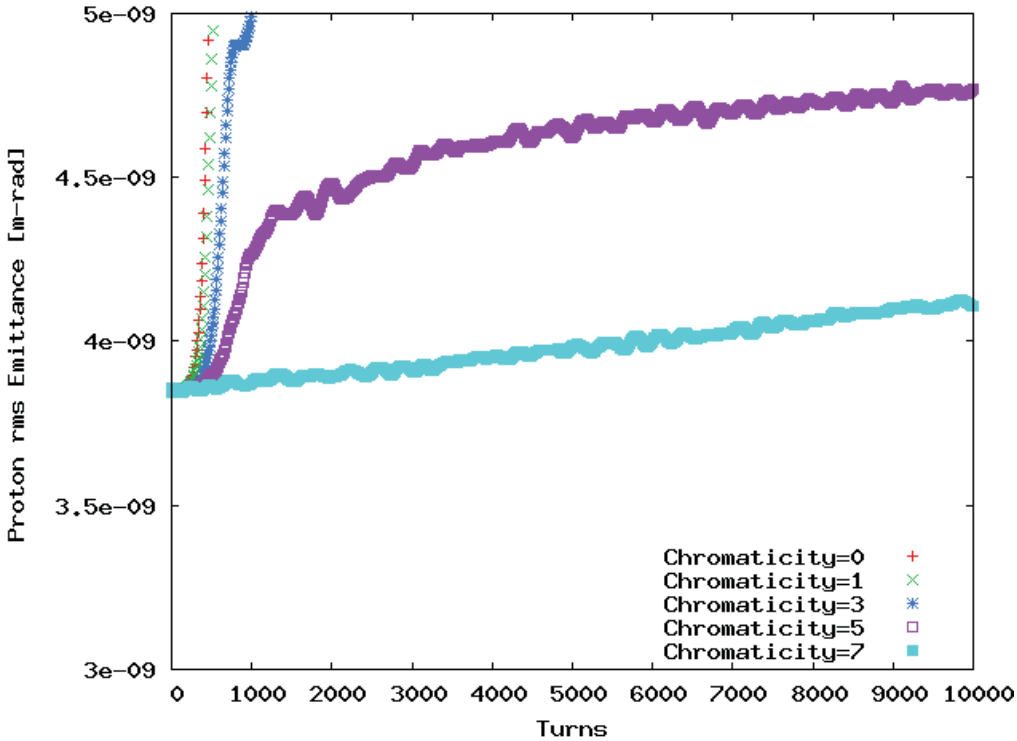

Figure 4.12 : Slow proton emittance growth at when chromaticity equals 7.

We must seek the origin of this slow emittance growth, because the emittance increases by 7.5% in only 0.13 seconds, which yields a very poor lifetime. This slow emittance growth is also reported from other head-tail type instability code [15]. This emittance growth is believed to be, at least partly, contributed by numerical error, i.e. a fake phenomena generated only by the code. We can examine this by increasing the number of macro-particles used in the code and fit the emittance growth with linear function. If the emittance growth is caused by numerical error, the slope of rms emittance growth should decrease as number of proton macro-particle number increases.

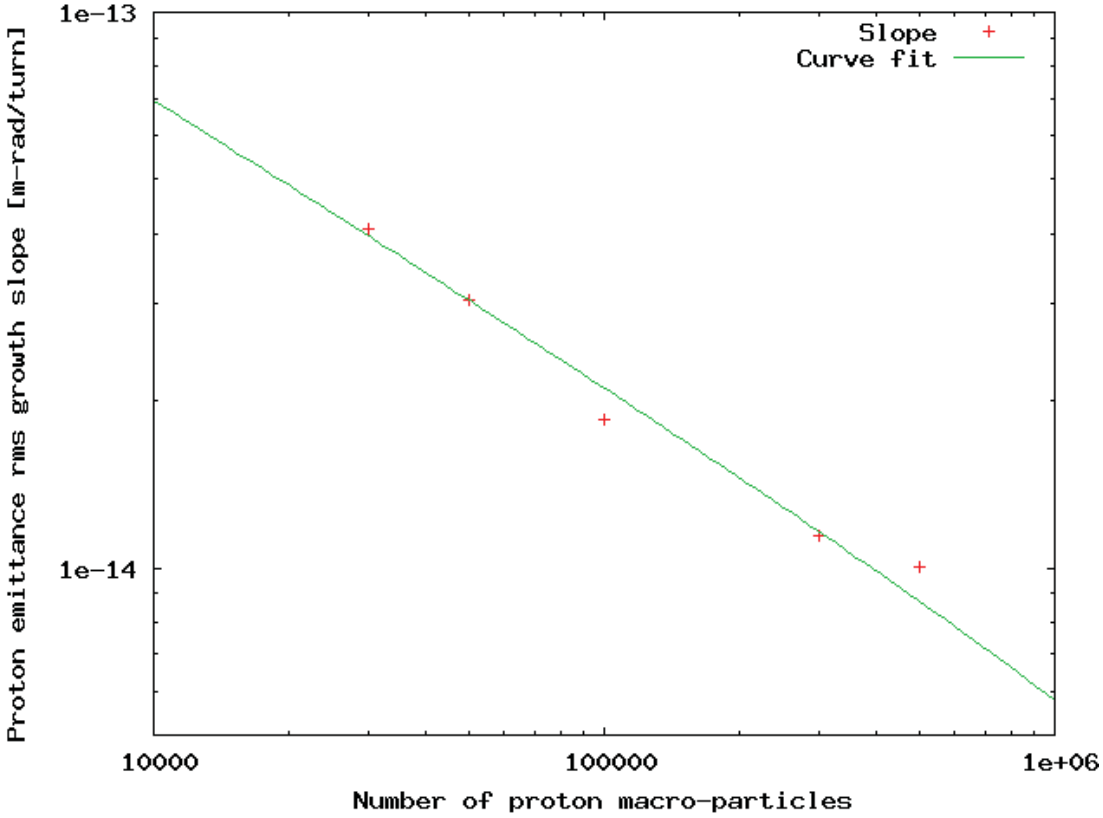

Figure 4.13: Proton rms emittance growth slope as function of macro-particle number

As indicated in Figure 4.13, the emittance growth slope drops if more macro-particles are used in simulation. We can model the emittance slope K be function of macro-particle number as:

$$K = a + \frac{b}{\sqrt{N}} \tag{4.21}$$

Here, N is the number of macro-particles, a and b are parameters to be determined. a is the intrinsic emittance growth slope and b is related to the slope due to numerical error. The fitting result is:

$$\begin{aligned} a &= -1.28\times10^{-15} \pm 2.03\times10^{-15}\,\text{m-rad/turn} \\ b &= 7.07\times10^{-12} \pm 5.48\times10^{-13}\,\text{m-rad/turn} \end{aligned} \tag{4.22}$$

Although the result cannot give a definitive judgment that the slow proton rms emittance growth at presence of proper chromaticity totally comes from numerical noise, we have strong evidence that the actual emittance growth is much smaller than the slope shown in Figure 4.12. More accurate estimation needs stronger computation resource.

5. PINCH EFFECT

The electron beam pinch effect is a very important effect in eRHIC e-p collision; because the enormous beam-beam parameter of electron beam will deform the electron distribution and shrink the rms beam size during collision. The consequence of this on the electron beam such as possible beam loss was covered in Chapter 3. In this chapter we are focused proton beam dynamics under electron beam pinch effect.

5.1. Collision of Thin Proton Beam with Rigid Electron Beam

Before considering the pinch effect of electron beam, we need to investigate the proton beam dynamics if the proton beam collides with 'strong' electron beams every turn. 'Strong' means any beam-beam effects on electron beam are neglected. In reality, this model is good for the fact that electron beam energy is extremely high or there is strong longitudinal magnetic field that make electron beam rigid. However, in ERL based eRHIC case, electron beam is 'weak' compared with proton beam and a solenoid for such strong longitudinal magnetic field is impossible to make. But the study of collision with rigid electron beam is still valuable for two reasons.

First, we can separate the hourglass effect, kink instability and pinch effect from nonlinear beam-beam force. As we know, under nonlinear force, beam emittance will not be a constant. Furthermore, combine with synchrotron motion, the collision point for different proton with different synchrotron amplitude will oscillate because of synchrotron oscillation and beam-beam parameter will also change due to hourglass effect. Only simulation can assure proton emittance will not blow up under nonlinear force and synchro-betatron oscillation.

Second, as we revealed in chapter 1, the proton beam will encounter the electron beam with a complicated transverse distribution. We anticipated that the real electron transverse distribution before the collision should be in some stage of transition from a Beer-Can distribution to a Gaussian distribution. For the Beer-Can distribution with transverse rms beam size σ, the beam density inside 2σ is constant and zero outside the boundary. The beam-beam field calculated from Beer-Can distribution, as showed in Figure 5.1, is linear function as transverse coordinate with in 2σ boundary and decreases inversely proportional to transverse coordinate.

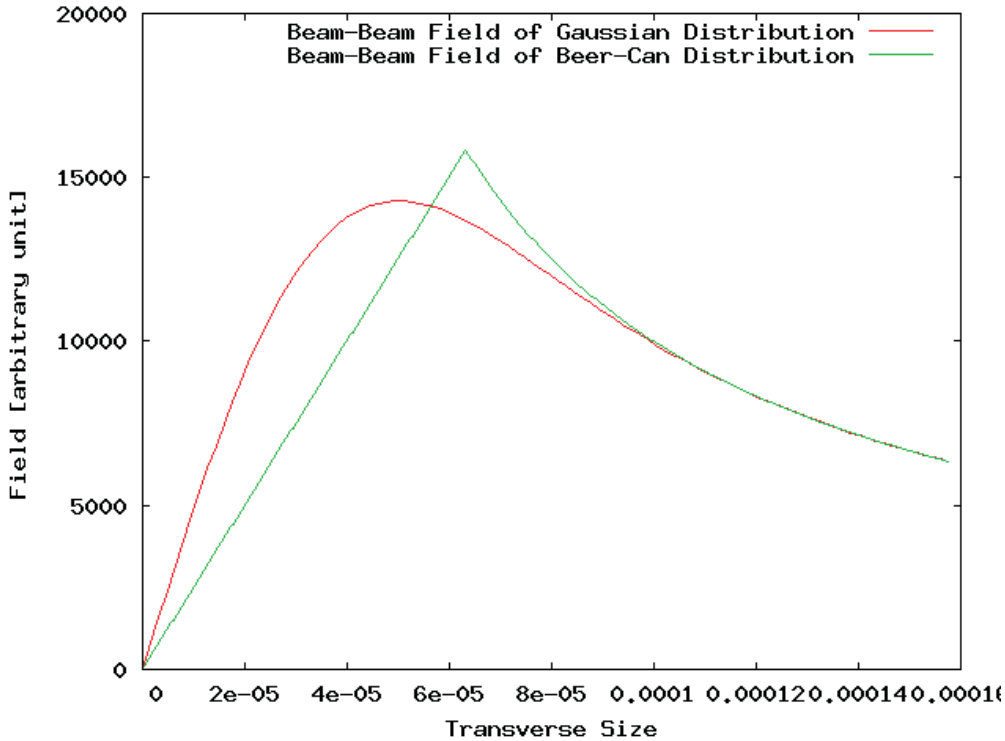

Figure 5.1: The beam-beam field of Gaussian and Beer-Can distribution with same beam intensity.

There is a hidden problem for the Beer-Can distribution in that, although the beam-beam field is a continuous function, its first order derivative has discontinuity at r=2σ. It means the proton beam at 2σ will have sudden change in beam-beam tune shift. The effect of this discontinuity on the proton beam also needs to be confirmed by simulation.

In the following simulation, we ignore the proton bunch length so that only the nonlinearity of beam-beam force is included. The working point is chosen to be (0.672, 0.678), similar to the current RHIC working point. From Figure 5.2, we can clearly see that, due to the field first order derivative discontinuity of Beer-Can distribution, the proton beam transverse rms emittance grows remarkably in 1×10^6 turns computation time. For comparison, proton emittance doesn't have observable increase during the computation time for transverse Gaussian distribution electron beam. Here, the lifetime is only estimation; since numerical error mechanism also

introduces emittance growth.

Table 5.1: Lifetime of Proton beam with different electron beam distribution

Electron beam transverse distribution	Time of proton emittance double
Beer-Can	87 seconds
Gaussian	>200 hours

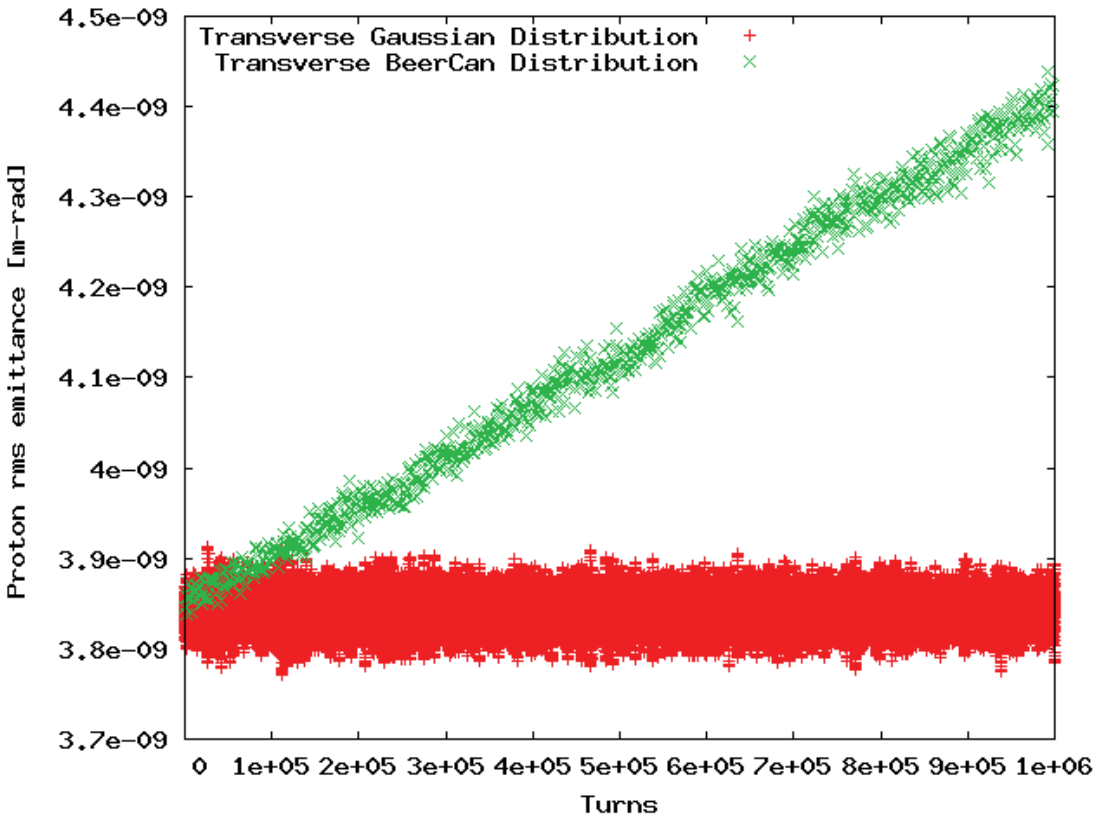

Figure 5.2: Comparison of proton rms emittance with rigid Gaussian and Beer-Can electron transverse distribution

Do the result in Figure 5.2 and Table 5.1 imply that transverse Beer-Can distribution electron beam must be forbidden? This question may actually be moot. The Beer-Can distribution we just considered has a sharp edge at two transverse rms beam size. But the sharp edge is not realistic in two following reason. First, there is no absolute hard edge beam in reality even at the moment that electron beam just comes out of the cathode. The edge must smoothly transfer from certain finite value to zero. Second, when electron beam is accelerated in the Linac and transported

through 5 pass lattices, the transverse electron beam distribution smoothen further because of the synchrotron radiation and the magnet alignment errors.

Therefore, it is worthwhile to model a 'soft edge Beer-Can distribution' to describe electron beam transverse distribution before collision. By utilizing the model, there will be no tune shift discontinuity for proton beam at transverse edge of electron beam. The model is written in the electron beam transverse density:

$$\rho(r) = \frac{N_e}{8\pi\sigma_{ex}^2}\,\mathrm{erfc}\left(\frac{r-2\sigma_{ex}}{edge}\right) \tag{5.1}$$

Here we use complementary error function erfc() to model the soft edge. When the edge approaches zero, $\rho(r)$ represents the Bear-Can distribution with hard edge (as shown in Figure 5.3).

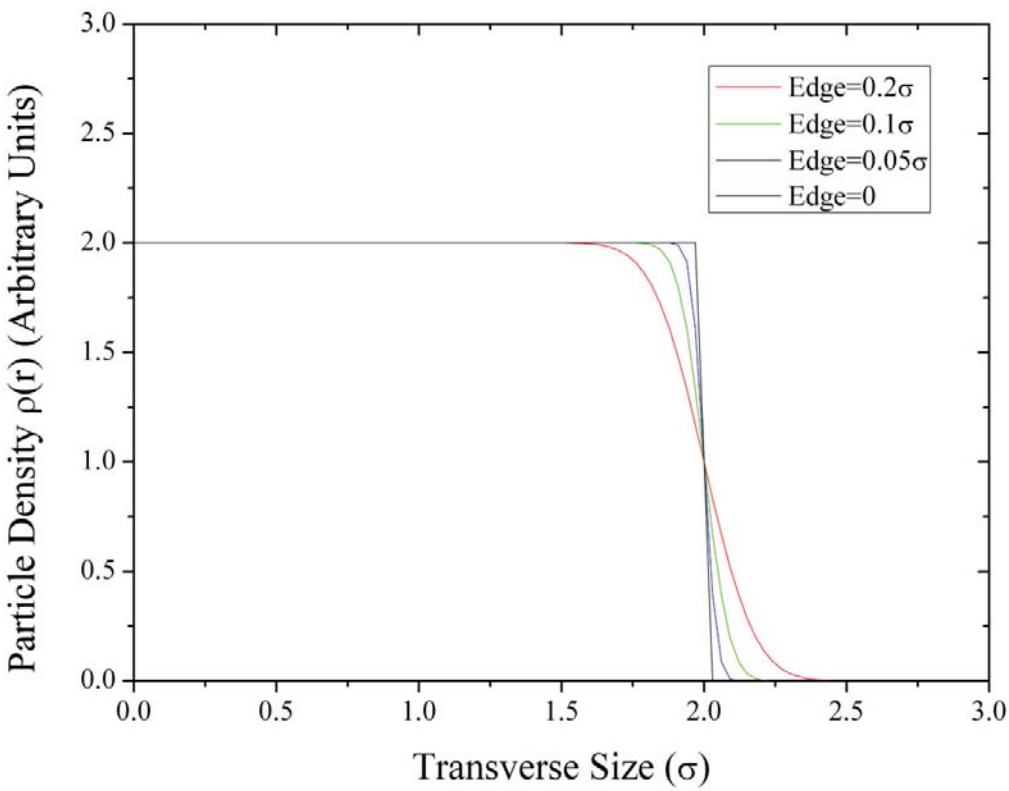

Figure 5.3: Soft edge Beer-Can distribution with different edge

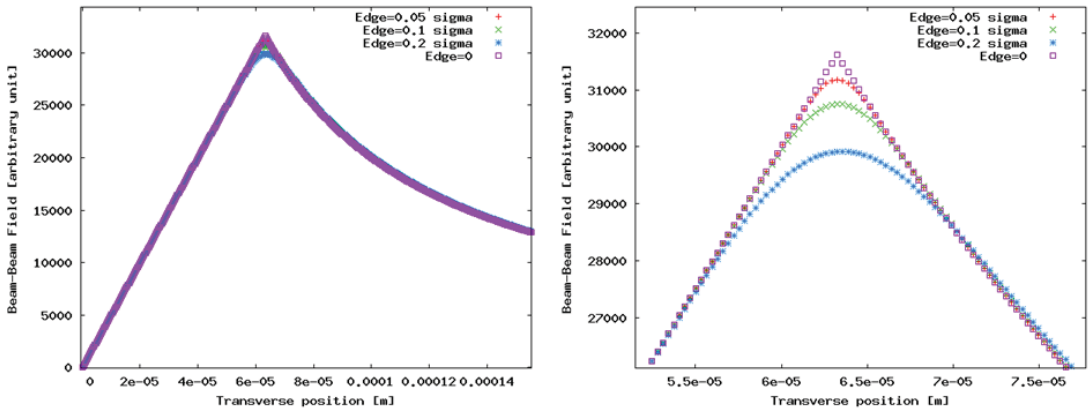

Figure 5.4: Beam-Beam Field calculated from Beer-Can transverse distribution with different edge size. The right graph is the zoom-in graph of left one at edge.

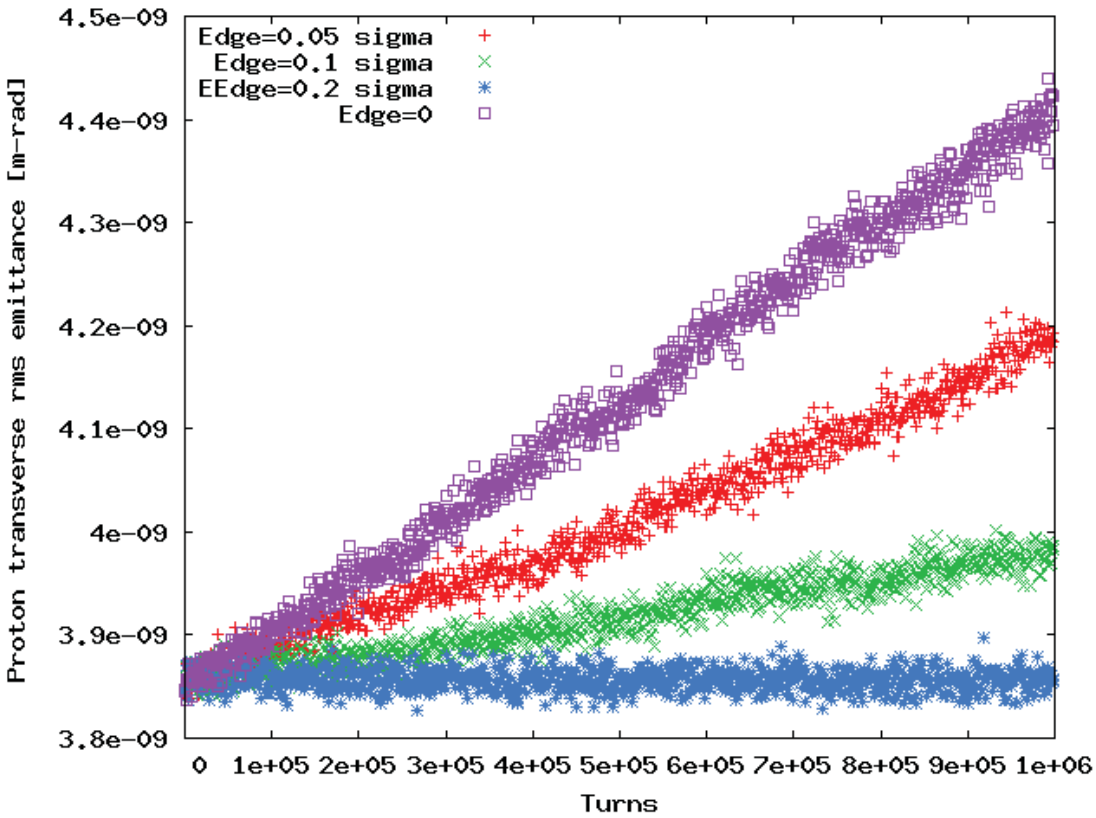

Figure 5.5: Proton emittance evolution under different size of edge in 'soft' Beer-Can distribution model.

In Figure 5.4, we can see that the beam-beam field shows only tiny difference between different edges from 0 to 0.2σ. The only difference happens at the position around boundary of Beer-Can distribution which is twice the transverse rms beam size of electron beam.

It is expected that the proton emittance growth will be reduced by introducing 'soft edge' transverse Beer-Can distribution of electron beam and Figure 5.5 confirms the expectation. If edge is set to 0.2σ, proton emittance growth is not observable in 1 million turn's computation time. This can be quantitatively evaluated by calculating the time for proton beam transverse emittance becoming two times larger as shown in Table 5.2.

Table 5.2: Lifetime of Proton beam with different edge size in Beer-Can distribution

Electron beam transverse distribution	Time for proton emittance double
Beer-Can hard edge (edge=0)	87 seconds
Beer-Can soft Edge (edge=0.05σ)	151 seconds
Beer-Can soft Edge (edge=0.1σ)	385 seconds
Beer-Can soft Edge (edge=0.2σ)	>200 hours

From the previous discussion, it is obvious that a soft electron distribution gives longer life time to the proton beam. At the edge value of 0.2σ, the beam-beam field does not differ much from hard edge Beer-Can distributions and can be considered as a reasonable estimation. However the real electron transverse distribution needs to be determined by tracking codes when lattice design is finished.

5.2. Electron Pinch Effect and Beam-Beam Field Calculation

In chapter 1, we learned that electron beam is focused by strong beam-beam force in interaction region. As an immediate result, electron beam has very small rms beam size at certain position within interaction region, usually referred as 'pinch effect'. If one pays attention to the electron beam distribution after beam-beam collision, the distribution has a dense core as well as a long tail, which deforms the

beam-beam field exerted on proton beam.

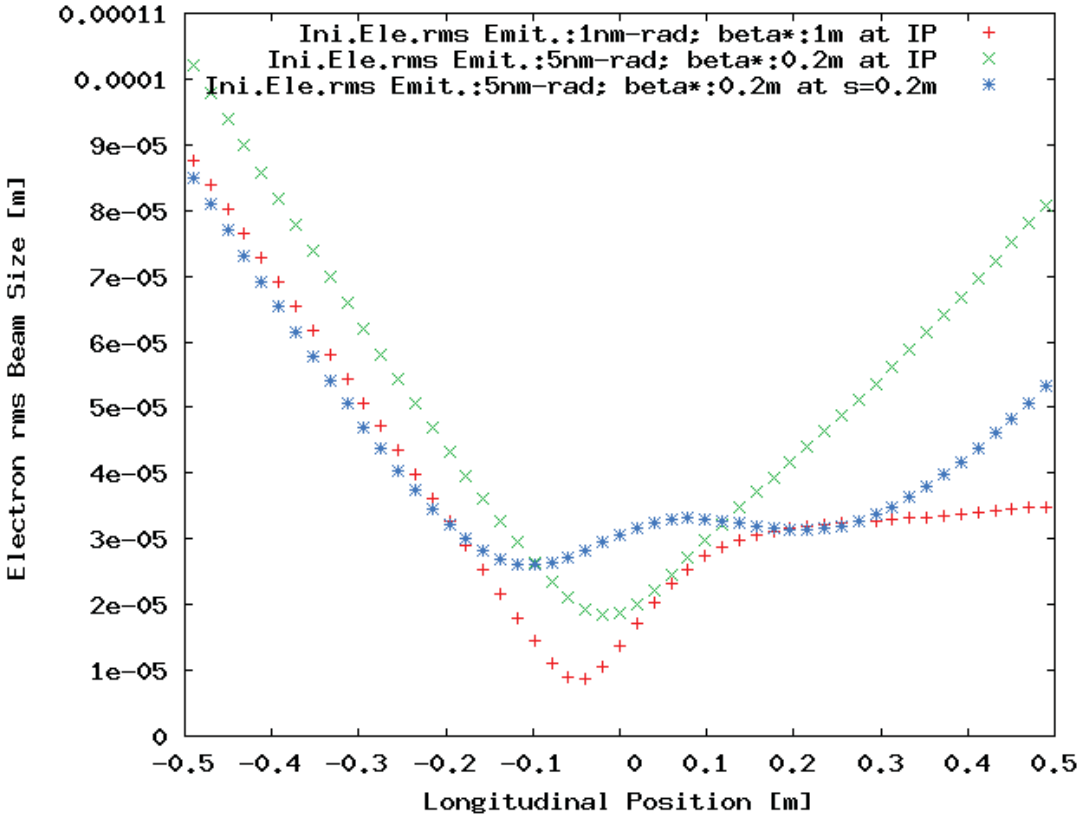

Figure 5.6: Electron pinch effect with different initial electron parameter

Figure 5.6 shows that the proton beam pinches electron beam via beam-beam force. The resulting electron beam envelope depends on the electron lattices design, according to the graph. The 'pinch effect' causes several consequences which need to be discussed in detail. The benefit from electron pinch effect is luminosity enhancement, as was covered in section 3.3. Table 3.2 gives the actual luminosity enhancement from including pinch effect.

In this section, the price for this luminosity enhancement will be assessed. The most obvious side effect is that the proton beam-beam parameter will increase as the rms electron beam size shrinks. One can rewrite the beam-beam parameter definition as:

$$\xi_p = \frac{N_e r_{0p} \beta_p^*}{4\pi\sigma_e^2 \gamma_p}$$

The parameter is inversely proportional to the square of rms size of electron beam, if the transverse electron beam distribution is Gaussian. For example if the initial electron emittance is 1nm-rad with β^*=1m at IP, the minimum rms electron beam size during collision is 8.7×10^{-6}m located as s=-0.04m, comparing with the nominal design value 3.2×10^{-5}m. Therefore proton beam-beam parameter at this specific point reaches 0.19, which is 13 times larger than the design value 0.015 in Table 1.2. If we take an average along the proton beam, the average proton beam-beam parameter during one collision is 0.067, more than four times larger than design value. It is not efficient way to gain no more than 30% luminosity with the price of 4 times larger average proton beam-beam parameter and 13 times larger peak value at a specific point.

There are two drawbacks from large beam-beam parameter induced by electron beam pinch effect.

- Large beam-beam parameter will produce large tune spread so that one cannot find proper working point to avoid nonlinear resonance. Nonlinear diffusion will destroy beam quickly

- Proton beam exerts different beam-beam parameter along the beam. Longitudinal oscillation will guide every proton in the bunch pass through the 'pinch' position which will induce synchro-betatron oscillation.

The electron rms beam size evolution can be controlled by proper initial electron optics and emittance. From Figure 5.6, the pinch effect is weakened by decreasing β^* and increasing the initial electron rms emittance. For initial emittance 5 nm-rad

and β^* value of 0.2m case, the minimum beam-beam parameter for proton beam becomes 0.043 and average beam-beam parameter throughout interaction region is 0.026.

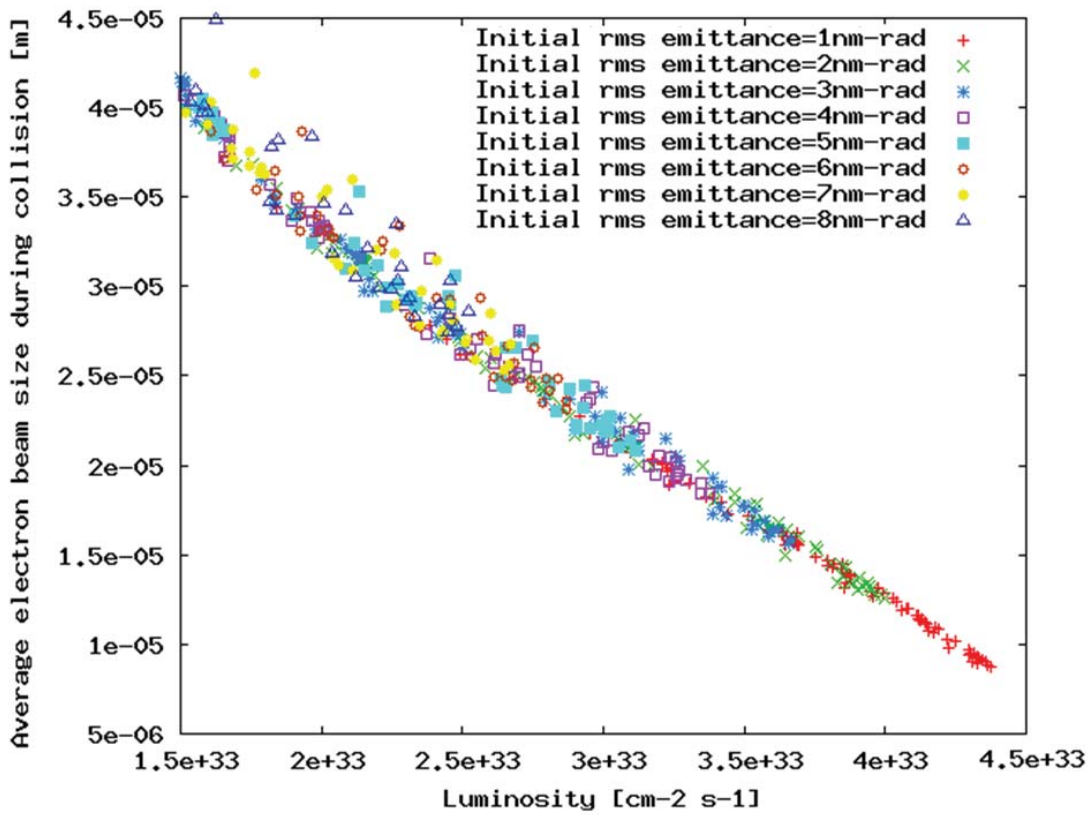

Figure 5.7: Average electron rms beam size as function of luminosity.

Followed by the procedure in section 3.5, we can vary the initial electron beam parameter to investigate the resulting average electron rms beam size. Again, we plot it as function of actual luminosity in Figure 5.7. The figure indicates a surprise fact that no matter what the initial electron beam emittance and optics are, the average electron rms beam size during collision is nearly a linear function of the luminosity. In another words, if we can get the luminosity during collision, we will approximate know the average electron beam size, hence the average beam-beam parameter of proton beam.

Besides the electron beam size shrinking, the distribution of the electron beam

also changes, and a simple model may be needed to study this. The initial electron transverse coordinate is written by (x, x') with Gaussian distribution:

$$f\left(x,x'\right) \propto \exp(-\frac{x^2+\beta^2 x'^2}{\sigma_x^2}) \tag{5.2}$$

Here f is the phase space distribution function, β is the beta function and σ_x is the rms beam size. The beam-beam kick from opposite bunch which is also Gaussian distribution is simplified as:

$$\begin{aligned} x_n &= x \\ x'_n &= x' - \frac{2\sigma_x^2}{f_x x_n}\left[1-\exp\left(-\frac{x_n^2}{2\sigma_x^2}\right)\right] \end{aligned} \tag{5.3}$$

The subscript n represents the new coordinate after kick. f_x is the focal length of beam-beam force. The map in (5.3) is symplectic map of first order which conserves energy. The old coordinate can be expressed as function of the new parameters as:

$$\begin{aligned} x &= x_n \\ x' &= x'_n + \frac{2\sigma_x^2}{f_x x_n}\left[1-\exp\left(-\frac{x_n^2}{2\sigma_x^2}\right)\right] \end{aligned}$$

According to Liouville's theorem, the distribution after collision gives:

$$f\left(x_n,x'_n\right) \propto \exp\left[-\frac{x_n^2}{\sigma_x^2}+\frac{\beta^2}{\sigma_x^2}\left(x'_n+\frac{x_n}{f_x}-\frac{x_n^3}{4\sigma_x^2 f_x}\right)^2\right] \tag{5.4}$$

Here we expand the exponential term at vicinity of zero. The distribution of angular divergence x' is no longer Gaussian. As the beam propagates forward, the phase space distribution will deviate from initial bi-Gaussian form.

We can plot the histogram of the x coordinate after beam-beam collision from the result the simulation. Figure 5.8 and Figure 5.9 show the histogram of electron coordinate and deviation from Gaussian distribution from initial electron rms emittance 1nm-rad and 5nm-rad respectively

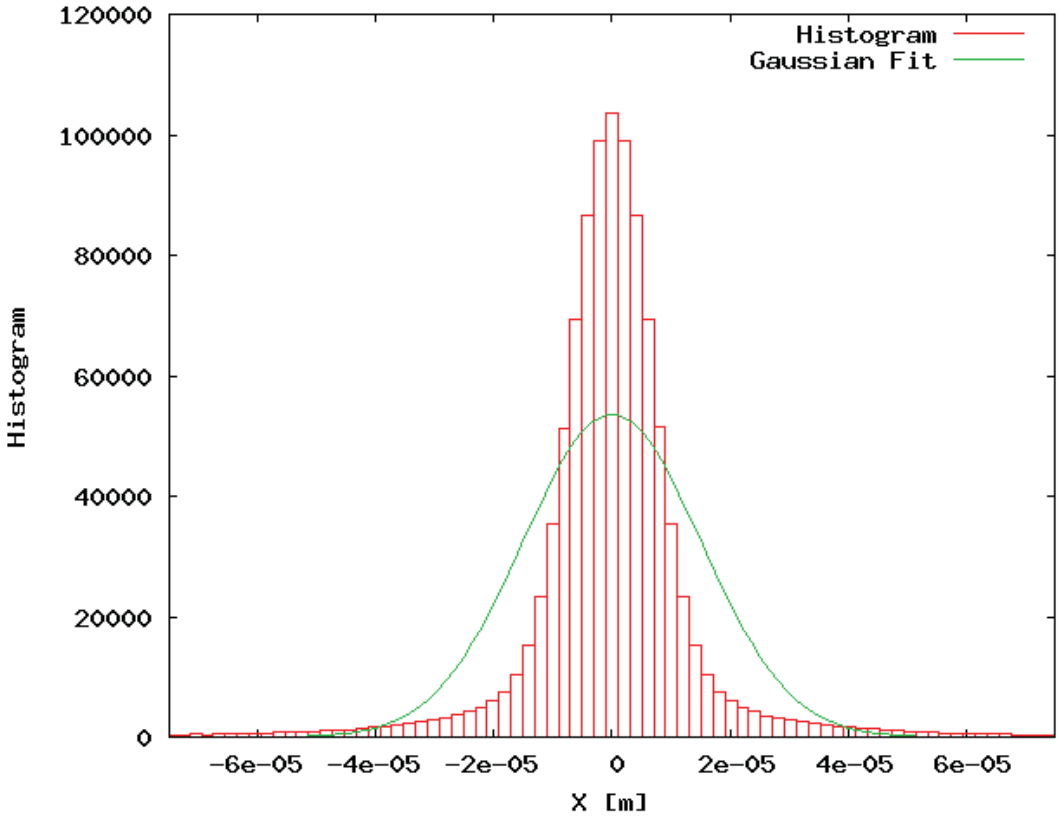

Figure 5.8: Electron position histogram after Beam-Beam collision. Initial electron rms emittance is 1nm-rad and β^* is 1m at IP. Green curve corresponds to the Gaussian function fit based on electron beam rms size and histogram data.

Figure 5.8 indicates that for small initial rms emittance and large waist beta function, the distribution has dense core and longer tail if compared with Gaussian distribution with same rms size. The deviation from Gaussian should be smaller if beta function is smaller, according to (5.4). This is confirmed by Figure 5.9. For 5nm-rad initial rms emittance and 0.2m β^*, the final electron distribution does not deform much from Gaussian distribution at all.

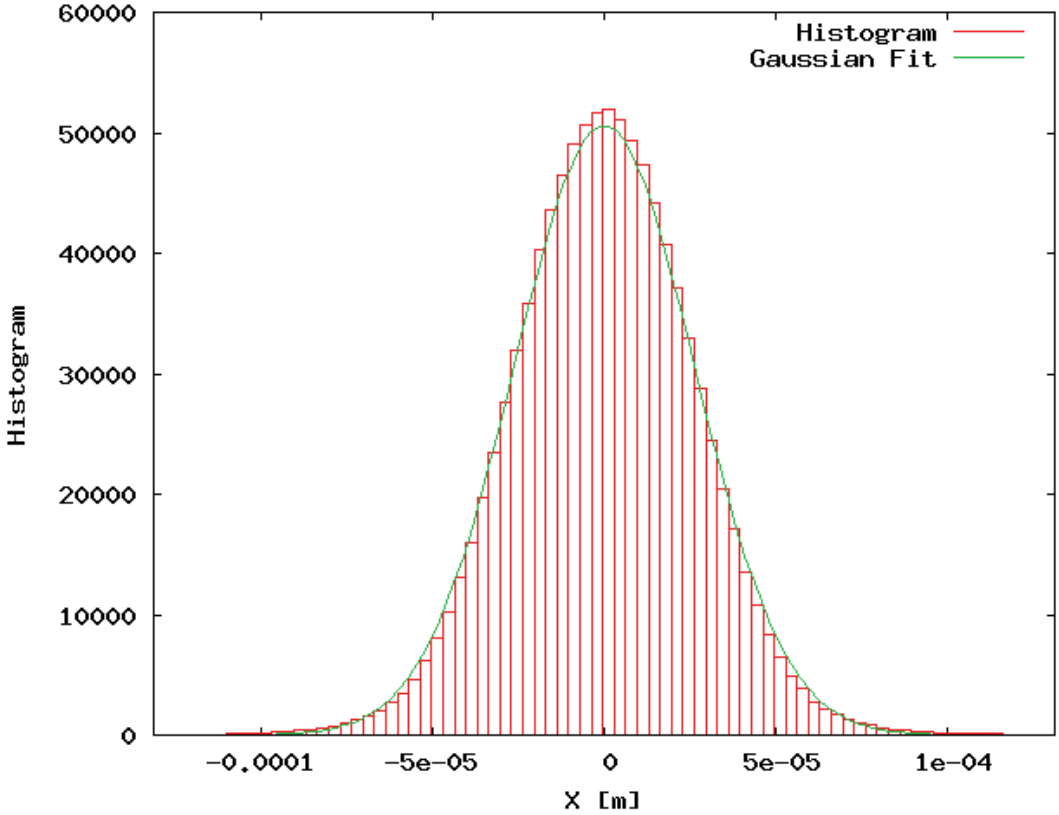

Figure 5.9: Electron position histogram after Beam-Beam collision. Initial electron rms emittance is 5nm-rad and β^* is 0.2m at IP. Green curve corresponds to the Gaussian function fit based on electron beam rms size and histogram data.

Since there is a possibility that electron transverse distribution will deviate from Gaussian distribution, it is not safe to use (2.3) to calculate the beam-beam field for each proton slices. We can take advantage of the fact that both beams are round. According to symmetry, we can alternatively calculate the electric field from Gauss's Law and the histogram of electron transverse position. And the field simply write as:

$$\begin{pmatrix} E_x \\ E_y \end{pmatrix} = -\frac{eN_e(r)}{2\pi\varepsilon_0 r^2}\begin{pmatrix} x \\ y \end{pmatrix} \tag{5.5}$$

Here $N_e(r)$ is number of electron beam that transverse displacement from axis equals or less than r.

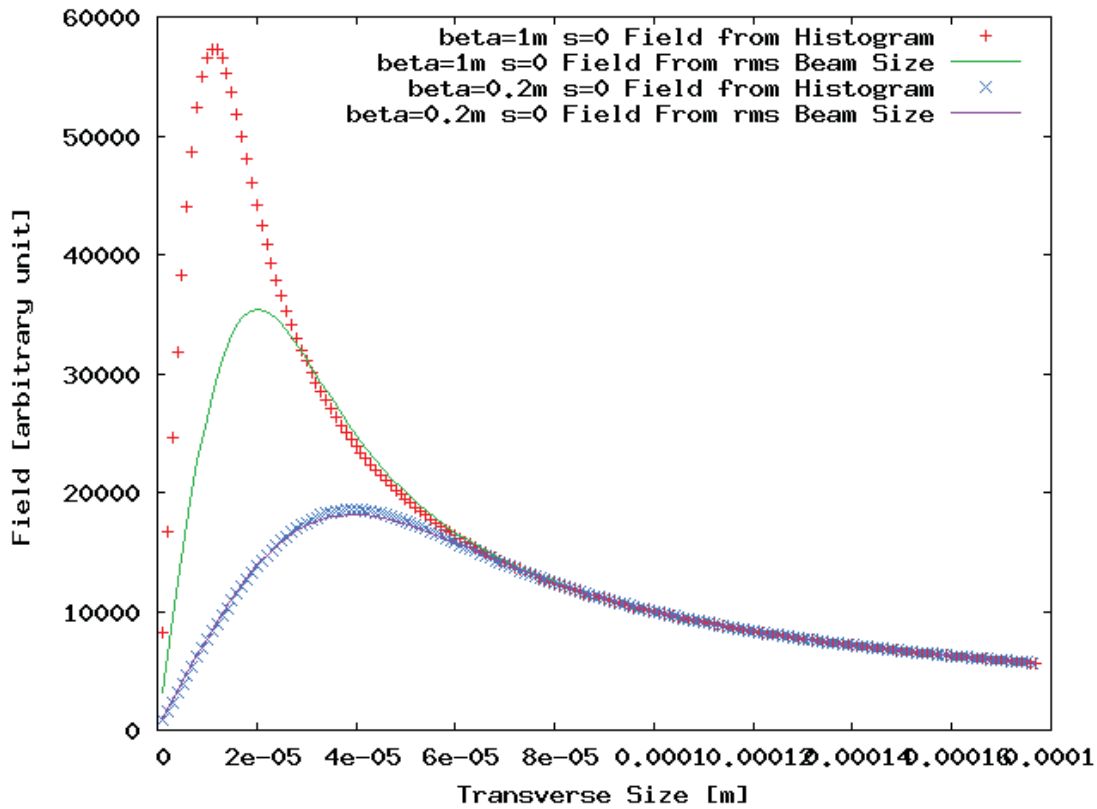

Figure 5.10: Beam-Beam field calculated by Gauss Law and from rms beam size

We compare the beam-beam field calculated from the different methods based on the electron beam after collision in Figure 5.10. The field calculated from beam histogram and Gauss's law is more accurate. And the field from (2.3) is based on the rms beam size with Gaussian distribution. For large β^* case (1m), there is huge difference between the two methods. The beam-beam field near axis is much larger than that anticipated from (2.3). If comparing the field slope near axis, the real field is about 2.5 times larger than the result from Gaussian beam formula. On the contrary, the difference is tiny for low β^* case (0.2m). The results are consistent with histogram graph Figure 5.8 and Figure 5.9.

Therefore, to calculate the beam-beam field generated by electron beam with large design beta function, the Gauss law (5.5) is required to achieve accurate effect on proton beam. For small design beta function, the Gauss's law method and equation (2.3) are expected to give similar results. In the simulation of this chapter,

we will always calculate the beam-beam field exerted by proton beam from Gauss's law method instead of equation (2.3) to increase accuracy.

5.3. Proton Emittance Growth under Pinch Effect

We have already shown that the electron beam pinch effect increases the beam-beam parameter for proton beam by two factors

- Electron rms beam size shrinks due to focusing effect of proton beam.
- Dense core formed in electron beam distributions.

A large beam-beam parameter may induce emittance growth due to nonlinear resonance. And the longitudinal position dependence of pinch effect can also deteriorate proton beam quality by synchro-betatron oscillation.

In order to focus on the pinch effect and the proton beam-beam parameter enhancement, we manually disabled the dipole moment of the proton beam. The dipole moment dynamics leads to head-tail type instability (kink instability), which is already discussed chapter 1. The working point of proton beam is set to (0.674, 0.675) to provide large tune spread space. The chromaticity is zero because the no head-tail instability will be excited due to dipole moment offset. The higher order offset will be suppressed by strong beam-beam force. The number of macro-particles for electron beam and proton beam are 50K and 300K respectively.

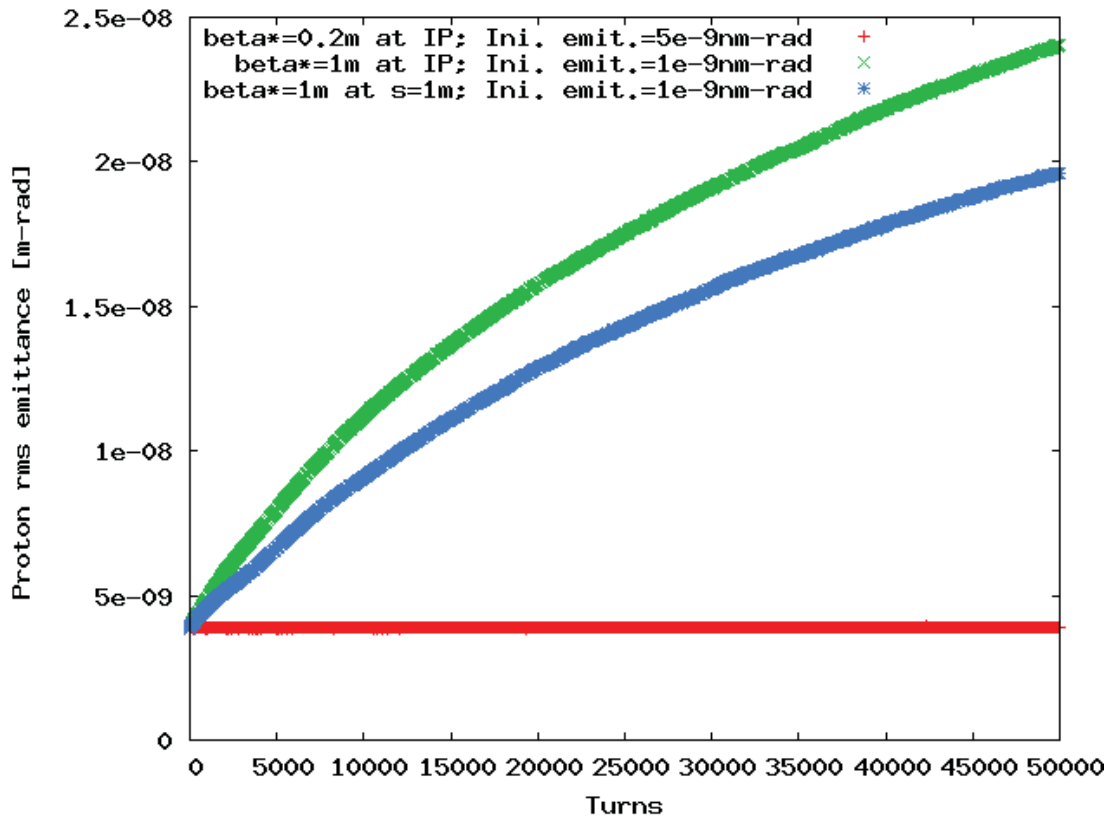

Figure 5.11: Proton rms emittance comparison between different electron beam initial emittance.

Figure 5.11 confirm the harm of large proton beam-beam parameter. As we revealed before, small initial electron rms emittance (1nm-rad and β^*=1m) yields unacceptable proton beam-beam parameter of 0.067, when electron distribution deformation is excluded. In this case, the emittance growth becomes very fast (green curve). On the contrary, the large initial electron rms emittance (5nm-rad and β^*=0.2m) case does not show obvious emittance change. However, the initial emittance 1nm-rad case also has larger luminosity than its opponent according to Table 3.2.

A more fair comparison is to compare two cases with similar luminosity. If the waist position of electron initial rms emittance 1nm-rad case shifts back from IP to s = 1m, the luminosity will drop to 2.8×10^{33}, less than the initial emittance 5nm-rad case. In this case the pinch effect is smaller because the electron beam is designed as

diverging beam before collision and focused by beam-beam force. If the luminosity is small, the average electron beam size through collision is large and the proton beam-beam parameter will be small indicated by Figure 5.7. But the emittance growth for this case (blue curve) is still very fast. This confirms the importance of distribution deformation. Although the average beam size is larger by moving the beta waist position, the β^* is still as high as 1m. Electron beam forms a dense core and deteriorates proton beam.

An important conclusion can be achieved from Figure 5.11. **In order to keep proton beam stable, we must choose large electron initial rms emittance and small beta waist position.**

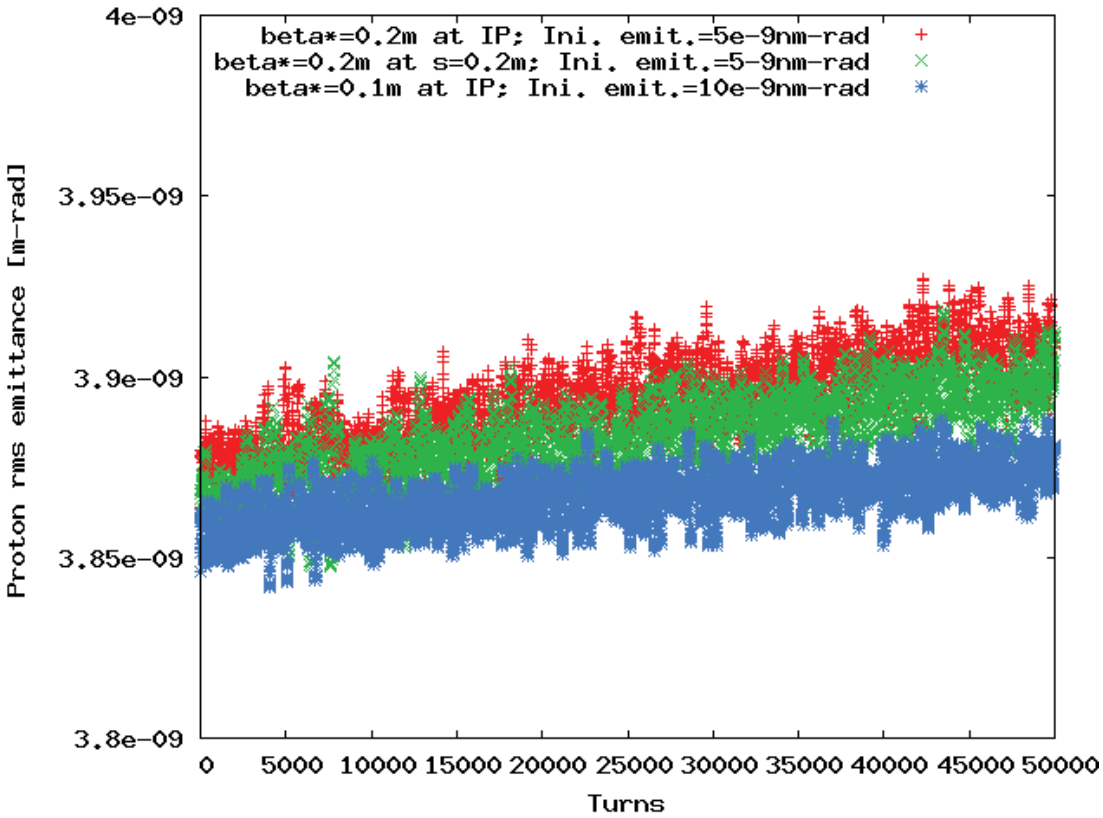

Figure 5.12: Proton rms emittance growth at small waist beta functions at different waist positions.

Table 5.3: Lifetime of Proton beam with different initial electron beam parameter

Initial electron beam parameters			Luminosity [$cm^{-2}s^{-1}$]	Time for proton emittance double
Emittance [nm-rad]	β* [m]	Waist position [m]		
1	1	0	3.7×10^{33}	0.25 seconds
1	1	1	2.8×10^{33}	0.26 seconds
5	0.2	0	3.0×10^{33}	150 seconds
5	0.2	0.2	2.6×10^{33}	200 seconds
10	0.1	0	2.3×10^{33}	400 seconds

Similar improvement can be employed for large electron initial rms emittance (5nm-rad) case to reduce pinch effect. If we shift the electron optics beta waist position backwards to s=0.2m, the luminosity will drop and the proton beam becomes more stable than the case of beta function at IP. We can see that for the large emittance case, i.e. the electron beam distribution does not deviate much from Gaussian; it is a compromise between high luminosity and stable proton beam.

The actual time for proton rms emittance increasing by factor of two will be longer than the values in Table 5.3. The reason is also from numerical noise, similar to the discussion in chapter 1. More accurate results are will need to utilize more macro-particles, both for electron beam and proton beam. With the same treatment, we fit the emittance growth as linear function and model the slope as,

$$K = a + \frac{b}{\sqrt{N_m}} \tag{5.6}$$

The slope K contains intrinsic part a and statistical error part b divided by the proton macro-particle number N_m with fixed electron macro-particles of 50000. The a and b are determined from different N_m values as:

$$
\begin{aligned}
a &= 3.2\times10^{-17} \pm 7.5\times10^{-17} \\
b &= 1.5\times10^{-13} \pm 2\times10^{-13}
\end{aligned}
\tag{5.7}
$$

It is not a surprise that the intrinsic emittance growth has a large error, due to the limitation of computation resources. More precise results require larger amount of macro-particles. Nevertheless, the emittance growth time for duplicating is already in same order as the anticipated cooling time of coherent electron cooling, which is about 15 minutes. Therefore, the emittance growth is expected to be suppressed by cooling technique.

6. NOISE

Noise is a unique issue in linac-ring collider and need to be considered carefully. In this chapter, different types of noise are analyzed separately and requirement of noise control is brought out.

6.1. Noise of Electron Beam

In linac-ring scheme, proton beam collides with fresh electron beam each turn. The imperfections of electron source, electron linac and transport path can cause variation from their design values. If the imperfection is changing from turn to turn randomly, the proton beam will exert beam-beam force with noise periodically. It should be distinguished from the periodic imperfection, which has sharp frequency spectrum. The noise may heat up proton beam and produce harmful results.

Types of noise can be classified by their frequency spectrum. If the noise contains all frequency, i.e. the power spectral density is constant, it has name of 'white noise'. Usually white noise is good approximation in real world. Here we assume all imperfections in electron beam that collides with proton beam each turn are white noise. Mathematically, the autocorrelation of the imperfection is delta function, only has none zero value if evaluated at same time.

6.2. Noise of Electron Beam Intensity and Displacement

The fluctuation of laser amplitude in the electron source and other facts may cause electron beam intensity fluctuations. As a result, the beam-beam parameter of proton beam varies from turn to turn by a small amount.

Let's consider a thin proton bunch which collides with electron bunch exactly at IP[12]. For a single proton, we have:

$$x_p'' + K^2(s)x_p = -\delta(s-nC)\frac{x_p}{f_p}\left(1+\frac{\delta_{fn}}{f_p}\right) \tag{6.1}$$

The definitions of symbols above are same as in section 4.1. δ_{fn} is the random focal length error at turn n raised from proton beam-beam parameter imperfection. We can combine the normal beam-beam kick to left hand side of (6.1), as:

$$x_p'' + \tilde{K}^2(s)x = -\delta(s-nC)\frac{x_p\delta_{fn}}{f_p^2} \tag{6.2}$$

Now the new $K(s)$ with tilde represent one turn revolution including regular beam-beam force. Only error beam-beam kick left in right hand side of (6.2). Assuming the beam-beam force is small, if not at IP, the motion x_p is approximately given as:

$$x_p(\mathrm{s}) = Aw(s)\cos(\psi(s)) \tag{6.3}$$

A is the betatron motion amplitude and unchanged between two beam-beam kick, $w(s)$ and $\psi(s)$ satisfy the envelope equation:

$$w'' + K'^2(s)w - \frac{1}{w^3} = 0 \qquad \psi' = \frac{1}{w^2}$$
$$\beta(s) = w^2(s) \tag{6.4}$$

Then between beam-beam collisions, the normalized particle motion $X_p(s)=x_p(s)/w(s)$ is just a sinusoidal motion with modulated phase $\psi(s)$. Then we have:

$$X(s)^2 + \left[X'(s)w^2(s)\right]^2 = A^2 \tag{6.5}$$

Just after error beam-beam kick at IP, the equation still holds with different amplitude:

$$X\left(s=0^+\right)^2 + \left[\left(X'\left(s=0^+\right) + \frac{\delta x'(0)}{w\left(s=0^+\right)}\right)w^2\left(s=0^+\right)\right]^2 = A^2 + \delta A^2 \tag{6.6}$$

Subtracting (6.6) from (6.5) and tracking on ensemble average, gives:

$$\left\langle \delta A^2 \right\rangle = \left\langle \left(w\left(s=0^+\right)\delta x'\right)^2 \right\rangle \tag{6.7}$$

If T represents the revolution period of the proton ring, from (6.3), the increase rate of average beam size at IP gives:

$$\frac{d\left\langle x_p^2\right\rangle}{dt} = \frac{\beta_p^*\left\langle \delta A^2\right\rangle}{2T} = \frac{\beta_p^{*2}\left\langle \delta x'^2\right\rangle}{2T}$$
$$= \frac{\beta_p^{*2}\left\langle x_p^2\right\rangle}{2Tf_p^2}\frac{\left\langle \delta f_{pn}^2\right\rangle}{f_p^2} \tag{6.8}$$

The momentum change due to error beam-beam kick is easily get from (6.2). It shows that the random error of linear field will cause beam size to grow exponentially. Then increase rate is inverse proportional to the error square, which reads,

$$\sqrt{\langle x_p^2 \rangle(t)} = \sqrt{\langle x_p^2 \rangle(0)} \exp(t/\tau)$$
$$\tau = \frac{4Tf_p^2}{\beta_p^{*2}} \frac{f_p^2}{\langle \delta f_{pn}^2 \rangle} = \frac{T}{4\pi^2 \xi_p^2} \frac{f_p^2}{\langle \delta f_{pn}^2 \rangle} \tag{6.9}$$

The factor two difference between (6.9) and (6.8) is because we are evaluating rms beam size in latter equation instead of beam size square in earlier one.

It is worthwhile to note that we are discussing a thin proton bunch passing through a linear thin lens with random error in focal length. The emittance of the proton beam should be remaining constant. This is not contradictory to the result of (6.9), which shows the rms beam size grows exponentially. The key to solve the paradox is that the result of (6.9) is statistical average of large ensemble. For one specific proton bunch, the rms beam size at IP will oscillate with increasing envelope. At the mean while, the rms beam transverse momentum also oscillates with an increasing envelope. But there is π phase shift between two oscillations, which lead to a constant emittance at all times.

If we plug in the design value of eRHIC, the rise time can be plotted as the relative error of electron beam intensity fluctuation ($=\langle \delta_f / f \rangle$). To get reasonable rise time ($\gg$10 hours), the electron beam intensity should be very stable, at order of 1×10^{-4}.

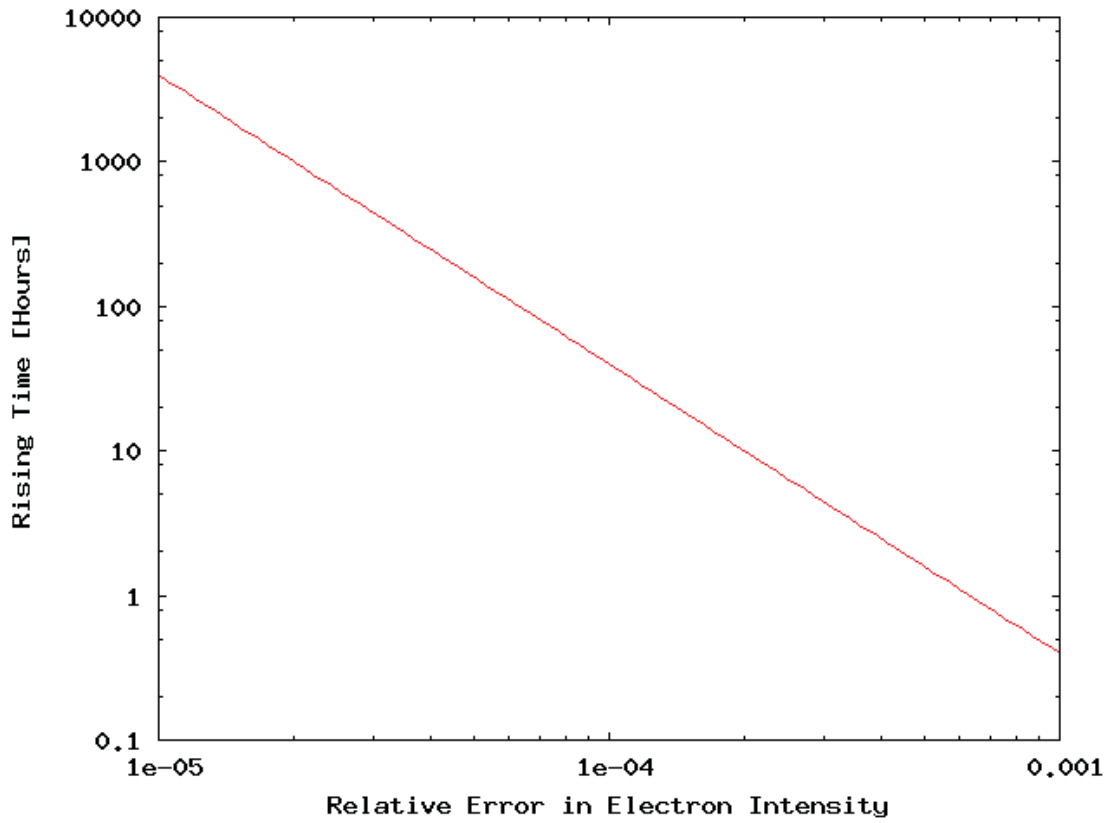

Figure 6.1: Transverse rms size rising time as function of electron intensity relative rms error

A simple simulation can verify what we get so far. To get quick effect, we set the error of electron intensity as 1×10^{-2} rms error. According to (6.9), the resulting increase rate is 1.125 million turns, which is 14.4 seconds.

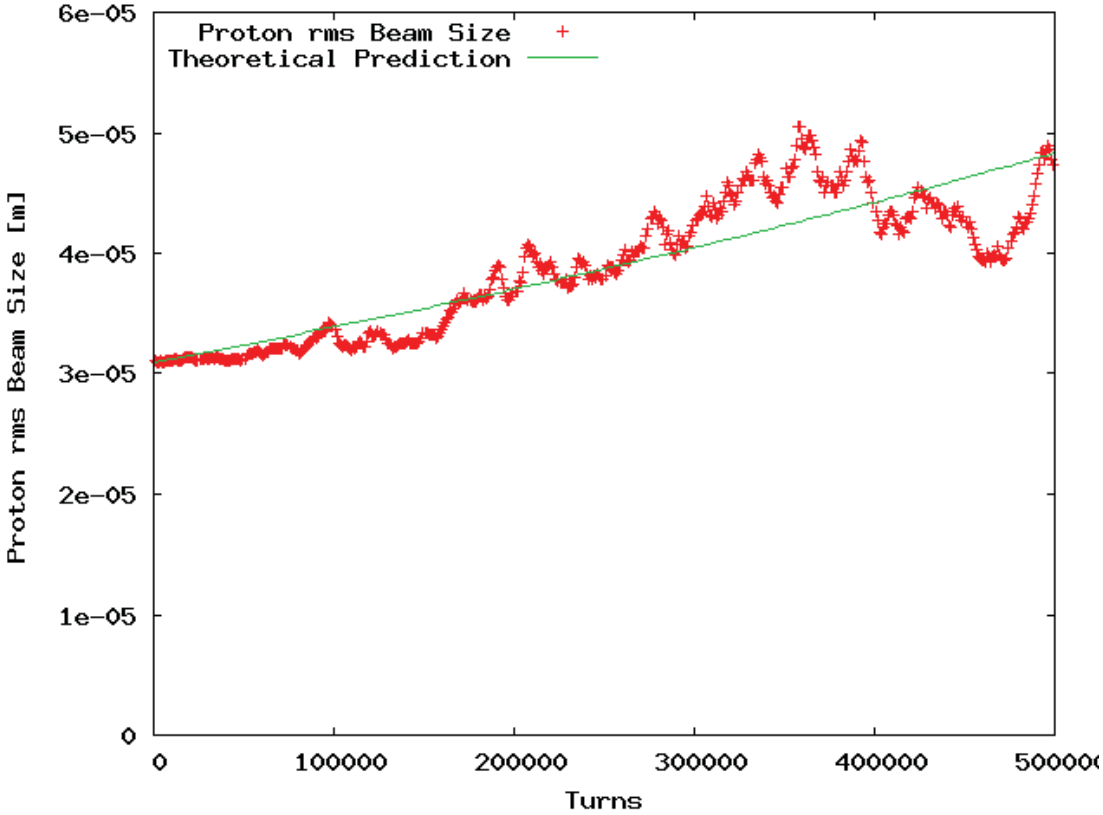

Figure 6.2: Proton rms beam size evolution under the presence of electron intensity noise and comparison with prediction of equation (6.9), each beam size data is the average of 1000 turns nearby.

Figure 6.2 shows good agreement between simulation and theory. The deviation between the simulation and the theoretical prediction is because the randomness of error each turn. The ensemble average will give perfect agreement with theory.

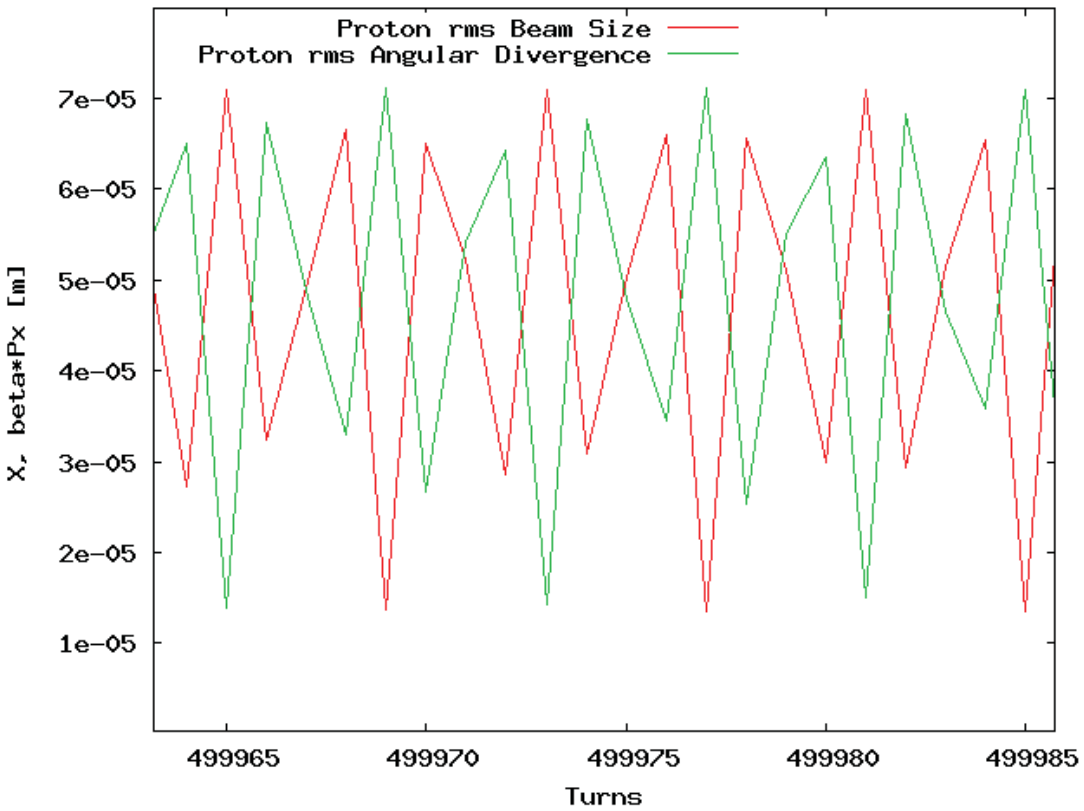

Figure 6.3: Details of proton beam rms beam size and angular divergence without averaging under the presence of electron intensity noise .

Figure 6.3 gives explanation on why the proton rms beam size grows exponentially under the noisy electron beam intensity while the rms beam emittance remain constant since the force is always linear. Both proton rms beam size and rms angular divergence actually oscillate under the presence of noise. Both oscillation amplitudes grow exponentially. When beam size reaches maximum, the rms angular divergence reaches minimum and maintain the emittance constant and vice versa.

Another imperfection can be the electron transverse position displacement at interaction region caused by orbit jitter. If there is tiny transverse displacement when two beams collide, the proton beam will exert an extra kick, which is proportional to the value of displacement. Consider the displacement is random from turn to turn; we can compare it with Brownian motion. The proton beam size is expected to grow linearly as function of square root of time. To prove our

expectation, we can perform similar steps as the beam intensity fluctuation. Equation (6.2) should be rewritten as:

$$x_p'' + \tilde{K}^2(s)x = -\delta(s - nC)\frac{d_n}{f_p} \tag{6.10}$$

d_n is the electron beam displacement at IP of turn n. After same steps, the equation (6.8) has the form:

$$\begin{aligned}\frac{d\langle x_p^2\rangle}{dt} &= \frac{\beta_p^*\langle\delta A^2\rangle}{2T} = \frac{\beta_p^{*2}\langle\delta x'^2\rangle}{2T} \\ &= \frac{\beta_p^{*2}}{2T}\frac{\langle d_n^2\rangle}{f_p^2}\end{aligned} \tag{6.11}$$

Explicitly, the proton rms beam size under random electron beam transverse displacement gives:

$$\sqrt{\langle x_p^2\rangle}(t) = \sqrt{\frac{\langle d_n^2\rangle\beta_p^{*2}t}{2Tf_p^2} + \langle x_p^2\rangle(t=0)} \tag{6.12}$$

Here, the expectation of rms beam size increasing is confirmed. To make proton beam stable, we need the first term in right hand side of (6.12) is smaller than second term in cooling time (~1/4 hours). We have:

$$\begin{aligned}&\frac{\langle d_n^2\rangle\beta_p^{*2}(0.25hour)}{2Tf_p^2} < \langle x_p^2\rangle(t=0) \\ &\sqrt{\langle d_n^2\rangle} < 8.8\times10^{-4}\sqrt{\langle x_p^2\rangle(t=0)}\end{aligned} \tag{6.13}$$

This requires that the transverse rms jitter at IP should be less than 2.8e-8m.

7. CONCLUSION

ERL based eRHIC project is a promising design with revolutionary ideas which currently in its R&D stage. As world first linac-ring collider, it takes full advantage of linac accelerator, which provide fresh electron bunch for each collision, to provide high luminosity electron-proton (10^{33} $cm^{-2}s^{-1}$) and electron-heavy ion (10^{32} $cm^{-2}s^{-1}$) collisions.

There are some special features that arose from the linac-ring collision concept, that are trivial in traditional ring-ring collision. The large beam-beam parameter and disruption factor induce electron beam distortion during beam-beam collision. This distortion enlarges electron beam emittance and possibility of electron beam loss. For the proton beam, the beam-beam parameter increases when the proton beam interacts with the distorted/pinched electron beam. The proton rms emittance may grow under large beam-beam parameter. Besides distortion, the offset of foreside proton beam could be transferred to rear part of proton beam. The beam-beam force can be regarded as wake field. The present design parameters of eRHIC are beyond the stability threshold under this effective wake field. The fresh electron beam for each collision will introduce noise to proton beam, which will heat up the proton can cause beam loss.

Through analytical calculation and simulation, all special features above are studied carefully. The electron disruption effect and distribution distortion can be

controlled by proper electron lattice and initial rms emittance. A large initial rms emittance (5nm-rad) and small waist beta function (0.2m) can reduce the mismatch between electron distribution after collision and design lattice and the electron distortion due to nonlinear force.

After the study above, we can suggest a new set of parameters and update the parameter table as shown in Table 7.1. This set of electron beam parameters can bring benefits to both electron and proton beam.

Table 7.1: Updated ERL based eRHIC parameter table

	High energy setup		Low energy setup	
	p	e	p	e
Energy (GeV)	250	10	50	3
Number of bunches	166		166	
Bunch spacing (ns)	71	71	71	71
Bunch intensity ($\times 10^{11}$)	2	1.2	2.0	1.2
Beam current (mA)	420	260	420	260
95% normalized emittance (π·mm·mrad)	6	**575**	6	**575**
Rms emittance (nm),	3.8	**5.0**	19	**16.5**
β^* (cm), x/y	26	**20**	26	**30**
Beam-beam parameters, x/y	0.015	**0.46**	0.015	**0.46**
Rms bunch length (cm)	20	0.7	20	1.5
Polarization, %	70	80	70	80
Peak Luminosity, $cm^{-2}s^{-1}$	**2.6×10^{33}**		0.53×10^{33}	

Analytical approach and simulation also show that the kink instability induced

by beam-beam force has threshold which is more than ten times smaller than the present design parameter. Proper tune spread is necessary to suppress fast proton emittance growth. Simulation shows a chromaticity value 7 to 8 is optimum for rms energy spread 5×10^{-4}. The tune spread can also be achieved by nonlinear lattice elements such as octopoles.

We also estimate the effect on proton beam due to turn by turn noise from fresh electron bunch. Both dipole and quadrupole errors and their consequence are analyzed. These criterions are brought out for certain proton lifetime.

The contents are not only useful in linac-ring collider, but also can be utilized in other very important projects such as in general wake field study, ILC pinch effect calculation and general electron cloud studies.

Appendix A. Symplectic Integrator

Suppose we have a dynamical system which is described by Hamiltonian, the symplectic integrator is developed to solve the equation of motion. The drawback of differential equation solver such as Leap-Frog, 4th order Runge-Kutta method is that they do not conserve system energy, i.e. the Hamiltonian is not constant as function of the independent variable.

For a dynamical system, its time independent Hamiltonian can be written as:

$$H\left(\vec{x},\vec{p}\right)=A\left(\vec{p}\right)+V\left(\vec{x}\right) \tag{A.1}$$

The equation of motion gives:

$$\frac{d\vec{x}}{dt}=\frac{\partial H}{\partial \vec{p}} \qquad \frac{d\vec{p}}{dt}=-\frac{\partial H}{\partial \vec{x}} \tag{A.2}$$

Here we use time t as the independent variable for universality. In application to accelerators, the longitudinal position s is usually chosen as independent variable for convenience.

The solution of equation motion has the form:

$$\begin{aligned} \vec{x} &= \vec{x}\left(\vec{x}_0, \vec{p}_0, t\right) \\ \vec{p} &= \vec{p}\left(\vec{x}_0, \vec{p}_0, t\right) \end{aligned} \tag{A.3}$$

The parameters with subscript *0* represent initial conditions. Alternatively, the solution can be express as a time dependent map of initial conditions:

$$\begin{pmatrix} \vec{x} \\ \vec{p} \end{pmatrix} = \vec{M}\left(t\right) \begin{pmatrix} \vec{x}_0 \\ \vec{p}_0 \end{pmatrix} \tag{A.4}$$

(A.3) or (A.4) are exact solutions of equation of motion (A.2). If we perform any numerical solving methods, the result will be only on approximate solution up to certain accuracy. If we can find the symplectic integrator map M_k, which satisfies:

$$\left\| \vec{M}_k\left(t\right) - \vec{M}\left(t\right) \right\| = O\left(t^{k+1}\right) \tag{A.5}$$

We will call M_k as symplectic integrator of order k.

In order to find the symplectic integrator of order k, we perform canonical transformation by a proper generation function so that the new Hamiltonian vanishes up to the kth order of independent variable t. And the map M_k can be derived from generation function of the third kind.

For symplectic integrator of order k, we can divide the time interval Δt_i, the time step from coordinate (x_i, p_i) to (x_{i+1}, p_{i+1}), to k sub-steps. For each sub-step we write the map as:

$$\begin{aligned} \vec{p}_{i,j+1} &= \vec{p}_{i,j} - c_j \frac{\partial V\left(\vec{x}_{i,j}\right)}{\partial \vec{x}_{i,j}} \Delta t_i \\ \vec{x}_{i,j+1} &= \vec{x}_{i,j} + d_j \frac{\partial A\left(\vec{p}_{i,j+1}\right)}{\partial \vec{p}_{i,j}} \Delta t_i \end{aligned} \tag{A.6}$$

For each time step *i*, the sub-step number *j* runs from 1 to order number k. c_j and d_j are constant parameters that only depend on order k. The usual order number can be 1, 2 or 4.

For k=1, the parameters give:

$$\begin{aligned} c_1 &= 1 \\ d_1 &= 1 \end{aligned} \tag{A.7}$$

For second order symplectic integrator, the parameters have the values:

$$\begin{aligned} c_1 &= 0 \qquad c_2 = 1 \\ d_1 &= 1/2 \quad d_2 = 1/2 \end{aligned} \tag{A.8}$$

Fourth order symplectic integrator has most popular usage, which has the parameter values:

$$\begin{aligned} c_1 &= 0 \qquad c_2 = 2x+1 \quad c_3 = -4x-1 \quad c_4 = 2x+1 \\ d_1 &= x+0.5 \quad d_2 = -x \qquad d_3 = -x \qquad d_4 = x+0.5 \end{aligned} \tag{A.9}$$

The parameter x has value of 0.1756. It is worthwhile to note that the parameters are not unique and may have other set of values.

Reference

[1] http://www.agsrhichome.bnl.gov/NT-share/rhicdm/index.html

[2] *eRHIC Zeroth-Order Design Report*, M. Farkhondeh and V. Ptitsyn, CA-D Note 142, 2004

[3] *eRHIC Accelerator Position Paper*, For NSAC Long Range Plan 2007, 2007

[4] D. Mohl, et al., Physics Reports-Review Section of Physics Letters 58 (1980) 73.

[5] A. H. Sorensen and E. Bonderup, Nuclear Instruments & Methods in Physics Research 215 (1983) 27.

[6] M. S. Zolotorev and A. A. Zholents, Physical Review E 50 (1994) 3087.

[7] V. N. Litvinenko and Y. S. Derbenev, in *Proceedings of the Free Electron Laser Conference*, Novosibirsk, Russia,(2007)

[8] S. M. Gruner, et al., Review of Scientific Instruments 73 (2002) 1402.

[9] R. Li and J. J. Bisognano, Physical Review E 48 (1993) 3965.

[10] Y. Zhang, K. Ohmi, and L. M. Chen, Physical Review Special Topics-Accelerators and Beams 8 (2005)

[11] S. A. Heifets, G. A. Krafft, and M. Fripp, Nuclear Instruments & Methods in Physics Research Section a-Accelerators Spectrometers Detectors and Associated Equipment 295 (1990) 286.

[12] Y. Hao, et al., in *Proceedings of the Particle Accelerators Conference 07*,

Albuquerque, NM,(2007)

[13] E. A. Perevedentsev and A. A. Valishev, Physical Review Special Topics-Accelerators and Beams 4 (2001)

[14] R. Li, et al., in *Proceedings of the Particle Accelerator Conference*, Chicago,(2001)

[15] E. Benedetto, et al., Physical Review Special Topics-Accelerators and Beams 8 (2005)